

**Seismic Investigations of a
Bottom Simulating Reflector:
Implications on Gas Hydrate and Free Gas
at Southern Hydrate Ridge**

DISSERTATION
ZUR ERLANGUNG DES DOKTORGRADES
DER MATHEMATISCH-NATURWISSENSCHAFTLICHEN FAKULTÄT
DER CHRISTIAN-ALBRECHTS-UNIVERSITÄT
ZU KIEL

vorgelegt von

Cord Papenberg

Kiel, 2004

Referent/in:

Korreferent/in:

Tag der mündlichen Prüfung:

Zum Druck genehmigt:

Prof. Dr. E. R. Flüh

Prof. Dr. W. Rabbel

29. November 2004

Kiel, 29. November 2004

Der Dekan

Abstract

One of the key questions related to the prediction of the hydrate distribution and quantity is the nature of the interface at the base of the gas hydrate stability zone (GHSZ), where it is generally considered that free gas is present below. The presence of gas below the gas hydrate stability zone is a major contributor to the formation of a bottom simulating reflector (BSR) present in seismic profile records.

Improved geophysical methods were used in September 2000 during cruise *Sonne SO-150* to seismically investigate the nature of the BSR across Hydrate Ridge, which is part of the Cascadia accretionary complex, offshore the Oregon continental margin. The experiments were carried out by using a variety of source and receiver acquisition systems. Within the scope of Ocean Drilling Program (ODP) Leg 204, Southern Hydrate Ridge was drilled in the year 2002 providing additional information to verify the results derived from the seismic data and supporting ongoing analyses with relevant acoustic log data.

The analyses, presented in this study, focus on deriving P-wave velocities from the seismic data to quantify the gas hydrate content within the GHSZ. By combining ocean bottom hydrophone (OBH) data with surface (SCS) and deep tow streamer data, an accurate velocity-depth distribution is determined, which is constrained by the acoustic logs of Ocean Drilling Program (ODP) Leg 204 and the depth of the BSR is predicted within a 5 m uncertainty. In general, the P-wave velocities are below 1600 m/s, averaged over the entire GHSZ, which leads to an estimate of about 1% of hydrate of pore space. This is in general below the average value of 2% resulting from ODP analyses, but is within an uncertainty of 1%, when considering thin hydrated layers affecting the mean velocity distribution.

The analyses of the frequency dependent amplitude variations of the BSR signal, result in the presence of a thin gas bearing layer below the BSR with an average thickness of 8 ± 4 m. The existence of a thick gas zone of several 100 m beneath the GHSZ, as observed in other hydrate provinces, is ruled out by P-wave velocity considerations. The presence of a thin gas layer leads to the assumption that amplitude variation along the BSR, in addition to a change in the gas concentration, is caused by tuning effects. Amplitude and velocity anomalies are not necessarily the result of a change in gas hydrate saturation. Further, it is assumed that this thin gas layer is an indication for gas hydrate in the GHSZ being recycled due to tectonic uplift and a major contributor for the free gas below.

Zusammenfassung

Eine der am häufigsten gestellten Fragen im Bezug auf die Vorhersage der Gas Hydrat Verteilung und Quantifizierung ist die nach der Beschaffenheit der Unterkante der Gas Hydrat Stabilitätszone (GHSZ). An deren Unterseite wird im allgemeinen freies Gas vermutet. Die Anwesenheit von freiem Gas unterhalb der Stabilitätszone ist ein wesentlicher Beitrag für die Abbildung eines Boden Simulierenden Reflektors (BSR) in seismischen Aufzeichnungen. Unterschiedliche geophysikalische Methoden wurden im September 2000 während der Meßfahrt *Sonne SO-150* angewandt, um die Beschaffenheit des BSR am Hydrat Rücken im Cascadia Subduktionskomplex des Oregon Kontinentalrandes zu untersuchen. Die Experimente wurden mit unterschiedlichen Quell- und Empfängerkonfigurationen durchgeführt. Im Rahmen des Ocean Drilling Program (ODP) Leg 204 wurden im Jahr 2002 Bohrungen am südlichen Hydrat Rücken durchgeführt. Diese liefern zusätzliche Informationen, um die Ergebnisse der seismischen Untersuchungen zu verifizieren und um weitergehende Analysen mit Hilfe von relevanten Logdaten zu unterstützen. Die Analysen in dieser Arbeit beschäftigen sich mit der Ableitung eines P-Wellen Geschwindigkeitsfeldes aus den seismischen Daten, um die Gas Hydrat-Menge innerhalb der GHSZ zu quantifizieren. Die Kombination von Ozean Boden Hydrophon (OBH) Daten mit Oberflächen Streamer (SCS) und tiefgeschleppten Streamer Daten ermöglicht es, eine genaue Geschwindigkeits-Tiefen-Verteilung zu errechnen, welche durch die gemessenen Akustiklogs des ODP Leg 204 verifiziert werden. Hierbei liegt die Vorhersage der BSR-Tiefe mit einer Ungenauigkeit von 5 m bei den gemessenen Tiefen des ODP Projektes. Im allgemeinen liegen die aus den seismischen Daten abgeleiteten Geschwindigkeiten in der GHSZ unterhalb von 1600 m/s. Diese niedrigen Geschwindigkeiten weisen auf einen geringen Hydratanteil von ungefähr 1% im Porenraum hin, welcher unterhalb des Ergebnisses der ODP Daten von 2% liegt. Berücksichtigt man den Effekt von dünnen hydratisierten Schichten auf die mittlere Geschwindigkeit innerhalb der gesamten GHSZ, liegt dieser Wert jedoch in der Ungenauigkeit von 1%. Die Analysen der frequenzabhängigen Amplitudenvariationen am BSR resultieren in einer dünnen gashaltigen Schicht unterhalb des BSR, deren Dicke $8 \text{ m} \pm 4 \text{ m}$ entspricht. Eine gashaltige Schicht mit größerer Mächtigkeit unterhalb der GHSZ läßt sich anhand von Geschwindigkeitsanalysen ausschließen. Das Vorhandensein einer dünnen Gasschicht läßt die Vermutung zu, daß die Amplitudenvariationen am BSR, im Zusammenhang mit möglichen Änderungen der Gaskonzentration, auch durch Tuningeffekte verursacht werden. Amplituden- und Geschwindigkeitsanomalien sind nicht unweigerlich das Ergebnis von sich ändernden Hydratkonzentrationen innerhalb der GHSZ. Weiterhin deutet das Vorhandensein einer dünnen freien Gasschicht darauf hin, daß sich das Hydrat, hervorgerufen durch tektonische Hebungen, an der Unterkante der GHSZ auflöst und somit ein primärer Lieferant für das frei Gas darstellt.

Contents

1	Preface	1
1.1	Introduction	1
1.2	The Bottom Simulating Reflector	2
1.3	Study area: Hydrate Ridge	5
1.4	Overview	7
2	Data	9
2.1	Introduction and Research Area	9
2.2	Data Processing	10
2.2.1	Pre-processing	10
2.2.2	Geometry considerations	11
2.2.3	Frequencies	14
2.2.4	Swell-filtering	17
2.2.5	Data	19
3	Velocity Model	29
3.1	Introduction	29
3.2	Pre-modeling considerations	30
3.2.1	Arrival picking and classifying	30
3.2.2	Data uncertainties	30
3.2.3	Data Fitting	31
3.3	Modeling	32
3.3.1	Starting Model	32
3.3.2	Inversion	33
3.3.3	Model Assessment	34
3.3.4	Final Model	39
3.4	Model discussion	42
3.5	Summary	48

4	Amplitude Analysis	49
4.1	Introduction	49
4.2	AVO considerations	50
4.3	Amplitude versus offset	51
4.3.1	Theory	51
4.3.2	Amplitude corrections	57
4.4	AVO anomalies	61
4.4.1	Summary	68
4.5	Quantitative AVO	68
4.5.1	AVO on OBS 61-63	68
4.5.2	AVO modeling at ODP Site 1244	70
4.5.3	Summary	73
4.6	Conclusion	74
5	Frequency Analysis	75
5.1	Introduction	75
5.2	Thickness estimation	76
5.2.1	Change in velocity	78
5.2.2	Change in gradient	81
5.2.3	Thickness estimation	83
5.2.4	Summary	86
5.3	Thin beds and AVO	87
5.3.1	Introduction	87
5.3.2	Thin bed analysis	87
5.4	Conclusion	90
6	ODP Leg 204 & Interpretation	91
6.1	Introduction	91
6.2	Previous studies	93
6.3	The gas hydrate stability zone	97
6.4	Free gas below the BSR	105
7	Conclusion and Outlook	109
	Bibliography	111

1 Preface

1.1 Introduction

Gas hydrate, also called gas clathrate, is a naturally occurring solid. It is composed of water molecules, which form a rigid lattice of cages, where most cages contain a molecule of natural gas, mainly methane. Gas hydrate occurs worldwide, but because of the pressure-temperature and gas volume requirements, its occurrence is restricted to two regions: polar region and continental margins. The fact that natural gas hydrate is metastable and affected by changes in pressure and temperature makes any released methane an attractive agent that could globally affect oceanic and atmospheric chemistry and ultimately global climate. And finally this characteristic of metastability could explain major seafloor instabilities resulting in submarine slides and slope failures. Destabilized gas hydrates may also effect climate through the release of methane, a "greenhouse" gas, which enhances global warming. To quantify the likely volume of hydrates and their potential as a resource and their role in global climate, it is important to understand both the distribution of hydrates in sediments and the mechanical properties of hydrate-bearing formations. Retrieved samples show individual particles of hydrate disseminated in the sedimentary section, but hydrates also occur as intergranular cement, nodules, laminae, veins and massive layers. In both marine and terrestrial permafrost deposits, hydrate-bearing sections typically vary in thickness from a few centimeters to 30 m. Hydrate that acts as cement stiffens the sediment matrix. It may also occur in the pore space without significantly affecting sediment rigidity. When gas hydrates form in the interstitial pore spaces of consolidating sediments, solid hydrate rather than liquid water occupies the pore spaces, and the diagenetic processes of consolidation and mineral cementation are greatly inhibited.

Most marine hydrates seem to be confined to edges of continents where water is about 5000 m deep and where nutrient-rich waters unload organic detrius for bacteria to convert to methane. Gas hydrates have been found at the seafloor, but their usual range is 100 to 500 m beneath it. In permafrost regions, they occur at shallower depths because surface temperatures are lower. Large accumulations have been identified offshore Japan, at the Blake Ridge off the US eastern coast, on the Cascadia continental margin off Vancouver, and offshore Oregon, and New Zealand. Only a small portion of the evidence for hydrate accumulations around the world comes from direct sampling, however; most is inferred from other sources, such as well logs, drilling data,

pore-water-salinity measurements and seismic reflection data.

The velocity of sound in pure hydrate is believed to be similar to that of ice, but the exact value has not been agreed upon, and probably depends on hydrate chemistry (e.g. 3300 m/s (*Sloan, 1998*), 3650 ± 50 m/s (*Stern et al., 2000*)). The acoustic velocity of a hydrate-cemented layer is therefore high - higher than in fluid filled sediment. As a result, the contact between a hydrate-rich layer and a gas-filled layer can act as a prominent seismic reflector. These reflectors, which occur at the base of the hydrate zone, are known as bottom simulating reflectors (BSR). Their shape mimics the shape of the seabottom, and the polarity of the seismic reflection signal is reversed. The depth of the BSR below the seabottom depends on the temperatures and pressures required for hydrate stability. The occurrence of a BSR in seismic reflection data is the most important indicator of hydrates in marine sediments.

1.2 The Bottom Simulating Reflector

Bottom simulating reflectors (BSR) are the most widely used indicator for gas hydrates in marine sediments. They mark the base of the hydrate stability zone, where pressure and temperature conditions are at the phase boundary between hydrates and free gas (Fig. 1.1). Because gas hydrate stability is much more sensitive to temperature than to pressure, BSRs approximately follow isotherms. In undisturbed sediment, isotherms are parallel to the seafloor, which is why BSRs mimic the seafloor.

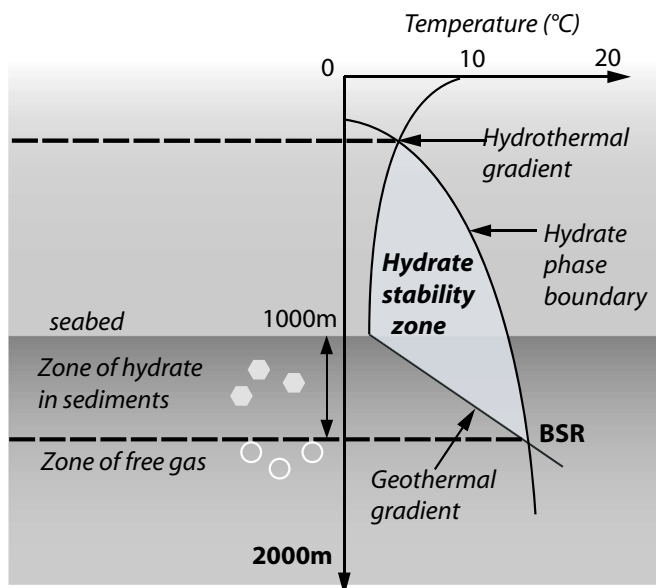


Figure 1.1: *Stability region of hydrate in seawater as defined by temperature and pressure (indicated as depth).*

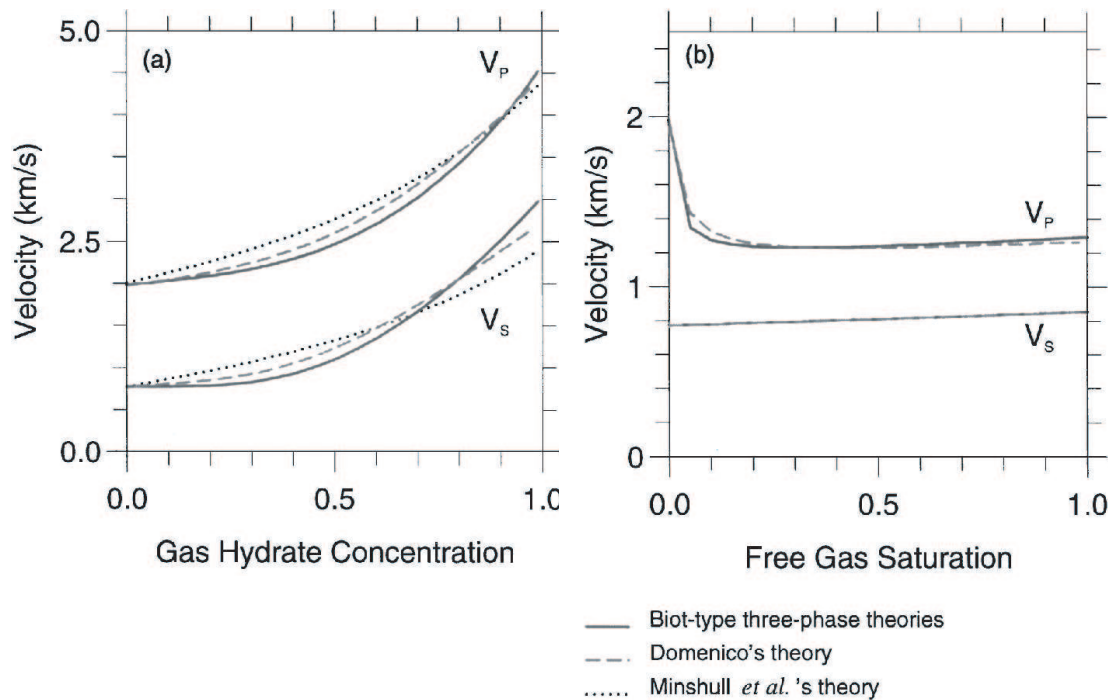


Figure 1.2: *Seismic compressional and shear velocities for a gas-hydrate bearing sediment and a free gas bearing sediment (from Carcione and Tinivella (2000)).*

Gas hydrate has a very strong effect on sediment acoustic properties because of its high acoustic velocity around 3.3 km/s (Sloan, 1998). The presence of gas hydrate in sediments increases their average velocity. Sediments below the gas hydrate stability zone, if water saturated, have lower velocities (water velocity is ~ 1.5 km/s), and if gas is trapped in the sediments below the hydrate, the velocity is much lower, even with a few percent of gas. Where no direct measurements are available, detailed knowledge of the compressional and/or shear wave velocity distribution in marine sediments is essential for the quantitative estimates of the gas hydrate and free gas saturation in the pore space. These acoustic parameters are derived from the bottom simulating reflector observed in seismic profiles by using traveltime (kinematic) and amplitude analyses (dynamic). The difference between the inverted velocity profile from seismic data and the velocity for the water-filled marine sediments are interpreted to be caused by the presence of gas hydrate (where positive anomalies are present) and free gas (where negative anomalies are present). Among others Carcione and Tinivella (2000) obtained wave velocities as a function of gas hydrate bearing sediment, which are based on theoretical rock models (Fig. 1.2).

The reflection strength for vertical incidence is proportional to the change of acoustic

impedance, which is the product of velocity and density. The base of the hydrate-cemented zone traps free gas bubbles and represents a very large change in velocity. Therefore it produces a very strong reflection, the BSR. This may or may not be a continuous reflection in seismic profiles, because the presence of gas varies laterally. Free gas at low saturations in the pore space will most likely be trapped as a cloud of isolated bubbles that will be buried with the sediment. *Henry et al. (1999)* suggest that a threshold saturation necessary for gas movement would typically be about 20%, which represents the percolation threshold for buoyant separate phase movement. As a consequence, this infers that gas is recycled into the hydrate zone (*Paull et al., 1994*). *Pecher et al. (1998)* suggest that the free gas generating the BSR probably comes from melting of pre-existing hydrate rather than representing a trapped pool that is sourced from below. This is based on the finding that on the Central and South American margins BSRs are largely confined to geological units that are downwarping tectonically or subsiding due to continued sedimentation. In this case the amount of gas is tied to the amount of hydrate that has melted to source the gas (*Dickens et al., 1997; Henry et al., 1999*).

This thesis focuses on the nature of the bottom simulating reflector, which marks the base of the hydrate bearing zone at Southern Hydrate Ridge (Fig. 1.3), offshore Oregon at the Cascadia continental margin.

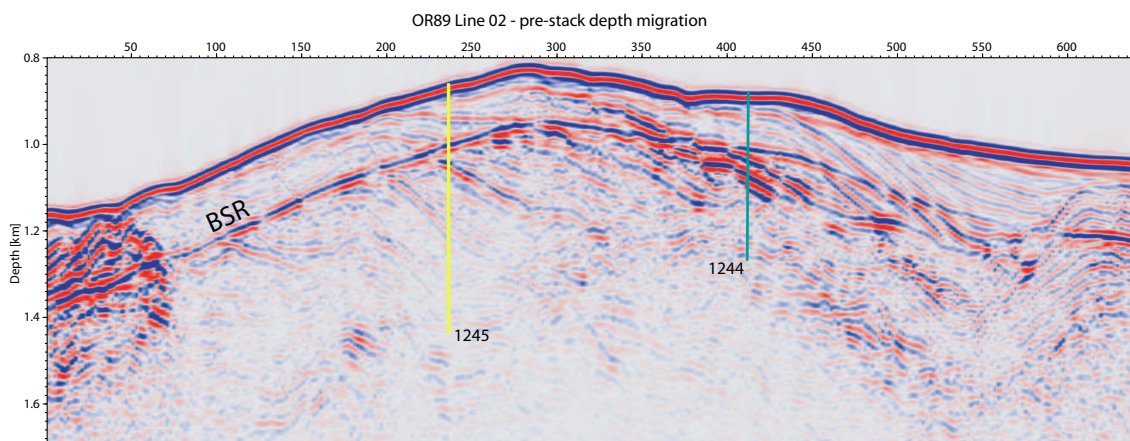


Figure 1.3: *Prestack depth-migration of line OR02 (from *Haris (2003)*) showing the BSR across the southern crest of Hydrate Ridge. The seismic line crosses two drill sites of the Ocean Drilling Program Leg 204.*

1.3 Study area: Hydrate Ridge

Hydrate Ridge, known as Second Ridge prior to the discovery of abundant massive methane hydrate at the seafloor in 1996, is a 25 km long and 15 km wide ridge in the Cascadia accretionary complex, formed as the Juan de Fuca plate subducts obliquely beneath North America at a rate of ~ 4.5 cm/y. The sediment on the subducting plate, which consists largely of turbidite beds, is accreted to the Oregon margin (*MacKay et al., 1992; MacKay, 1995*). Hydrate Ridge is located near and south of a structural transition between seaward vergent thrust packets to the south and landward vergent thrust to the north (*MacKay, 1995*). In addition to the change in tectonic style from north to south along the margin, numerous oblique strike-slip faults offset the accretionary prism (*McCaffrey and Goldfinger, 1995*).

Hydrate Ridge is characterized by a northern summit at a water depth of ~ 600 m and a southern summit at a water depth of ~ 800 m. Seafloor gas vents, outcrops of hydrate, authigenic carbonates, and chemosynthetic organisms exist on the southern and northern summits of this ridge, and a strong BSR is widespread in the area (*Tréhu et al., 2002; Clague et al., 2001; Torres et al., 2002*). The northern crest of the ridge was the site of the Ocean Drilling Program (ODP) Leg146 in 1992. Massive gas hy-

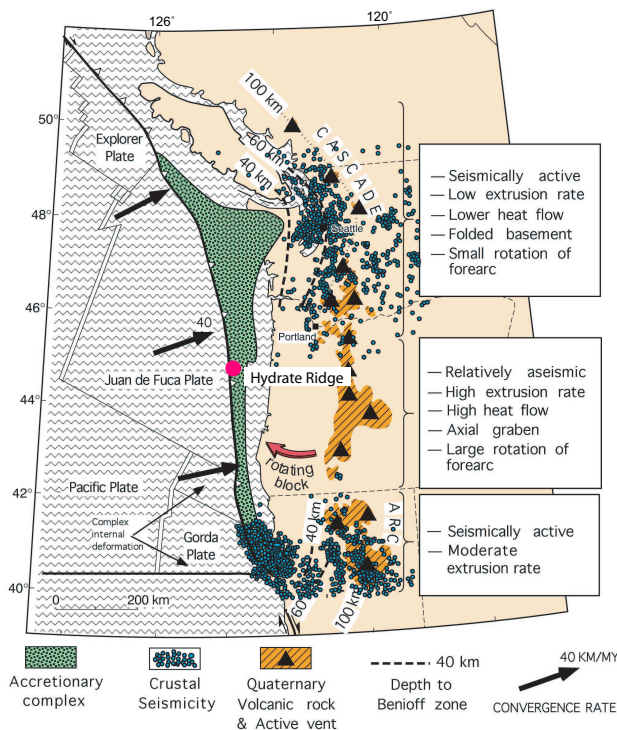


Figure 1.4: *The main tectonic units and segmentation of the Cascadia margin (from Gerdom et al. (2000)). Red circle marks Hydrate Ridge.*

drate was recovered from the southern crest in 1998 using a large video-guided grab sampler (*Bohrmann et al., 1998; Suess et al., 1999*). Since 1996, there have been several cruises per year to the northern and southern Hydrate Ridge. These cruises have collected a comprehensive swath bathymetry and a deep-towed side-scan database as well as extensive seafloor observations and sample collections by submersibles and remote vehicles (ROVs) (*Suess and Bohrmann, 1997; Clague et al., 2001; Torres et al., 1998, 1999; Bohrmann et al., 2000; Linke and Suess, 2001*). In addition, a high-resolution 3-D seismic survey was conducted in 2000 as a site survey for ODP Leg 204 (*Tréhu and Bangs, 2001; Tréhu et al., 2002*).

Hydrate Ridge was visited with R/V *Somme* in 2000 within the HYDGAS project (*Klaeschen et al., 2001*) for a comprehensive seismic study. The northern and southern crest of Hydrate Ridge was covered by numerous seismic profiles using multiple source and receiver configurations. With respect to the planned ODP Leg 204 at Southern Hydrate Ridge, and to existing multi-channel seismic data (MCS) (*MacKay, 1995*), the main seismic experiments were carried out along a line (P173) that was planned to cross two ODP Sites and that was coincident with existing MCS data of line OR02 (*MacKay, 1995*) (Fig. 1.5) This main line is subject of this thesis.

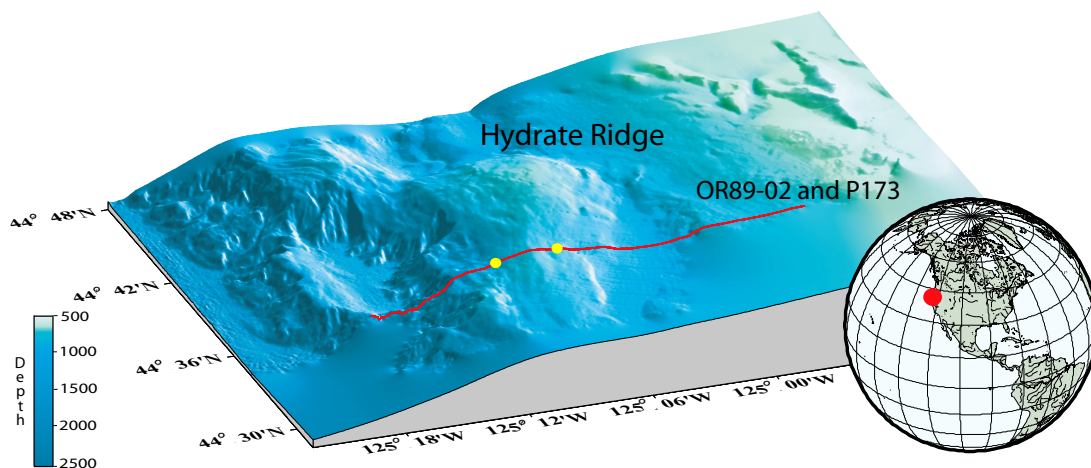


Figure 1.5: *Perspective view and bathymetry of Hydrate Ridge at the Cascadia margin offshore Oregon. The two yellow circles represent the two drill site locations of Ocean Drilling Program Leg 204 coinciding with the main seismic line, which is investigated in this study.*

1.4 Overview

This study aims at the quantification of gas hydrates by focusing on the P-wave velocity distribution within the gas hydrate stability zone. Furthermore, the possibility of a thin gas layer beneath the BSR is studied in detail by analyzing the reflecting amplitudes of the BSR in different frequency domains. Additional drill site information of the Ocean Drilling Program Leg 204 assists to verify the results of the methodological approaches, presented in this study, to describe the BSR at Southern Hydrate Ridge. The following chapter sequence is chosen for this thesis:

- **Chapter 2** describes the seismic data basis for the analysis presented in this thesis and presents the main processing steps applied to this data
- **Chapter 3** presents the combined velocity analysis of the different acquisition systems and provides an accurate velocity model along the main seismic profile
- **Chapter 4** deals with the analysis of the BSR amplitude and investigates the limitations of standard AVO analysis for a single interface
- **Chapter 5** focuses on the frequency-dependent amplitude variations at the BSR with respect to tuning effects of a thin gas layer beneath the GHSZ. At the end of this chapter the consequences of a thin layer for AVO analysis is discussed
- **Chapter 6** compares the analysis results with information available from ODP Leg 204
- **Chapter 7** concludes and provides an outlook for future seismic investigations of gas hydrate systems.

2 Data

2.1 Introduction and Research Area

The seismic data set was acquired in September 2000 at Hydrate Ridge, offshore Oregon on the continental margin of the Cascadia subduction zone. The data set was recorded during the *Sonne* cruise SO150 within the *HYDGAS* project (Klaeschen *et al.*, 2001) (Fig. 2.1), which aimed at the development of seismic approaches to characterize the gas hydrate environment. The main interest was to examine the nature of a BSR with a series of different receiver and source configurations. Several seismic lines were shot covering the northern and the southern crest of Hydrate Ridge. In this study only data of the southern ridge will be presented. The data at Northern Hydrate Ridge was investigated by Petersen (2004). The layout of the southern seismic experiments was closely linked to existing seismic multi-channel (MCS) profiles (MacKay *et al.*, 1992) and proposed drill site locations of the planned ODP Leg 204. Regional line OR02 (MacKay *et al.*, 1992) (Fig. 2.1) was revisited several times during the cruise, because two drill sites were planned along this profile. Ocean bottom hydrophones

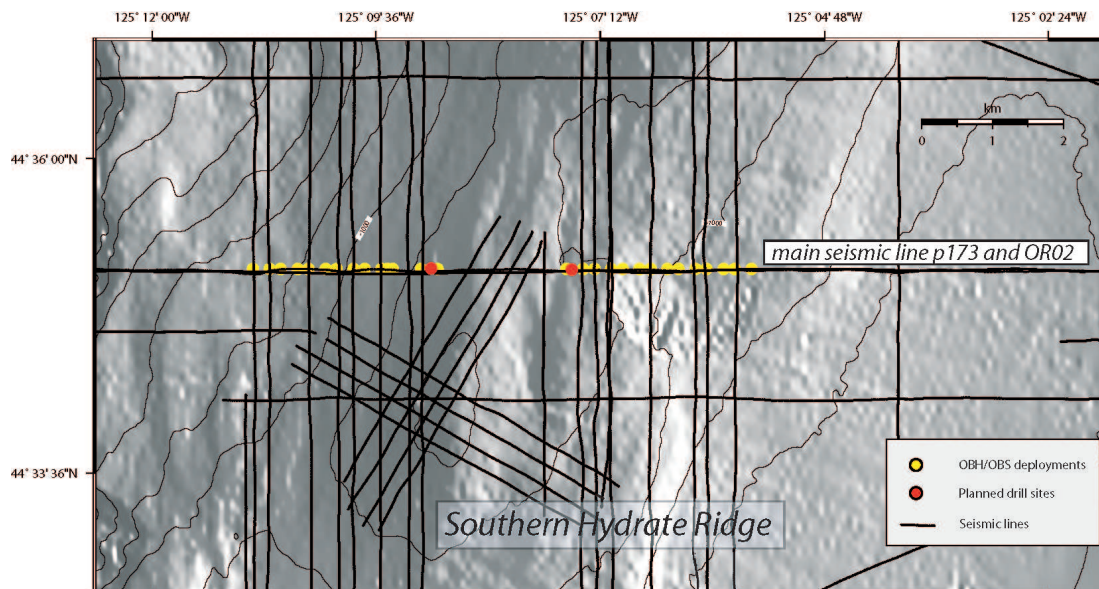


Figure 2.1: Location map of seismic lines acquired during the *HYDGAS* cruise in September 2000, and deployment of ocean bottom receivers (OBH/OBS).

and seismometers (OBH/OBS) (*Bialas and Flueh, 1999*) were deployed along this line (Fig. 2.1). The main scientific experiments were carried out, using the OBH/OBS instruments and multiple streamer seismic acquisition systems. The combination of towed streamer systems (with their limited aperture, but high lateral resolution) and OBH/OBS (without aperture limitation), offers a wide range of analysis techniques to characterize the sub surface, and especially the BSR signature. In addition to the multi-system receiver configuration five different seismic sources were used to cover a broad range of frequencies.

2.2 Data Processing

An especially designed pre-processing sequence is applied to the raw seismic data. With respect to amplitude investigations a true amplitude (TA) processing is inevitable to preserve real amplitudes. A careful geometry setup in the pre-processing steps is needed to account for the broad range of acquisition systems. The small shot-point distance (e.g., 6 m for the sparker data) allows an uncertainty of shot and receiver positions only within a few meters. The locations of the OBH/OBS and each source are derived from the data subsequently, as source and receiver positions have to be recalculated relative to the position of the vessel. Due to drifting of the OBH/OBS instruments during deployment, re-positioning of the ocean bottom instruments is performed by developing a 3-D relocalization tool. The pre-processed data is then corrected ('swell-filtered') for high-frequency trace shifts caused by undersampling of the trigger-time series and/or bad weather conditions. The main processing steps as well as data examples are presented in more detail in the following sections.

2.2.1 Pre-processing

With respect to the different acquisition systems used during the HYDAGS cruise, the processing sequences for all data were designed to satisfy the high-resolution requirements. Existing routines to automatically pre-process wide-angle seismic data had to be modified and new routines were introduced into the processing sequence. After converting the raw data to standard SEG-Y format the following processing steps were applied:

- geometry settings
- relocation of ocean bottom instruments
- frequency band-pass filtering
- swell-filtering

At this point, it should be mentioned that no signal deconvolution was applied to the data, in order to fulfill the true amplitude requirements.

2.2.2 Geometry considerations

Relocation of ocean bottom instruments

During the deployment of OBH/OBS, stations may drift laterally more than 100 m, caused by currents in the water column, as they descend to the seafloor. The method to relocate the exact positions of the drifted OBH/OBS is based on the relationship between the recorded traveltimes of the direct arrival and the exact shot point geometry (*Zelt and Barton, 1994*). The existing relocalization algorithm is restricted only to two dimensions and does not produce the accuracy needed for the high-resolution data set. Several iterative applications are necessary to determine the exact position. Instead, a 3-D approach is developed to relocate the OBH/OBS in three dimensions. Based on the known traveltimes of the direct arrivals along three profiles, exact positions can be computed by

$$t(x, y, z) = \frac{1}{v} \sqrt{x^2 + y^2 + z^2}$$

$$\sum_{i=1}^n \left(\frac{1}{v} \sqrt{x_{obs}^2 + y_{obs}^2 + z_{obs}^2} - \frac{1}{v} \sqrt{x_{picks_i}^2 + y_{picks_i}^2 + z_{obs}^2} \right) = MIN$$

$$MIN \Rightarrow X_r, Y_r, Z_r$$

where

$$\begin{aligned} t(x, y, z) &= \text{traveltime [s]} \\ v &= \text{sound velocity of water (= 1480m/s)} \\ x_{obs}, y_{obs}, z_{obs} &= \text{OBH/OBS position} \\ x_{picks}, y_{picks} &= \text{coordinates of picked traveltimes [m]} \\ X_r, Y_r, Z_r &= \text{relocated coordinates [m]} \end{aligned}$$

In addition to the main seismic line along the deployed OBH/OBS, several cross lines (Fig. 2.1) were acquired to obtain the necessary 3-D information for the relocalization process. Figure 2.2 shows schematically the geometry used for the relocalization process. The water velocity is set constant to 1480 m/s. This information is derived from a Conductivity Temperature Depth (CTD) measurement (Fig. 2.4). The relocated depths of the OBH/OBS are compared to the respective depth in the high resolution bathymetry. The predicted error within the coordinate-determination is less than 5 m, so that the final positions can be determined within a 5 m × 5 m × 5 m cube. In Figure 2.3 the positions before and after relocalization are plotted over the ships track

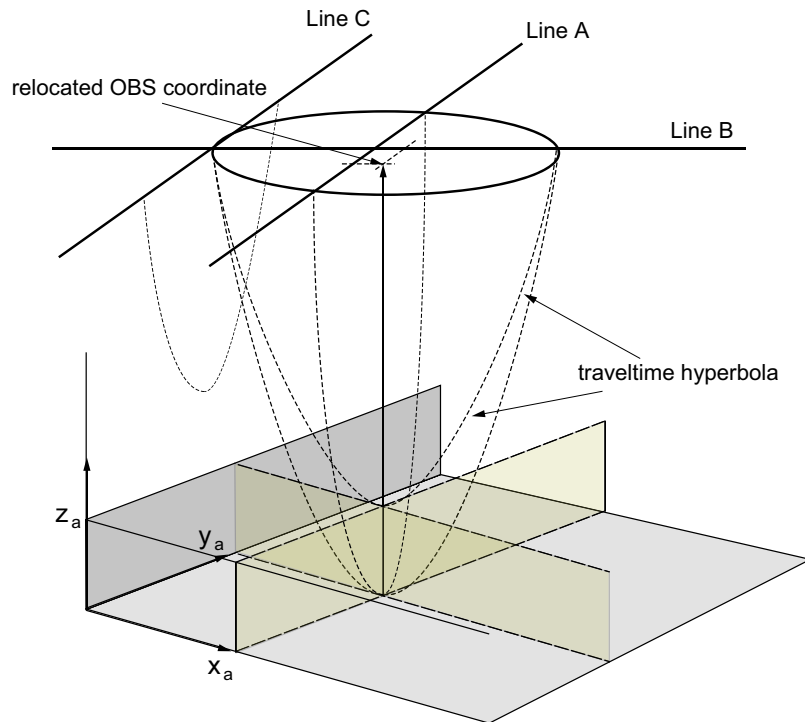


Figure 2.2: *Traveltime hyperboloids to relocate drifted OBH/OBS.*

of line p173. All OBH/OBS have apparently drifted approximately 100 m to the north. Special attention is paid on OBHs that were not deployed directly on the seafloor. Along the main profile p173, three instruments (OBH 60, 65, and 66) were deployed 200 m above the seafloor (OBH at rope). These instruments are necessary to record the direct arrival and the seafloor reflection separately. At instruments deployed on the ocean floor, the direct wave and the seafloor reflection interfere and consequently amplitude and phase information are difficult to separate. True amplitude reflections of the seafloor are only derived from OBHs deployed above the seafloor. This is necessary for the calculation of the reflection-coefficients during the amplitude analysis.

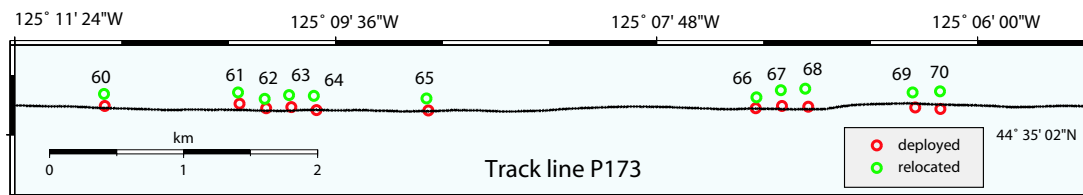


Figure 2.3: *Main seismic line p173 with locations of deployed and relocated positions.*

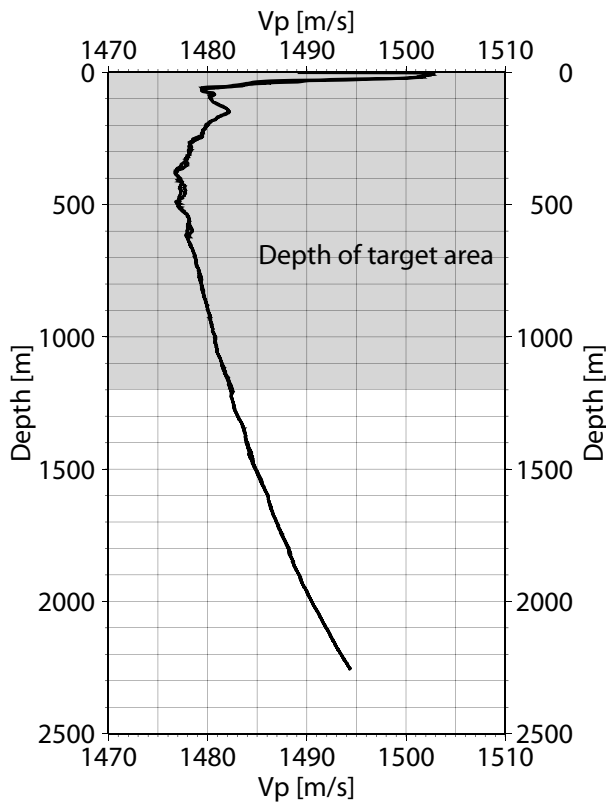


Figure 2.4: *Sound profile of the water layer derived from a conductivity temperature depth (CTD) measurement. The water depths of the target area (shaded area) are between 800 and 1200 m and the average sound velocity of the water layer is about 1480 m/s.*

Unfortunately the relocated positions of these stations are ambiguous. Changing water currents during the acquisition of two lines probably result in two different positions. The main line was shot several times, each time with a different source. The OBH floating 200 m above the seafloor recorded shots from all lines over a period of several days. For seafloor-based stations the relocated positions fit the arrival times of all lines. Only the OBH floating 200 m above the seafloor exhibits different OBH positions during the relocalization process. Table 2.1 presents the comparison of the recalculated position depths to the bathymetry and the offline distance of the OBH/OBS to the main seismic line p173. The bathymetry is computed by importing the sound-velocity profile, derived from the CTD measurement (Fig. 2.4).

OBH/S	60	61	62	63	64	65	66	67	68	69	70
Depth reloc.[m]	918	1049	1051	991	967	663	626	850	919	1001	1015
Depth bathym.[m]	1168	1057	1056	1001	971	917	831	859	1024	1003	1022
Offline [m] p173	105	131	89	116	104	94	83	141	153	84	97

Table 2.1: *Recalculated position depths of the OBH along seismic line p173 and depth derived from the bathymetry data. The average offline distance from the OBH/OBS to the main seismic line is roughly 100 m. OBH 60, 65, and 66 were deployed \sim 200 m above the seafloor.*

2.2.3 Frequencies

At Southern Hydrate Ridge four different seismic sources were used during acquisition to image the BSR with a wide range of frequencies (Fig. 2.5). The broad frequency content of each source is determined and main signal frequencies (Tab. 2.2) are calculated from primary signal phases. The seismic data are frequency filtered by applying a band-pass Ormsby-filter to increase the signal/noise ratio. Before filtering, various band-pass filters were tested for preserving true amplitudes and phases, only the Ormsby-filter satisfies the true-amplitude requirements. Figure 2.5 shows the signal wavelets of all four sources. The signals vary in their frequency content (compare Tab. 2.2), which is displayed above each panel. The grey shaded area in the frequency-window represents the spectrum of the entire wavelet including the so-called bubble pulse. These bubble pulses are caused by the oscillating bubble, generated by marine explosive-type sources. The primary pulse of each source is displayed in the inlet panel of Figure 2.5. The black line, lying over the grey shaded spectra represents the frequency-distribution of the primary signal, thus without the frequency content of the bubble. The bubble pulse is responsible for the low-frequency content, resulting in low-frequency spikes. The bubble pulse of the Bolt-gun and the airgun signal occurs 160 ms and 100 ms after the primary pulse, respectively (Fig. 2.5). The frequency range of the Bolt-gun signal can be split up into two dominant frequency ranges. A high frequency part, defined by the first (positive) phase and a low-frequency part, caused by the second (negative) and more

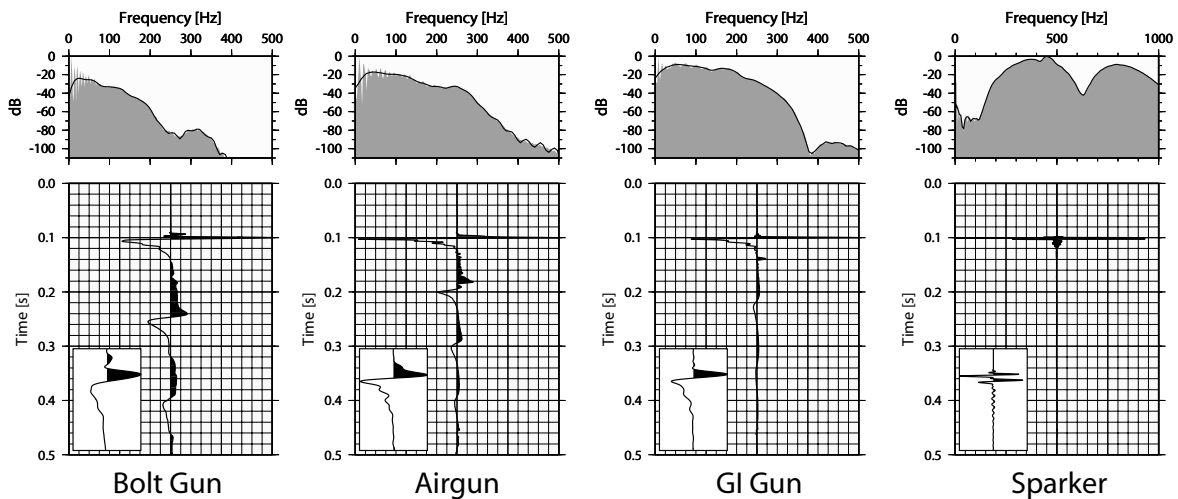


Figure 2.5: *Seismic wavelets, recorded with the surface streamer, towed at 5 m depth. In the upper panels, the power spectra are displayed for each source. The grey shaded area represents the entire wavetrain, including the bubble pulse, whereas the black line represents the frequencies of the primary signal, displayed in the inlet panels.*

Source	main freq.	wavelength	FZ_{SCS}	FZ_{OBS}	shot rate	shot dist
Bolt-gun	80 Hz	19 m	136 m	22 m	17 sec	35 m
Airgun	100 Hz	15 m	122 m	19 m	10 sec	20 m
GI-gun	150 Hz	10 m	100 m	14 m	7 sec	15 m
Sparker	300 Hz (1st phase)	5 m	70 m	8 m	3 sec	6 m

Table 2.2: *Dominant frequencies of the seismic sources, used during the HYDGAS cruise. Fresnel zones of surface and seafloor receiver configurations as well as shot distances are given.*

complex phase, which is similar to the bubble frequency. The primary phase frequency of 80 Hz is similar to that of the airgun of 100 Hz. The GI-gun (*Generator-Injector gun*) comprises two airguns. The first gun, the generator, produces the primary pulse, whereas the second gun, the injector, is triggered after a delay to suppress the bubble. Although the bubble was successfully suppressed, a remaining phase is clearly visible at about 35 ms after the primary pulse, presumably caused during the injection phase. The signal wavelet of the sparker data consists of two double-phases. This is caused by another typical effect, when using marine sources. If the source and receiver are deployed within a few meters below the sea surface, the generated pulses are reflected at the sea-surface in addition to the direct "down-going" signal, and both interfere to a mixed primary pulse (Fig. 4.6). The so-called ghost-effect is observed at the receiver, which in case of a surface streamer, is floating a few meters below the sea surface. Reflections arriving from the subsurface are passing the receiver twice; once directly from below and again from the sea-surface reflection, which can be a few milliseconds later, depending on the towing depth of the streamer. Consequently, ocean bottom instruments and deep-towed systems are only affected by the source-type interference, the source-ghost. The source signals presented in Figure 2.5 are derived from the single channel streamer, towed approximately 5 to 10 m below the sea-surface. In the sparker

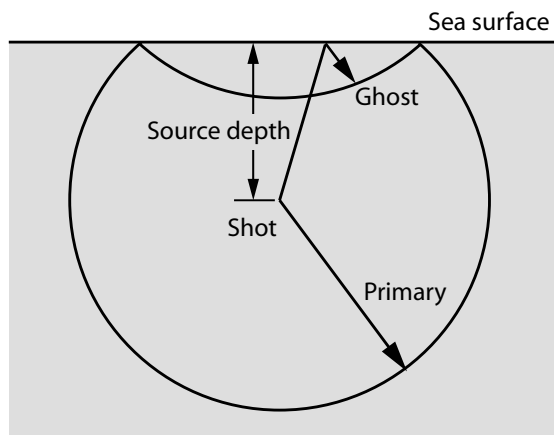


Figure 2.6: *A marine source towed at depth behind the vessel produces a direct down-going pulse and secondary "source ghost" caused by the reflection of the direct up-going pulse from the free surface.*

data, the reflected receiver-ghost arrival and the primary arrival do not interfere and two almost separated phases were recorded. The ghost-interference creates a notch within the power spectrum, as it is observed at approximately 650 Hz in the spectrum of the sparker data and 380 Hz in the spectrum of the GI-gun data.

This detailed analysis of the source signals and signal-spectra is necessary, because no signal deconvolution is applied to the data, and phase identification is crucial for arrival picking and amplitude analysis, presented below. A more detailed description of marine seismic sources and signals can be found in (e.g., *Larner et al., 1982; Hargreaves, 1992; Hamarbitan and Margrave, 2001; Johnson, 1994; Ziolkowski, 1970, 1998*).

The Fresnel zone is related to the source frequency and therefore the signal wavelength. While the wavelength is a measure for vertical resolution, the Fresnel zone describes the horizontal resolution. The width Z of the Fresnel zone for a surface source and receiver is related to the dominant wavelength λ of the source and the reflector depth d after *Sheriff (1980)*:

$$Z \approx \sqrt{2d\lambda} \quad (\text{for } Z \gg \lambda)$$

The Fresnel zone can be decreased (*Otterbein, 1997*), by lowering the receiver closer to the target, as is the case for ocean bottom instruments. The effect of two receivers at different depths on the Fresnel radius is displayed in Figure 2.7. The red line represents the conventional streamer floating at the sea surface, whereas an ocean bottom instrument is represented by the blue curve. For a given reflector depth (~ 1000 m within this study) the Fresnel zone is reduced dramatically at higher frequencies (= smaller wavelengths). Comparing the single channel streamer (SCS) (Fig. 2.7, blue line) to OBS (Fig. 2.7, red line) geometry, the lateral resolution is improved by using a OBH/OBS geometry.

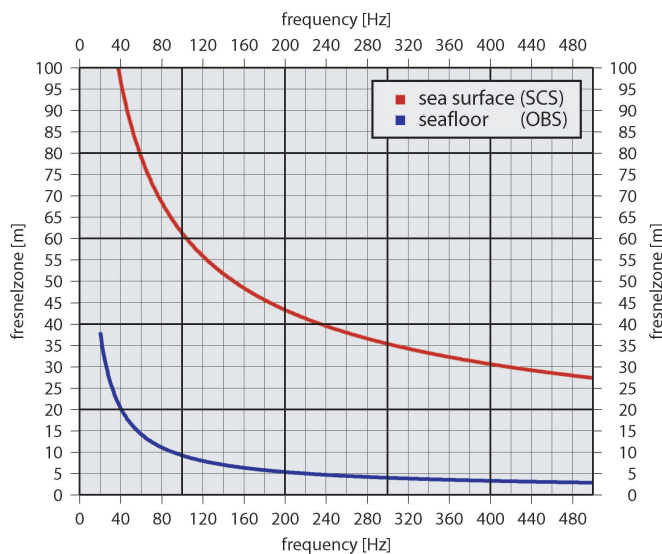


Figure 2.7: *Effect on the frequency/wavelength-dependent Fresnel radius of two different receiver configurations. The red line represents the surface streamer and displays larger Fresnel radii than ocean bottom station (OBS, blue). The Fresnel zones were calculated for a target depth of 1000 m.*

2.2.4 Swell-filtering

After applying all necessary geometric corrections and frequency-filtering, all data is analyzed for possible small-scale heterogeneities in the reflection arrivals. These anomalies occur in the seismogram and are caused by bad weather conditions. During data acquisition vertical changes of the seismic source depth in consecutive shots, caused by rough sea (swell), generate a small-scale shift of consecutive traces, and consequently the coherency of seismic reflectors in the seismogram is reduced. In the case of high-frequency data, like the sparker data, coherency is completely lost. To better illustrate this behavior, an example is given in Figure 2.8. In order to increase the coherency, a swell-filter is designed. Two main algorithms are incorporated into the swell-filter procedure: (1) an automatic so-called first-arrival picker and (2) a conventional 1-D filter-operator. A first-arrival picker is developed, based on the C-code routines provided by the Seismic Unix software package (*Cohen and Stockwell, 2001*). The first-arrival picker is designed to pick the first occurrence of one defined amplitude value (threshold) for all traces. Once the polarity and threshold amplitude is defined interactively, the entire seismic section is then picked automatically. The output file is an ascii-file, which contains the traveltimes-picks of each trace. As the name 'first-arrival-picker' suggests, this process only works for first arrivals. Therefore only the seafloor/direct wave of the streamer/OBH data is picked automatically. Fortunately the signal to noise ratio is of good quality and almost each trace is correctly picked. The resulting ascii-file, containing the picks as 1-D time-series is then filtered in the time-domain using a gaussian-type filter-operator. The filter length is selected to the appropriate Fresnel zone of each seismic source (*Thore and Juliard, 1999*). The average deviation between the filtered (smoothed) time-series and the original picked time-series is approximately one millisecond, with single peak values of two milliseconds. Finally, the swell-filtering process statically shifts the data, trace by trace, by the time of the deviation values. The seismic section of Figure 2.8 after application of the swell-filter is displayed in Figure 2.9. Smoothing the data is inevitable to accurately image the subsurface within the migration process and to confidently identify arrivals for the traveltimes inversion.

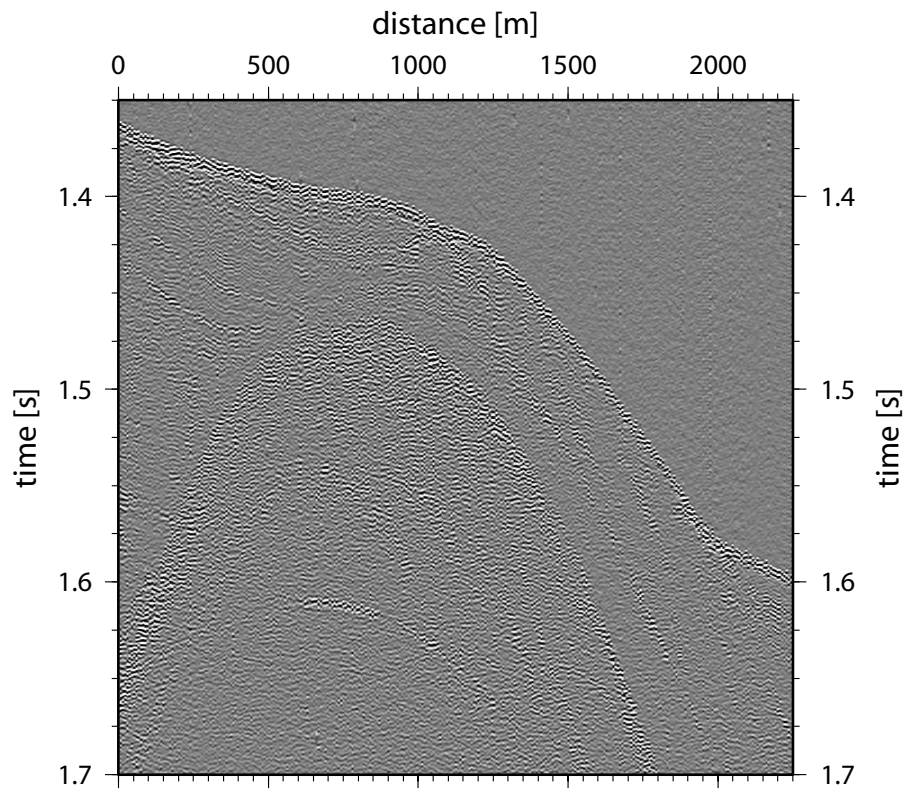


Figure 2.8: *Close-up of SCS line 171 shot with the high-frequency sparker. The small-scale heterogeneities are clearly visible at the seafloor. The coherency of reflectors in the subsurface is almost lost.*

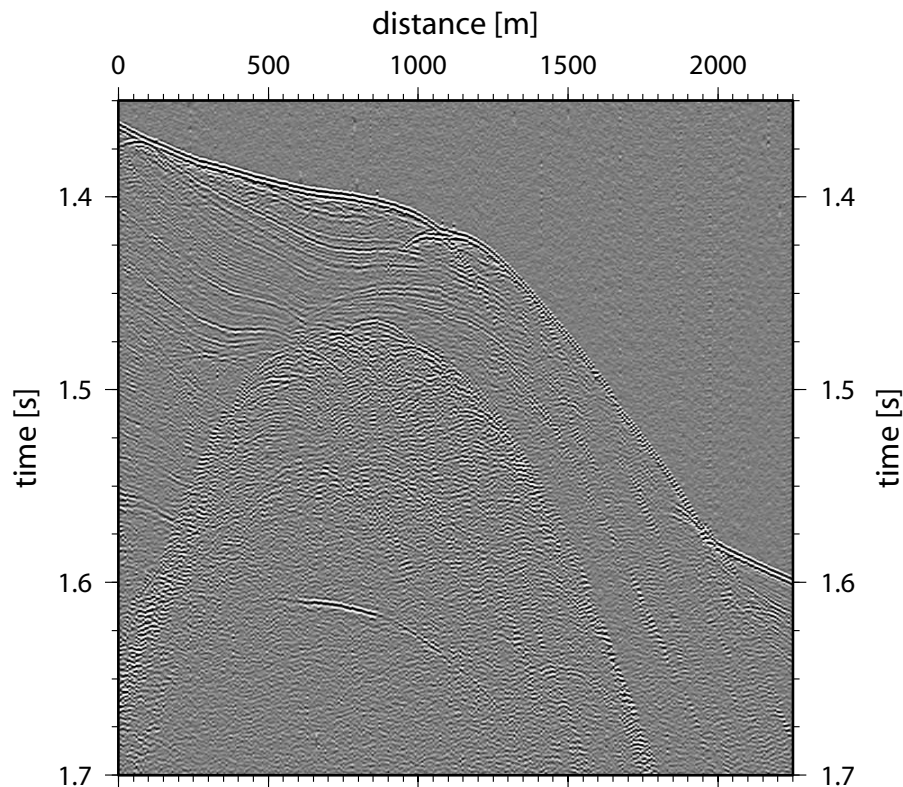


Figure 2.9: *Close-up of SCS line 171 shot with the high-frequency sparker. In comparison to Fig. 2.8 the section is well-filtered, consequently the coherency is increased.*

2.2.5 Data

Single channel streamer data

For the velocity and amplitude analysis in Chapter 3 and Chapter 4 mainly line p173 (Gi-gun) is investigated and the coincident lines shot with the airgun (p172) and sparker (p171). Coincident line p181, shot with the Bolt-gun, is not included in the majority of the investigations because the bubble pulse unfortunately coincides with the arrival of the BSR at approximately 160 ms two-way-traveltime below seafloor (TWT bsfl) (Fig. 2.10). In the airgun and the GI-gun data the BSR is clearly visible approximately 160 ms below the seafloor. The BSR seems to disappear in the sparker data, where it reflects only locally on the western flank with a weak amplitude. In general, the reflection pattern of the airgun, Boltgun, and Gi-gun data are similar in strength. Only the amplitudes of the high frequency data are apparently attenuated at greater depths. The data presented in Figure 2.10 are still unmigrated and to better image the sub seafloor and the BSR, a 2-D time migration (Stolt method) with a constant velocity of 1500 m/s is applied to the seismic data set. Prior to the migration process traces are interpolated to avoid spatial aliasing. Especially the high-frequency sparker data show strong spatial aliasing-effects of moderate dips (*Yilmaz, 1987*). The trace-interpolation and the subsequent 2-D time-migration was carried out using Schlumberger's SEISMOS processing package. The trace interpolation module is divided into two components: the dip analysis and the actual interpolation. A dip-field is determined and interpolation is performed linearly along these estimated dips. The effort being made during the swell-filtering process is necessary, because trace-interpolation only works properly when the seismic reflectors are coherent in their phases.

The time-migrated sections of the four seismic lines presented in Figure 2.10 are displayed in Figures 2.11 and 2.12. The main geologic features, which can be observed in the seismograms are discussed in Chapter 6, where additional drill information of ODP leg 204 is integrated in the discussion.

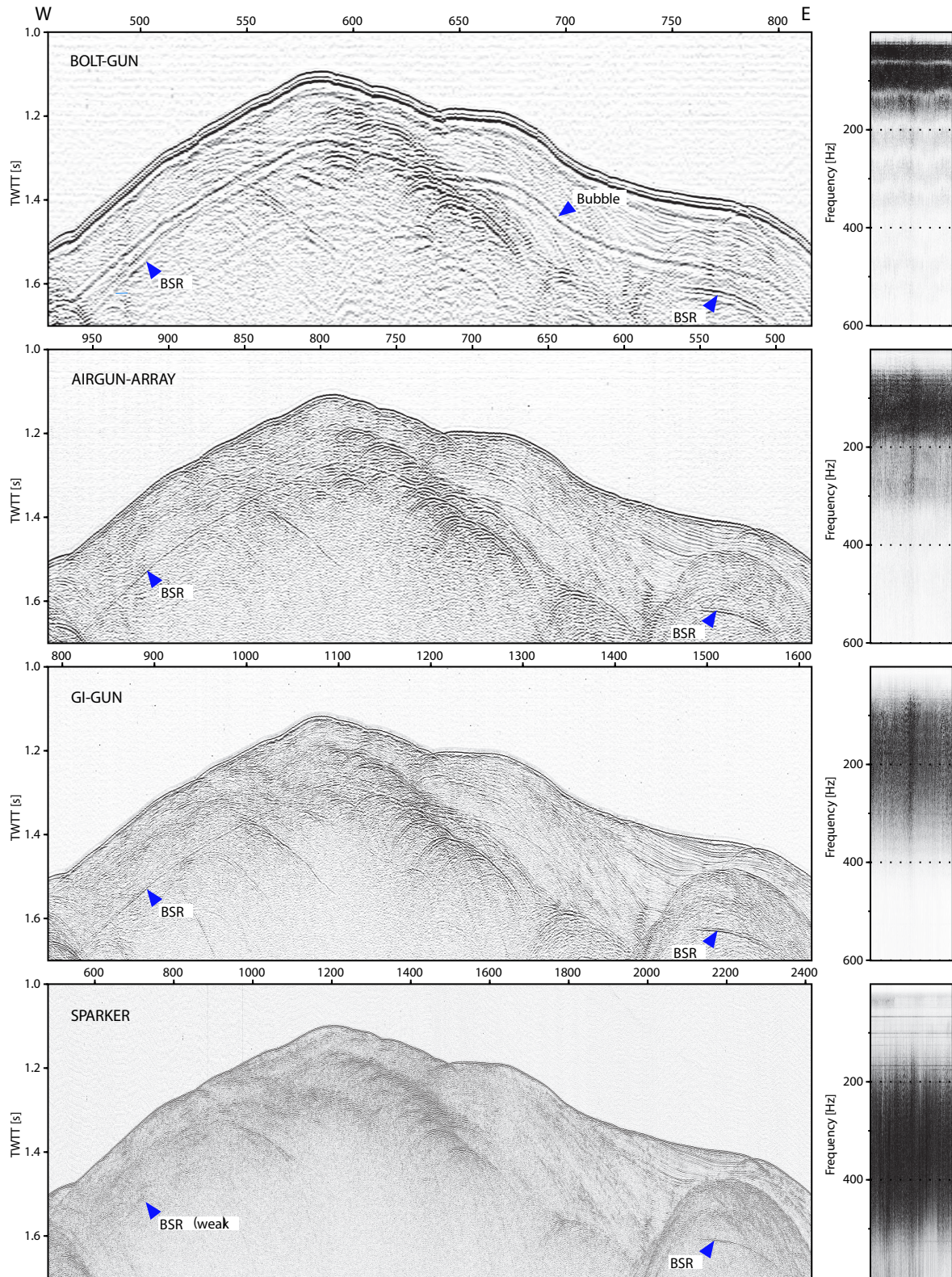


Figure 2.10: *Seismic single channel streamer (SCS) sections of the main seismic line. From top to bottom: Bolt-gun, airgun, GI-gun and sparker. The panels on the right of each seismic section display the frequency content of each source. Note how the BSR disappears at higher frequencies. The bubble pulse in the Bolt-gun data nearly coincides with the BSR.*

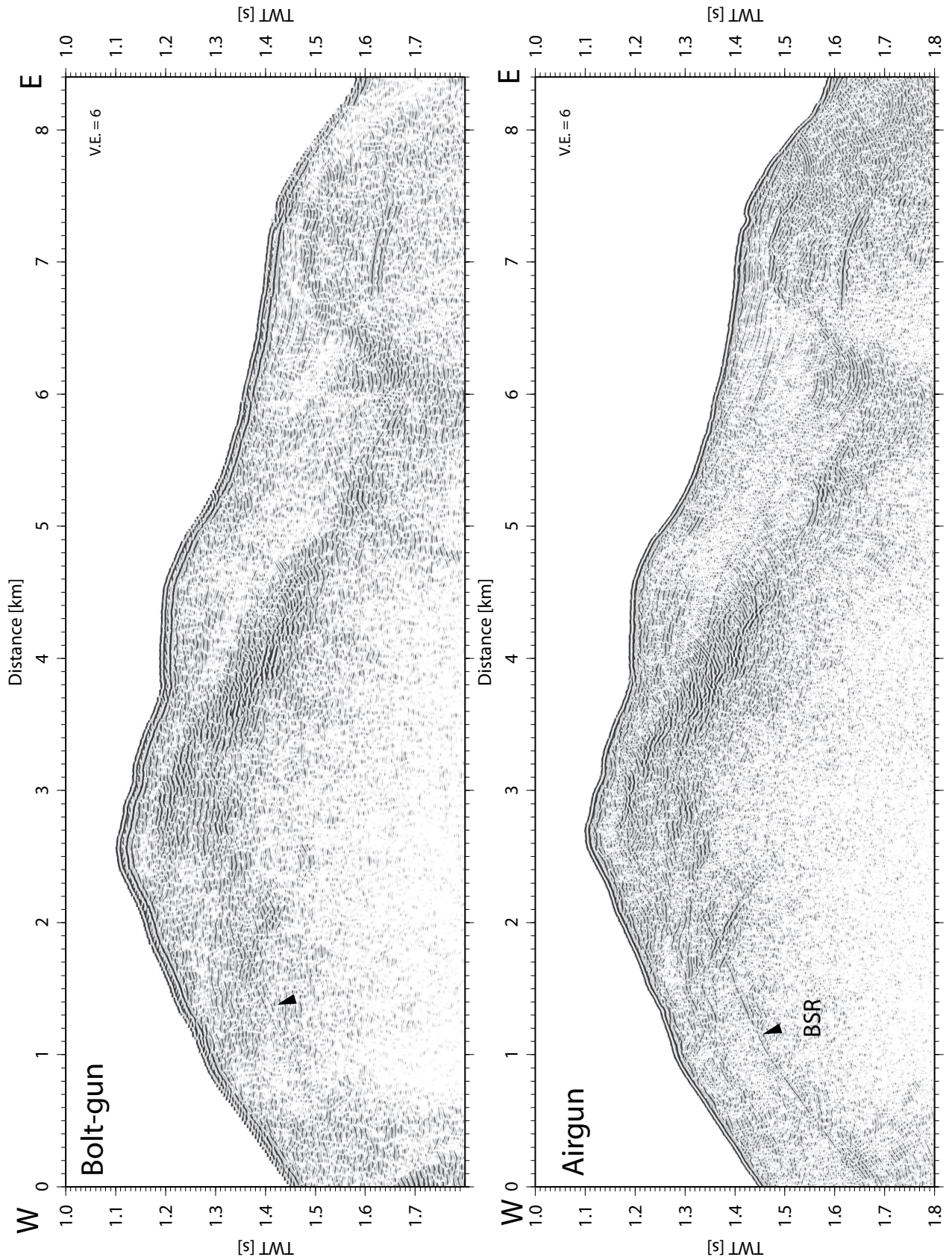


Figure 2.11: Time-migrated seismic section of the main seismic line p173. (Stolt migration with a constant velocity of 1500 m/s). Data of the Bolt-gun (top) and airgun (bottom) are displayed.

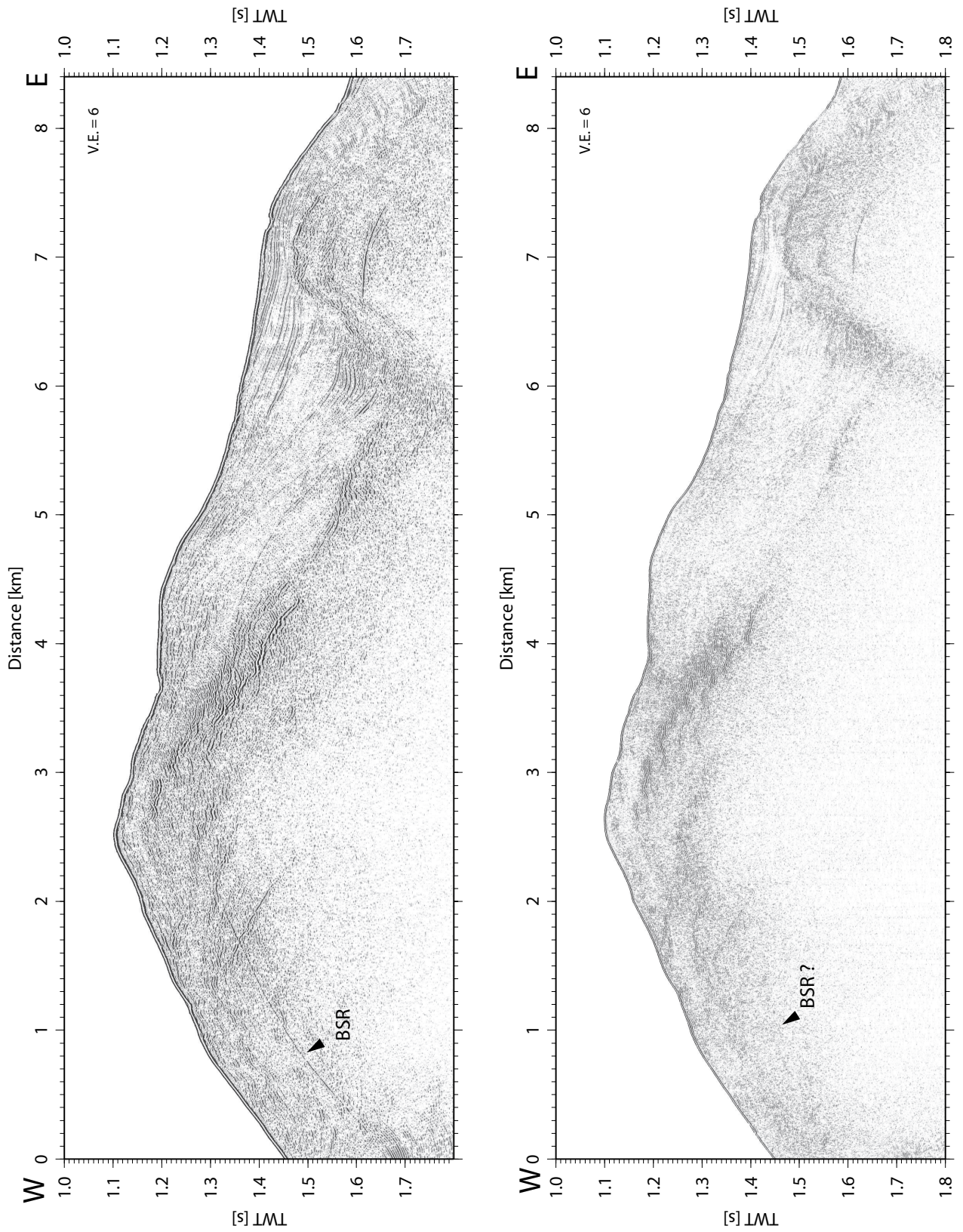


Figure 2.12: *Time-migrated seismic section of the main seismic line p173 (Stolt migration with a constant velocity of 1500 m/s). Data of the GI-gun (left) and sparker (right) are displayed.*

Ocean bottom station data

Ten OBH/OBS were deployed along the main line p173 to record wide-angle reflections from shots of the GI-gun, airgun, Bolt-gun, and sparker, respectively. For reasons, mentioned above, the Bolt-gun data is neglected for further investigations and is not further described. In general, the OBH and OBS data are of good quality, once the low-frequency noise is cut off. An example of a raw OBS seismic data set (OBS 62) is displayed in Figure 2.13.

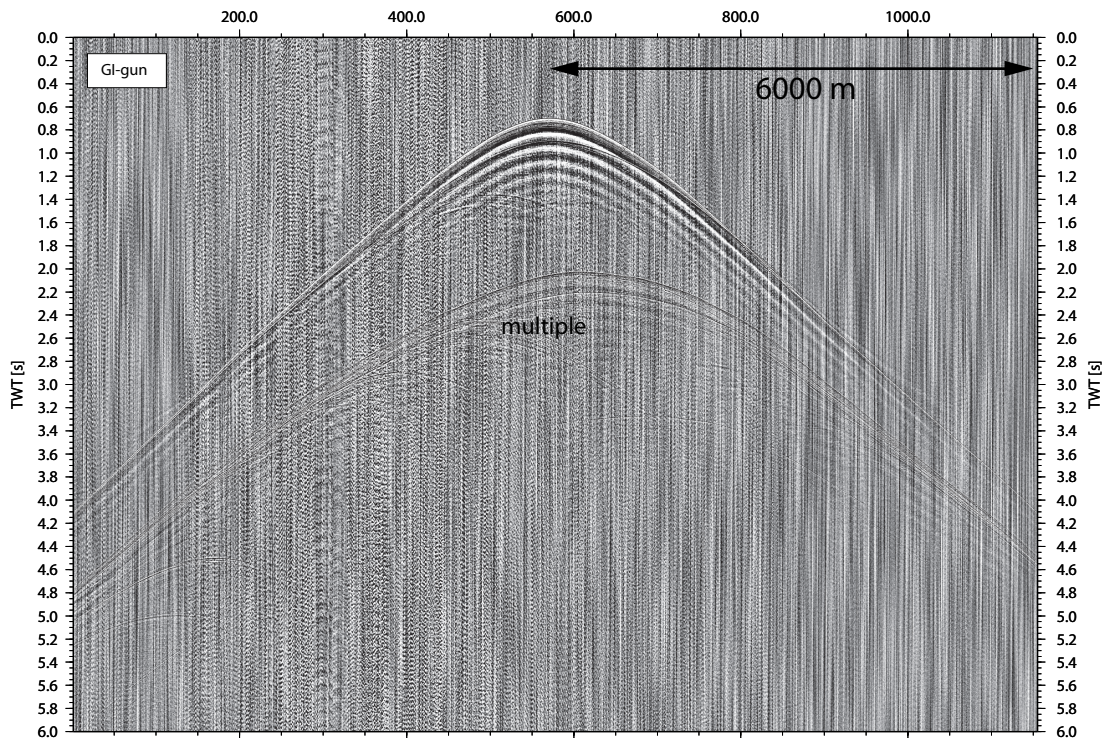


Figure 2.13: *Raw seismic section of OBS 62 (hydrophone component) shot by the GI-gun (line p173). The data are dominated by low frequency energy following the direct arrival.*

The OBS was deployed at a depth of 1051 m that corresponds to the first arrival of the direct wave at 0.71 s one-way traveltime. The data are dominated by a low frequency content, following the direct arrival. This noise is presumably caused by the strong and unattenuated direct arrival energy, which produces an analog overdriving of the hydrophone. This is not unusual, as the main interest lies on the reflection amplitudes from the subsurface, which are of one magnitude smaller. The analog data are pre-amplified by a factor that yields a most effective dynamic amplitude range of the subsurface reflections. Consequently, the direct wave amplitudes move out of the measurable amplitude range (limited by the 16-bit data logger). Hence the data of

the direct arrivals are being 'clipped'. The low frequency noise is cut off during the frequency-filtering sequence and the signal to noise ratio is clearly improved. Subsequently, the data is swell-filtered and statically corrected for a hyperbolic moveout. This process is used to statically 'flatten' the direct arrival to a constant travelttime (Fig. 2.14 and 2.15). This method is a useful tool to enhance the coherency of the re-

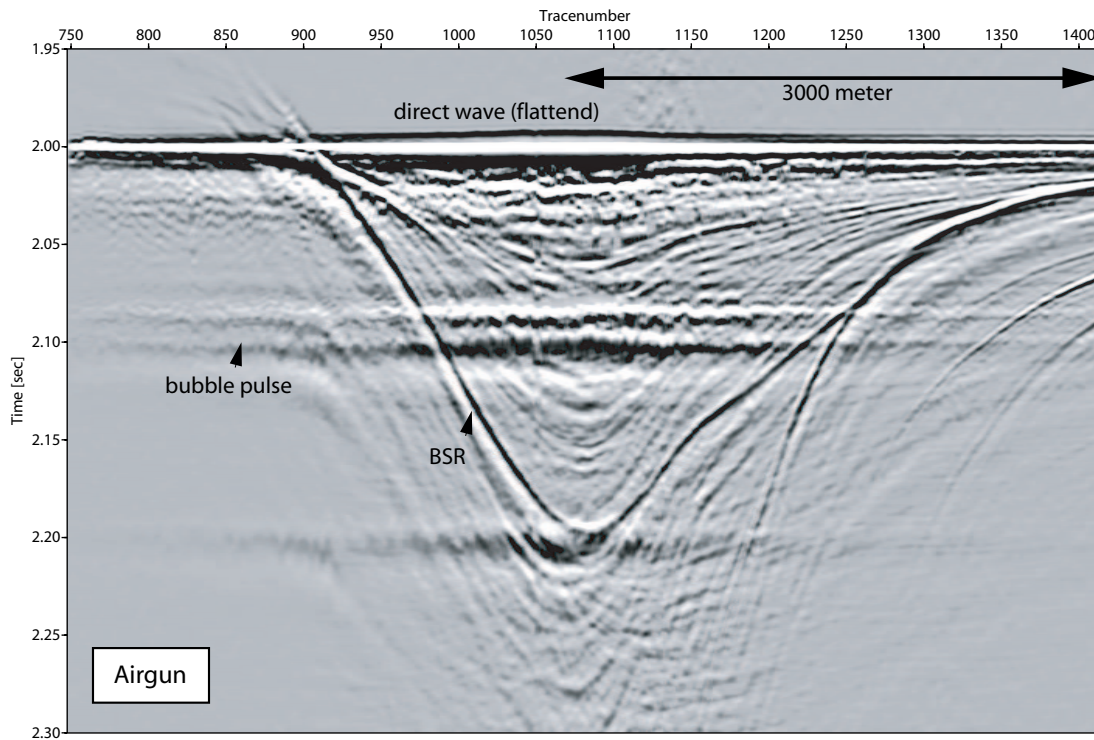


Figure 2.14: *Seismic section of OBS 62 (hydrophone component). The data are statically shifted with a hyperbolic moveout to flatten the first arrival (direct wave) to a constant travelttime (2 s). The data were shot with the airgun from west to east. A bubble pulse is clearly visible at ~ 80 ms behind the direct arrival. The data are sorted by shotnumbers and deviations within the ship's track are visible as asymmetric hyperbolas (most distinct in the BSR on the right side).*

flected arrivals. The strongly dipping reflection hyperbolas in the raw data are 'spatial' aliased (Yilmaz, 1987), which makes it difficult to confidently identify single reflectors. After the static shift the reflection amplitudes of the BSR can now be traced along the entire offset section. A clear phase reversal is observed, when comparing the direct arrival with the BSR reflection. Assuming a positive impedance contrast at the seafloor, which is usually the case, the BSR is then defined as a negative impedance contrast. In general, this is linked to a velocity inversion, generally caused by the presence of free gas below the BSR.

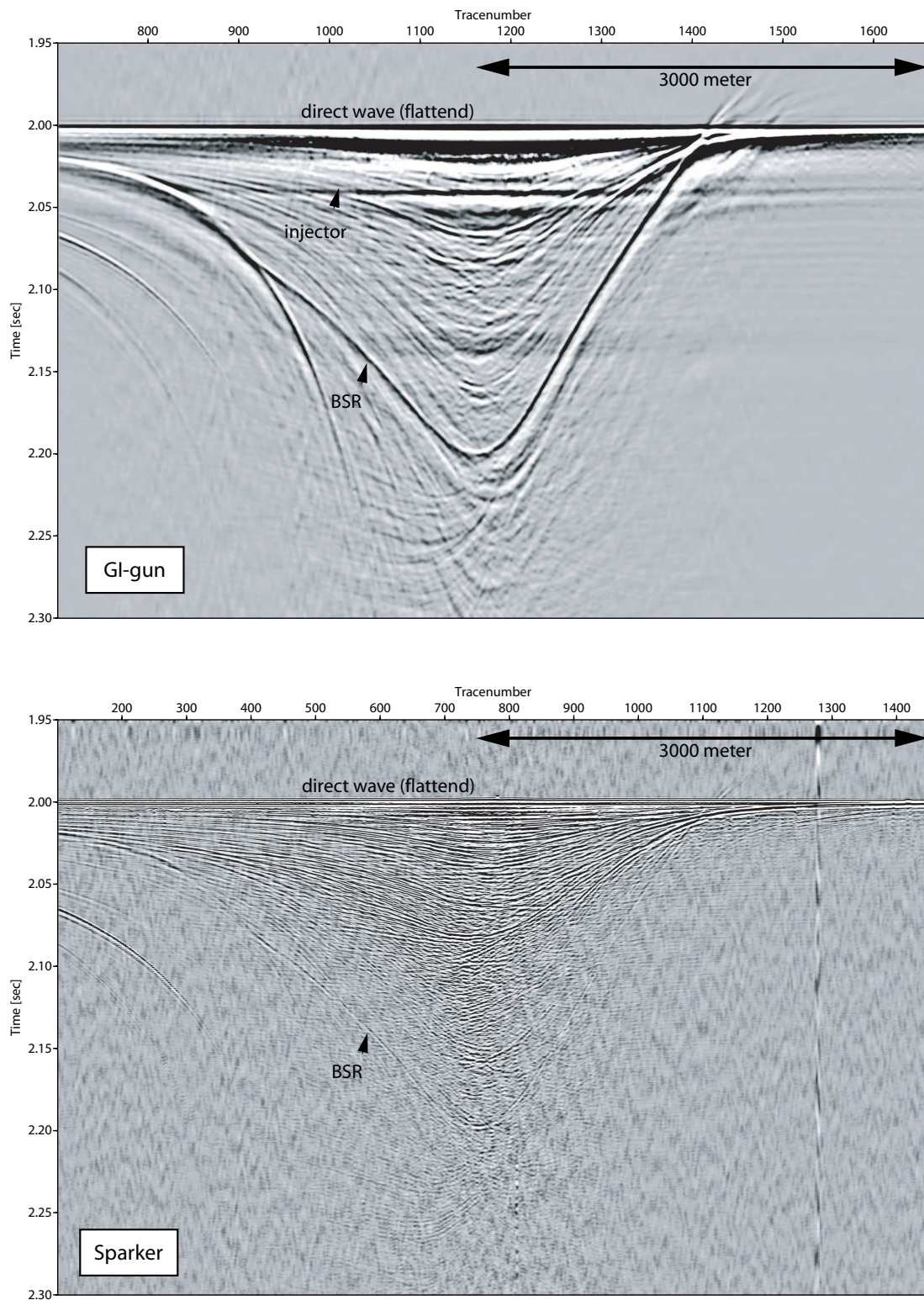


Figure 2.15: Seismic OBS sections (OBS 62:hydrophone) shot by the GI-gun (upper panel) and the sparker (lower panel). These lines were shot in the opposite direction (W-E) compared to the airgun data (Fig. 2.14). The BSR is clearly visible in the GI-gun data, whereas it is weak in the sparker section.

Deep tow streamer data

The streamer was towed with a constant cable length of 1000 m, resulting in a traveltime for the direct wave of 0.67 s with a water velocity of 1480 m/s. The calculation is restricted to an area of a relatively plane seafloor. The position of the deeptow sensor (hydrophone) is determined numerically by traveltime calculations of direct and seafloor reflection arrivals (Fig. 2.16) and averaged to a resulting depth of 281 m below sea surface and a towing distance of 963 m behind the ship. The derived geometry is used to calculate a migrated section (Fig. 2.17), using a 3D Kirchhoff prestack depth migration with a constant velocity of 1480 m/s. Although uncertainties of the sensor position have to be considered due to changes of the ships speed, the migration process results in an accurate image of the subseafloor.

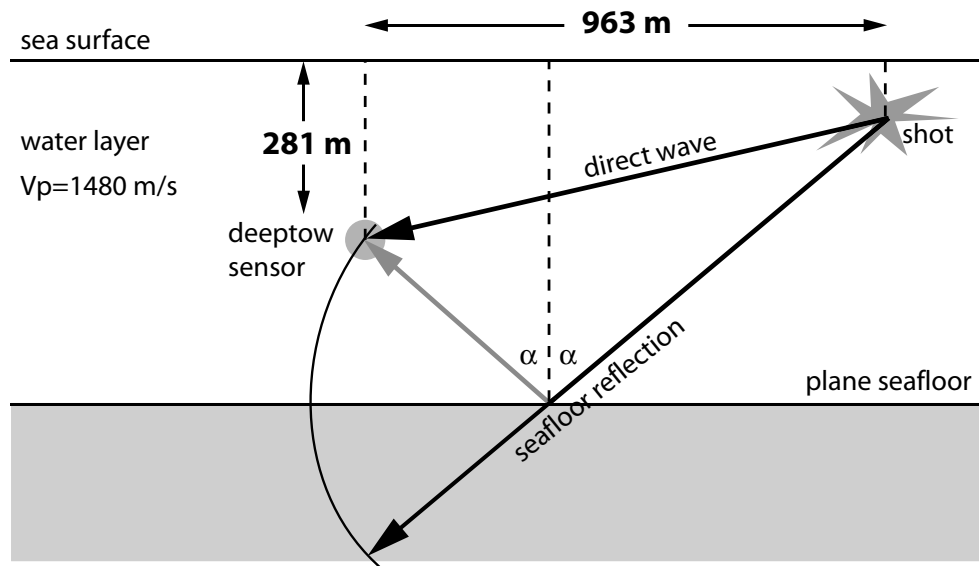


Figure 2.16: *Schematic setup for the calculation of the deeptow streamer geometry.*

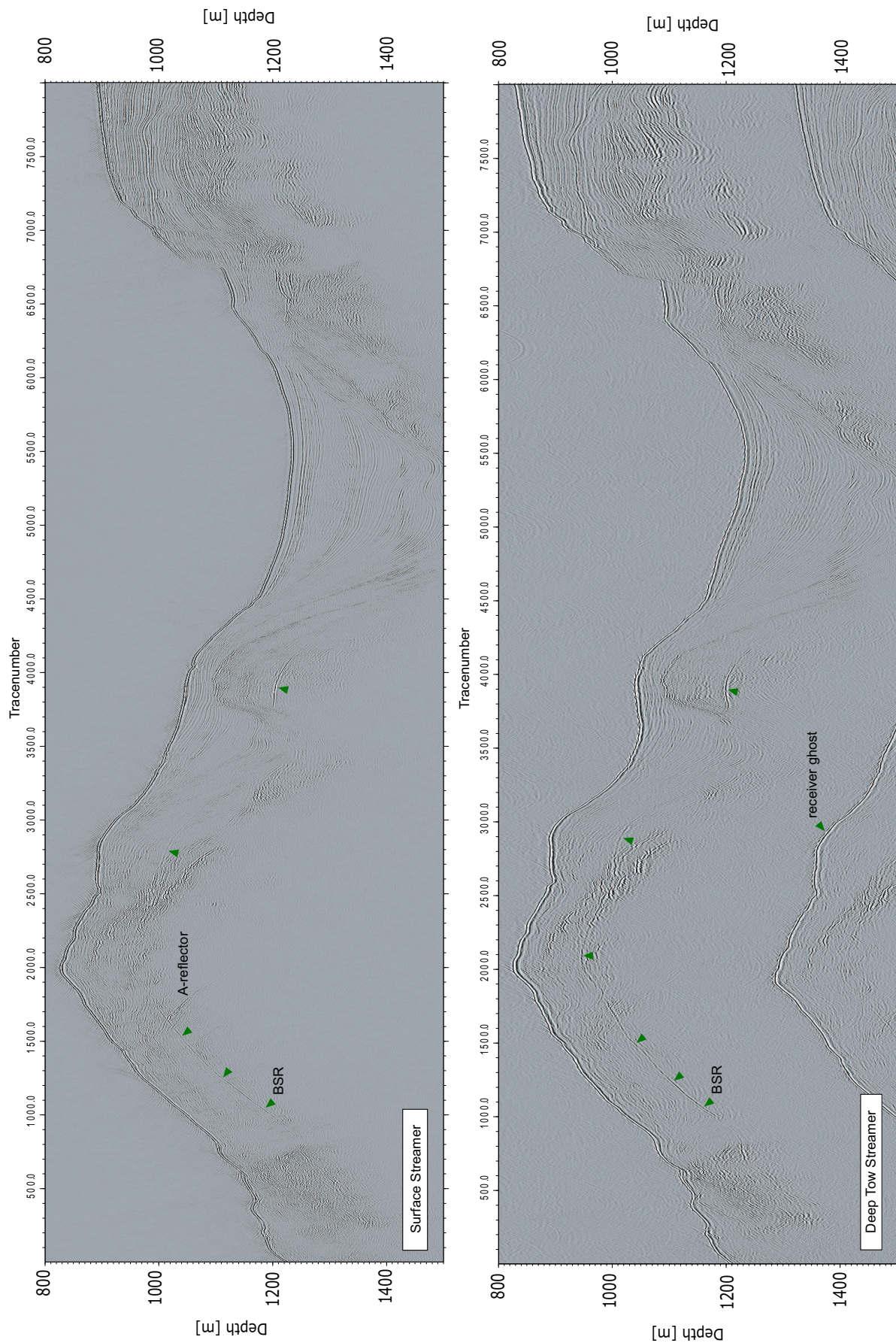


Figure 2.17: Migrated sections showing the surface streamer (top, time-migration with constant velocity of 1550 m/s) and the deep tow streamer data (bottom, depth-migration with a constant velocity of 1480 m/s).

3 Velocity Model

3.1 Introduction

The data of ten OBH and OBS along profile p173 (Fig. 3.1) are used to obtain a detailed 2-D velocity model and to investigate the BSR interface structure across Southern Hydrate Ridge. As part of the ODP leg 204 this data set was extended by deploying seven OBS at the crest of the ridge during Cruise EW0208 (*Bangs and Pecher, 2002*). Both data sets are used to derive a P-wave velocity model by applying the 2-D traveltimes inversion algorithm of *Zelt and Smith (1992)*. The *rayinvr*-software code (*Zelt and Smith, 1992*) is used for this process, iteratively applying two modules:

- **rayinvr**, a forward 2-D ray tracing program to compute refraction and reflection traveltimes
- **dmpltsqr**, a program to apply the method of damped least-squares to the linearized inverse problem, which uses the partial derivatives of the traveltimes residuals calculated by the program **rayinvr**

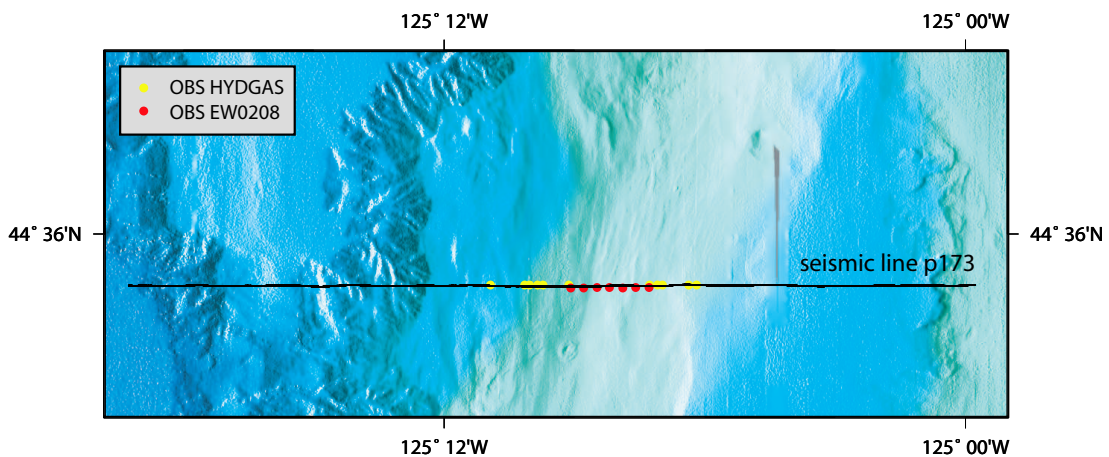


Figure 3.1: Map showing the bathymetry of Hydrate Ridge and deployed ocean bottom instruments along p173, used for the velocity analysis. Data from instruments of the HYDGAS cruise (yellow) and Ewing cruise (red) were used.

Before running the inversion process, some efforts are made to set up an accurate starting model and to minimize uncertainties in the final velocity model. The seafloor and BSR reflections in the OBH/OBS are picked in all sections as well as in the deep tow streamer and the surface streamer sections. However, combining all three seismic receiver configurations is instable for the inversion method. Due to the uncertainty of the deep tow geometry, only the OBH/OBS and the surface streamer data are included in the inversion process.

3.2 Pre-modeling considerations

3.2.1 Arrival picking and classifying

"A model developed by the analysis of wide-angle traveltime data is as good as the picks" (*Zelt, 1999*). Arrivals should only be included in the modeling once they can be confidently identified. In general, the data analyzed here have a good signal to noise ratio, allowing a good identification of reflection arrivals. However, pre-processing steps and geometry considerations reduce picking accuracy to five or 10 ms, depending on the receiver type. Only seafloor and BSR arrivals are used for the inversion algorithm. The BSR near-offset reflections are weaker than the far-offset reflections, inhibiting picks at near offsets at some stations, especially locations where prominent reflections cross-cut the BSR. Overall, only picks of confidently identified BSR phases are included into the inversion. Data, where picks cannot confidently be identified are only included qualitatively and do not run through the inversion process.

3.2.2 Data uncertainties

The picking accuracy was reduced by pre-processing steps and geometry considerations. As a consequence of the lateral drifts of more than 100 m of the OBS after deployment, profile shots were offline. The station depths of all OBH/OBS deployed along p173 are between 800 and 1000 meters, resulting in an average traveltime deviation of ~ 4 ms when passing the OBH/OBS (Fig. 3.2). An average value of 1 ms was applied to the raw data during the swell-filter process. Thus, the picking uncertainty of the OBH/OBS data is assumed to be 5 ms due to offline shooting (4 ms) and swell-filtering (1 ms). Similar considerations result in a mean picking uncertainty of 8 ms for the surface streamer data. The position of the deep tow streamer was determined by the direct arrivals and seafloor reflections. Large uncertainties in locating the streamer position cannot be ruled out, due to turbulent movements of the streamer, which was towed at the end of a 1000 m long cable, not knowing the exact water depth of the receiver. Consequently the picking accuracy of the deep tow streamer data is defined to 10 ms.

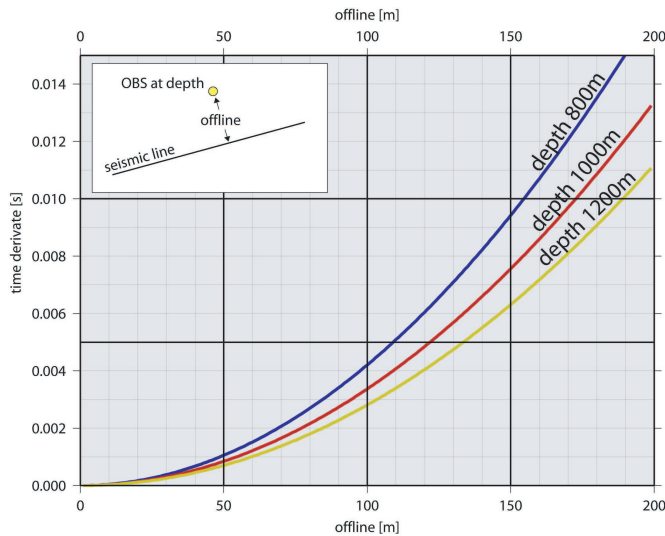


Figure 3.2: *The influence of traveltime uncertainties at ocean bottom instruments drifting offline from the shot profile. Traveltime residuals to on-line shooting are displayed in relation to offline distance and deployed station depth.*

3.2.3 Data Fitting

A common method to describe the quality of the inversion result is the chi-square (χ^2) test. In short, chi-square is defined as the sum of each weighted (squared) difference:

$$\chi^2 = \frac{1}{n} \sum_{i=1}^n \left(\frac{t_{pick} - t_{calc}}{\varepsilon} \right)^2$$

where,

- n = number of picked traveltimes,
- t_{pick} = picked traveltime,
- t_{calc} = calculated traveltime,
- ε = picking uncertainty.

Ideally, an overall normalized traveltime misfit of $\chi^2 = 1$ should be achieved ([Bevington, 1969](#)). Data fitting is strongly linked to the data uncertainties. In addition, the choice of velocity and depth node spacing influences the inversion result. The rayinvr-code has to be modified to take into account for a denser spacing of lateral model nodes. The original spacing is limited to 10 m, definitely enough for the analysis of crustal velocity structures, where profiles can reach more than 200 km. Here, along profile p173, all OBH/OBS data cover a line of 10 km and the GI-gun shot distance is 15 m (sparker-lines 7 m). Advised strategies by C. Zelt ([Zelt, 1999](#)) for modeling seismic refraction and wide-angle reflection traveltimes suggest a node spacing equal to at least the shot point distance. To handle a higher lateral resolution, the accuracy for node spacing is modified in the source code and increased to 1 m. However, higher lateral resolution provides more room for inverting a good fit "numerically" but may

be useless in geological terms. Therefore different node spacings are tested to obtain a stable inversion run and to gain suitable results for geological interpretations. It turns out that a node spacing within the range of the Fresnel-zone is sufficient for the traveltimes inversion. Additionally, by combining two independent data sets (OBH/OBS and SCS data), emphasis is placed on simultaneously inverting traveltimes picks from both configurations. Especially the ray coverage is increased by combining these two configurations, and model parameters are better constrained.

3.3 Modeling

3.3.1 Starting Model

The bathymetry along profile p173 is included in the starting model, defining the water column as a fixed layer with a constant seismic water velocity of 1480 m/s. The water P-wave velocity is derived by the moveout-traveltimes of the direct arrivals of the OBH/OBS recordings. A second layer is introduced with a bottom boundary marking the BSR. This layer, representing the gas hydrate stability zone (GHSZ), parallels the seafloor at a constant vertical distance of 150 m. The velocities are set to 1520 m/s at the top of this layer (seafloor) and 1600 m/s at the bottom (BSR) (Fig. 3.3).

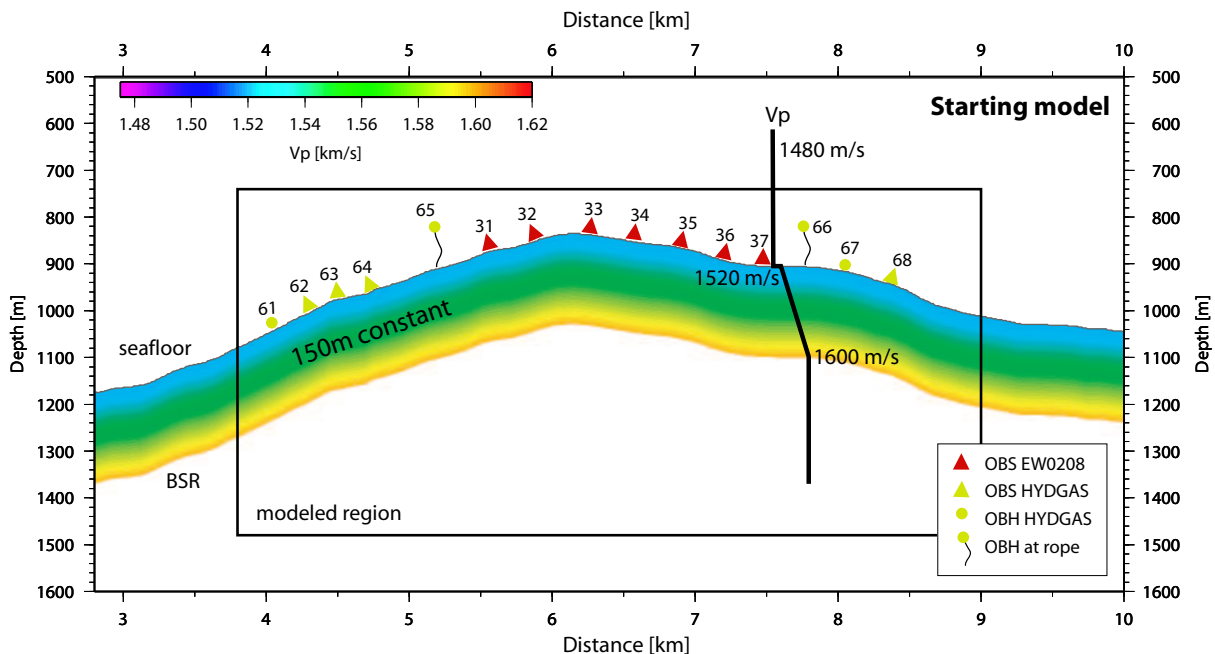


Figure 3.3: Starting model for the traveltimes inversion. The BSR is at a constant depth, 150 m below the seafloor. P-wave velocity is fixed in the water column with 1480 m/s; sedimentary layer down to the BSR starts with 1520 m/s at the seafloor and gradually increases to 1600 m/s at the BSR.

3.3.2 Inversion

During the inversion process, velocity and depth nodes are fixed alternately to understand how these parameters affect the inversion algorithm. Sediment velocities below the seafloor are fixed to 1520 m/s at the beginning, but are also inverted for in the final stage. During the first iterations only the velocities and depth values at the BSR are inverted to approximate the resulting velocity model. In a final run, all traveltimes are inverted (except for the water column) resulting in a final velocity-depth model (Fig. 3.5). The misfit of the calculated and observed (picked) traveltimes (Fig. 3.4) has an overall value of $\chi^2=1.13$. Both, streamer data and OBS data are inverted simultaneously. The inversion results for each individual OBH/OBS are displayed in Table 3.1. OBH 65 was deployed 200 m above the seafloor. The high χ^2 -value of 2.06 for OBH 65 is the result of the ambiguous OBH position during the relocalization process. In general, the simultaneous inversion of different receiver configurations (streamer and

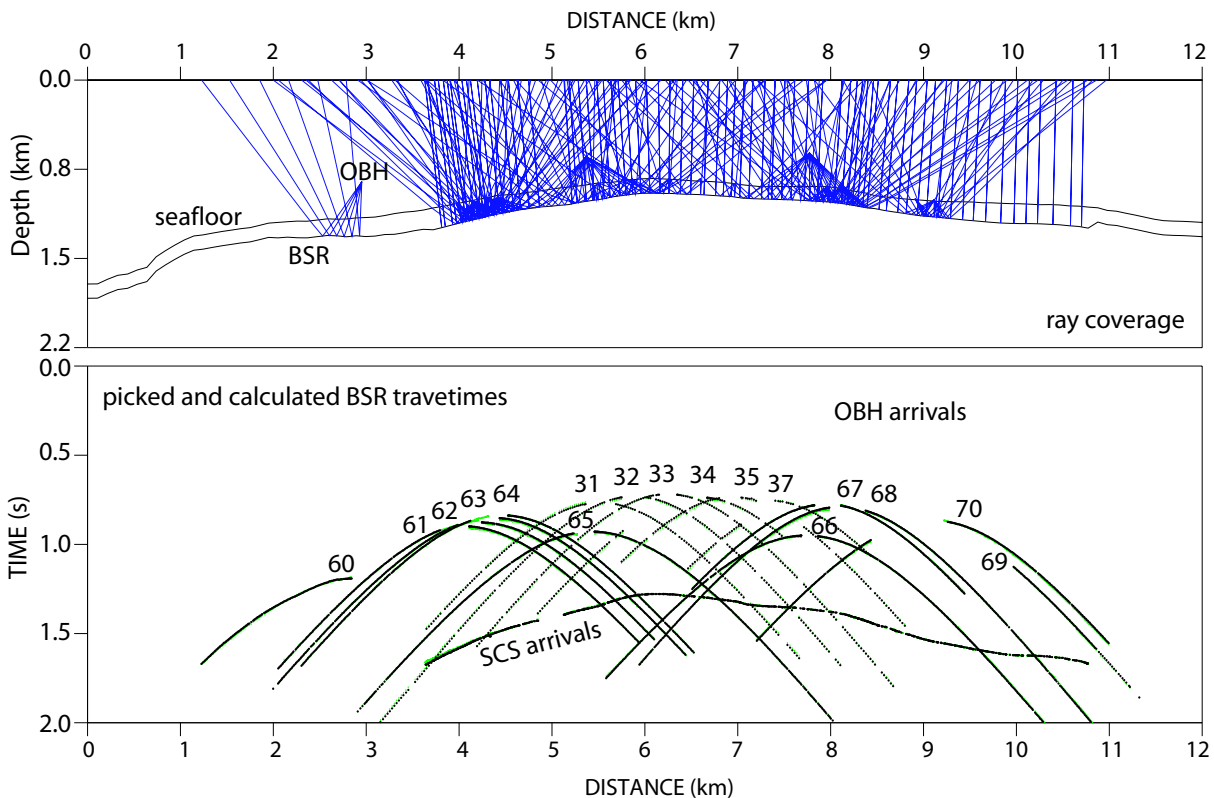


Figure 3.4: *Traveltimes of the picked and calculated arrival (lower panel). Ray-coverage of rays (every 20th ray is plotted) from OBH/S and streamer data. The green bars mark the picking uncertainty of 5 milliseconds during the inversion process. Calculated traveltimes correlate to the picked traveltimes with a χ^2 of 1.13.*

instrument	χ^2	std. deviation
obh 60	0.97	1 ms
obs 61	0.84	1 ms
obs 62	0.98	1 ms
obs 63	0.74	2 ms
obh 64	0.88	1 ms
obh 65	2.06	6 ms
obh 66	0.75	2 ms
obh 67	0.83	2 ms
obs 68	0.53	3 ms
obh 69	1.01	1 ms
obh 70	0.97	1 ms

instrument	χ^2	std. deviation
obs 31	1.03	1 ms
obs 32	0.91	1 ms
obs 33	0.98	1 ms
obs 34	0.88	1 ms
obs 35	1.11	1 ms
obs 36	-	-
obs 37	1.25	3 ms

Table 3.1: χ^2 values and standard deviation of the traveltimes misfit after the inversion process for each station.

OBH/OBS data) leads to a more accurate velocity model, since the sensitivity of the inversion process is raised dramatically when including the surface streamer data.

3.3.3 Model Assessment

Since multiple receiver configurations are used in this inversion algorithm, efforts are made to keep the accuracy as high as possible and to minimize the uncertainty. In this section the inverted final velocity model is tested on uniqueness by applying an error estimation. In a first step the velocity-depth model is converted to a velocity-time model and compared to the seismic section of line p173. The seismic section overlain by the color-coded velocity function, now converted to time, is displayed in Figure 3.5. The bottom of the colored velocity-interval matches the BSR in the seismic section. In a second stage the inversion is run again, with the final model as starting model but the BSR fixed at a depth 10 m deeper with respect to the starting model. The iterative inversion process is checked after each step and the inversion results of each individual station and the streamer data are controlled visually. This is necessary to achieve overall mean and constant traveltimes residuals not exceeding the defined picking accuracy of 5 ms by more than 2 ms. Thus, the total traveltimes derivation is below 7 ms. The traveltimes residuals for the streamer data and each station, displayed in Figure 3.6, show the different quality of the inverted models. The result of the inverted test model (shifted and fixed BSR by 10 m) has higher traveltimes residuals after the inversion compared to those of the preferred final model. However, χ^2 -values of $\chi^2 \sim 1$ are still acceptable for a possible model. The resulting P-wave velocities compared to

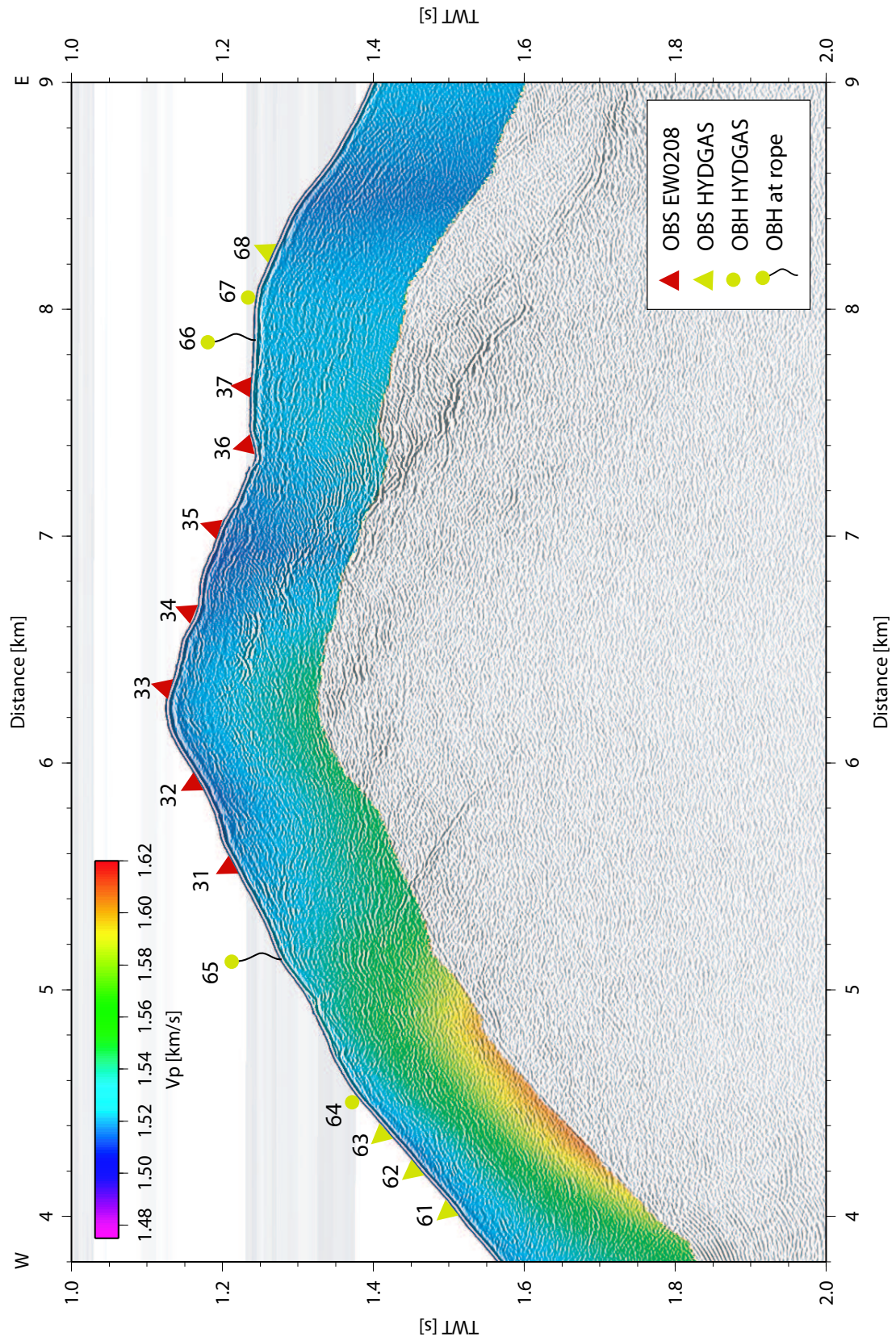


Figure 3.5: Final velocity model underlain by the seismic section of GI-gun line p173.

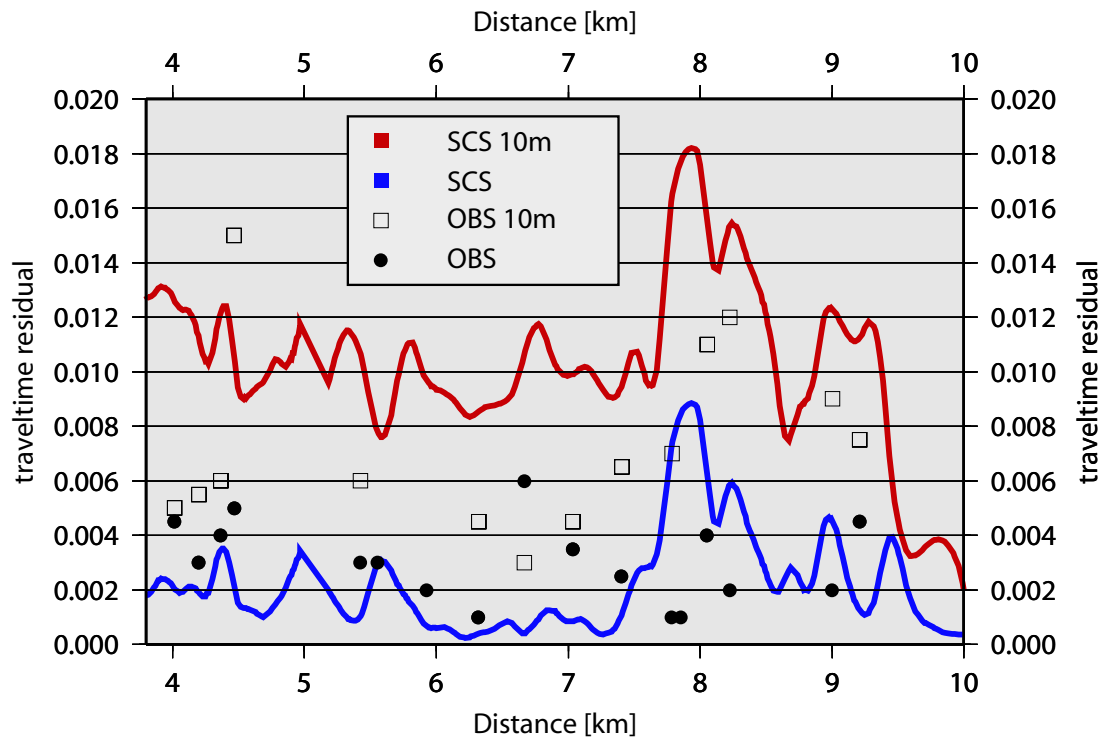


Figure 3.6: *Traveltime residuals of the final model compared to the reference (BSR 10 m deeper) model.*

those of the final model are displayed as residual velocities in Figure 3.8. An average uncertainty of 20 m/s in the velocity model can be observed. Strong lateral changes are restricted to the eastern flank of the ridge where the shifted BSR inverts a different vertical velocity gradient compared to the final model. This is demonstrated by the color-coded V_p -residuals in Fig. 3.8. A nearly constant 20 m/s (green) uncertainty in P-wave velocities along the western flank can be applied to the final model. The eastern flank is dominated by lateral changes suggested by the strong reflectivity changes in the seismic image. In contrast to fixing the BSR 10 m deeper, a second inversion run is tested with fixed velocities at the BSR. This fixed velocity is now increased by 20 m/s compared to the preferred and final model. Consequently the BSR depth is inverted to a different depth. A mean traveltime residual of 2 ms beyond the defined picking accuracy is accepted for the inversion result. The inverted BSR depth is displayed in Figure 3.7. The overall shift of 5 to 7 m, averaged along the entire profile, correlates to the uncertainty results of the previous test, when keeping the BSR fixed 10 m deeper. In conclusion, an average error of ± 20 m/s in the velocity distribution and ± 10 m in the depth estimation has to be considered in the final velocity-depth model.

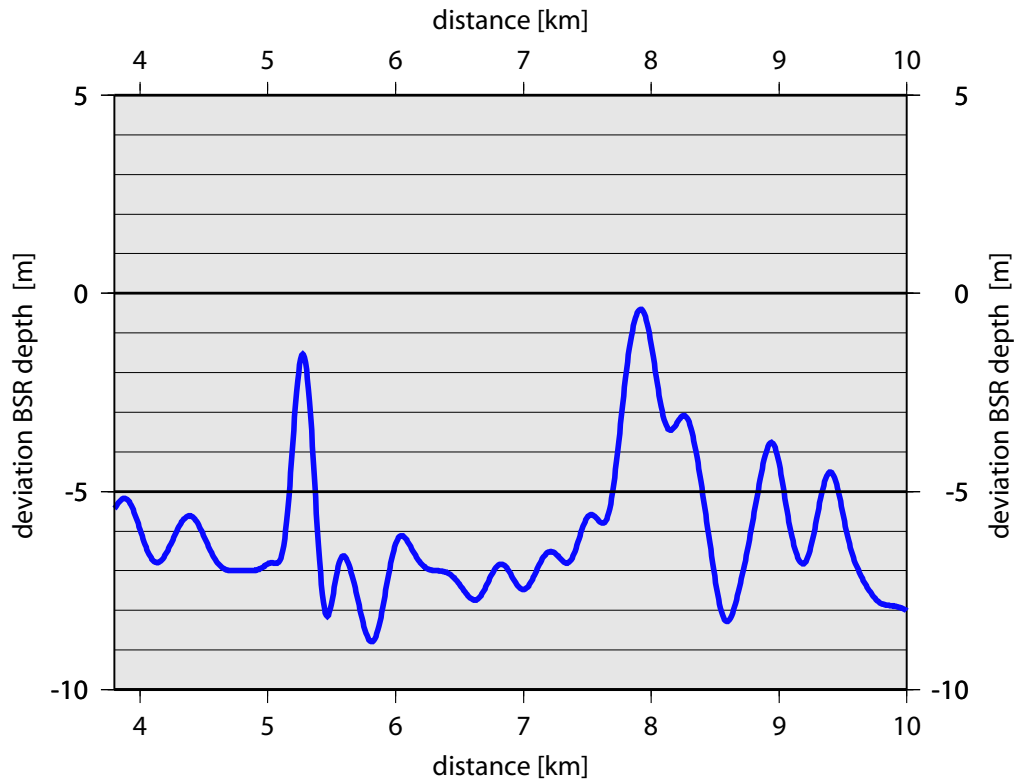


Figure 3.7: *Deviation of the BSR depth to the inverted original depth with a higher reference velocity at the BSR (+ 20 m/s).*

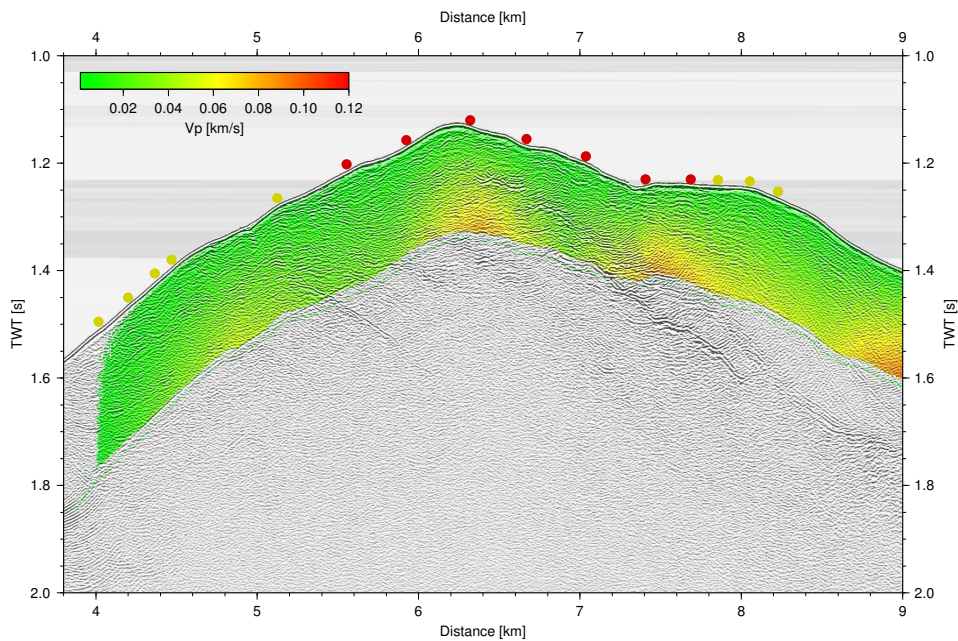


Figure 3.8: *Averaged velocity error (color-coded). Velocity residuals, resulting from an inversion with a BSR 10 m deeper.*

In addition to the OBS and the SCS data, reflection arrivals in the seismic deep-tow-section along line p173 are picked. The positioning of the deep-tow streamer is inaccurate to directly contribute to the inversion process. Nevertheless, the final model is tested for the picked arrivals of the deep-tow system. Results of forward raytracing of the BSR traveltimes compared to traveltimes picks of the deep-tow data are displayed in Fig. 3.9.

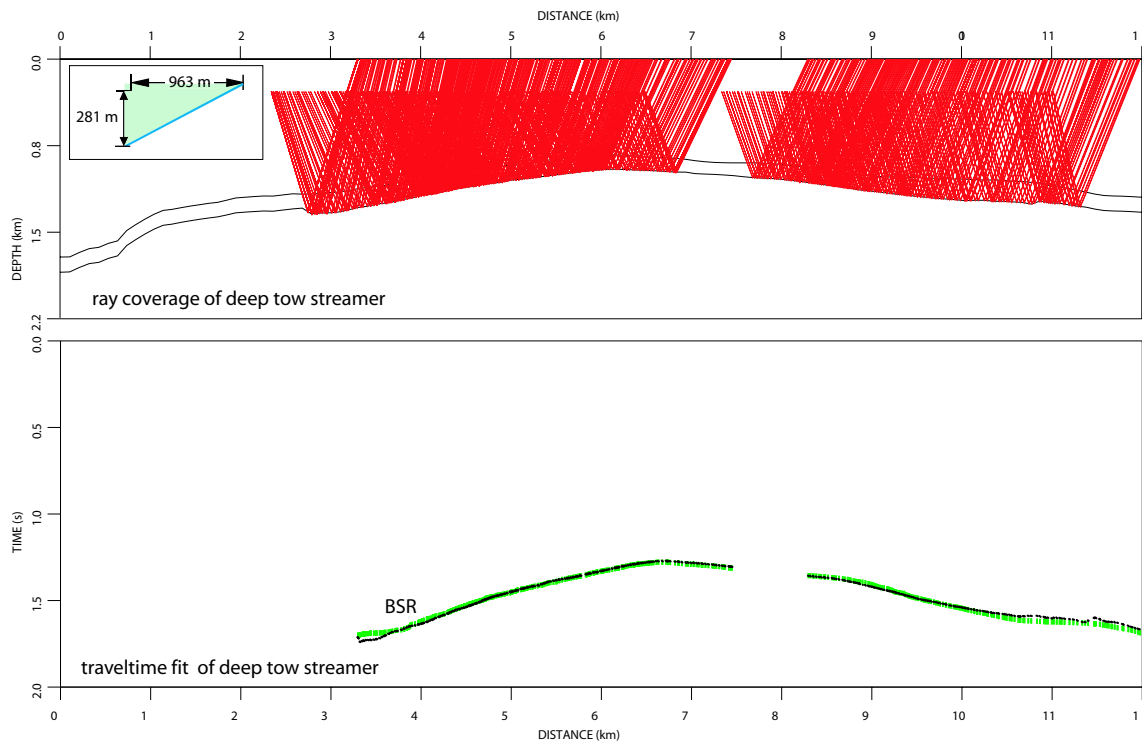


Figure 3.9: *Ray tracing result of the final model for the deep-tow geometry. The picked BSR of the deep-tow data fit the calculated traveltimes of the final model (lower panel).*

The calculated BSR traveltimes for the deep-tow streamer geometry (Fig. 3.9) fit the picked deep-tow BSR arrivals. The good correlation of the independently modeled deep-tow data is an additional constraint for the final result of the inversion algorithm.

3.3.4 Final Model

The inversion result is displayed in Figure 3.10. The inverted velocity model shows three distinct zones of velocity anomalies. The average velocities between the seafloor and the BSR are typical sediment velocities, even smaller than P-wave velocities suggested by *Hamilton (1979a)*. The apparent high velocities at the western flank of the ridge might indicate the presence of gas hydrates. It is believed that the occurrence of gas hydrates increase the compressional wave velocity (*Guerin et al., 1999*). Two zones of low P-wave velocities mark the eastern flank of the ridge, possibly caused by upward migrating fluids. A comparison of the starting model and the final model (Fig. 3.11) reveals some features, which can also be observed in the flattened seismic SCS-sections (Fig. 3.12). Figure 3.11 shows a sketch comparing the starting and the final model. The starting depth of the BSR is moved upward, varying in depth between 100 and 130 m below the seafloor (mbsf), compared to a starting depth of 150 mbsf. Only at the western flank of the ridge the BSR depth stays at 150 mbsf and reaches greater depths further west. The seismic sections displayed in Figure 3.12 are flattened, which means statically shifted for a constant seafloor. This illustration allows a better comparison of the BSR progression relative to the seafloor. The seismic sections displayed are time-migrated before the static shifts are applied. The data are not depth migrated,

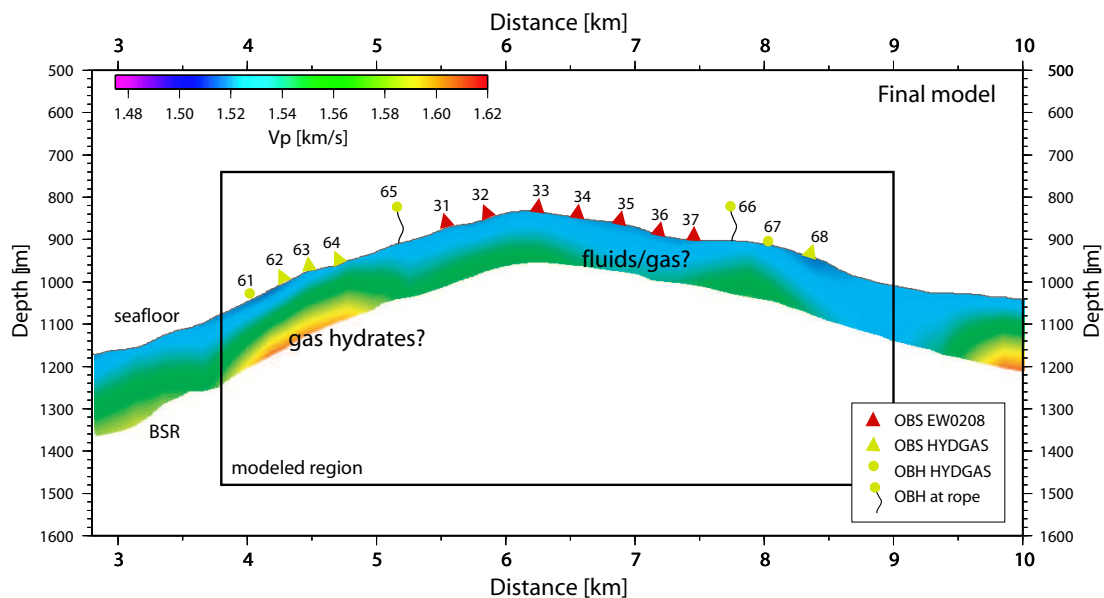


Figure 3.10: *Final velocity model inverted from OBS wide-angle reflection data. Velocities are typical sediment velocities and no hydrate related velocity increase can be observed, except on the western flank, where locally higher velocities might indicate the presence of gas hydrates.*

but give us a first insight on how the BSR changes its characteristics along the profile. The BSR is shallower beneath the crest of the ridge. This behavior is constrained by the inverted results.

The final velocities, compared to the starting values, are inverted for lower P-wave velocities (< 1600 m/s), except in the region of the western flank. In general, P-wave velocities are below 1600 m/s at the BSR, but P-wave velocity gradients vary along the profile (Fig. 3.11) and suggest lateral changes of the sedimentary units.

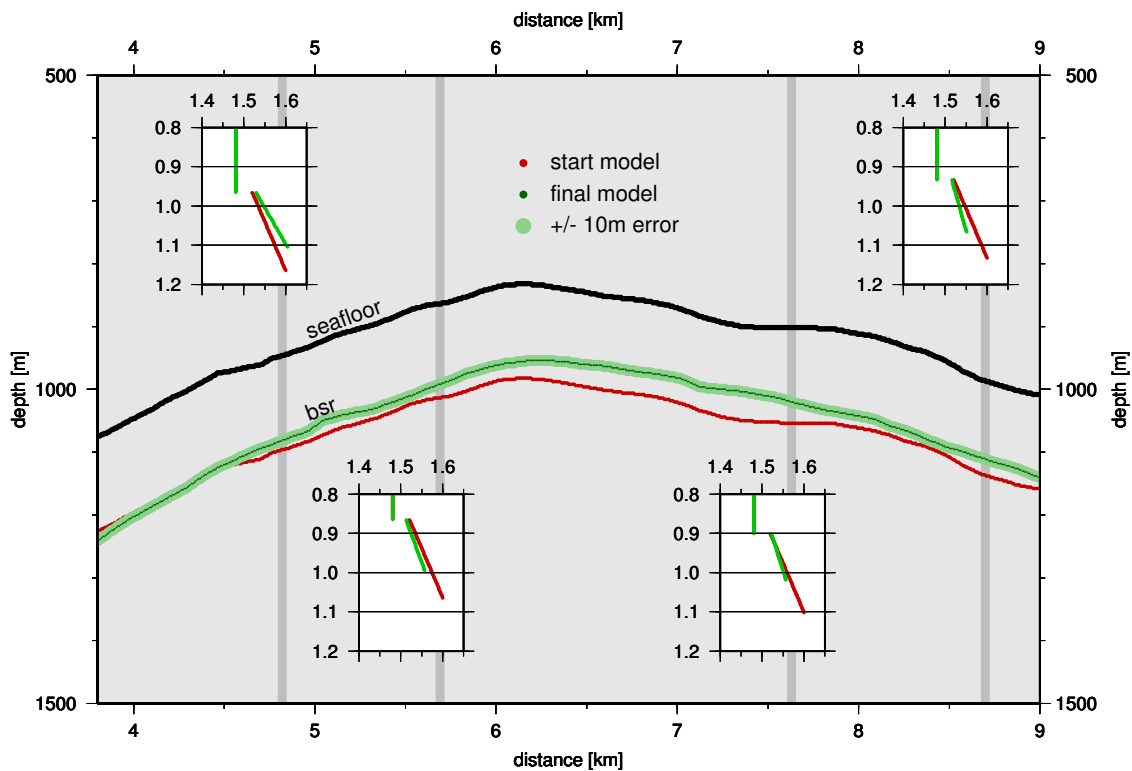


Figure 3.11: Comparison of the starting model and the final inverted velocity model.

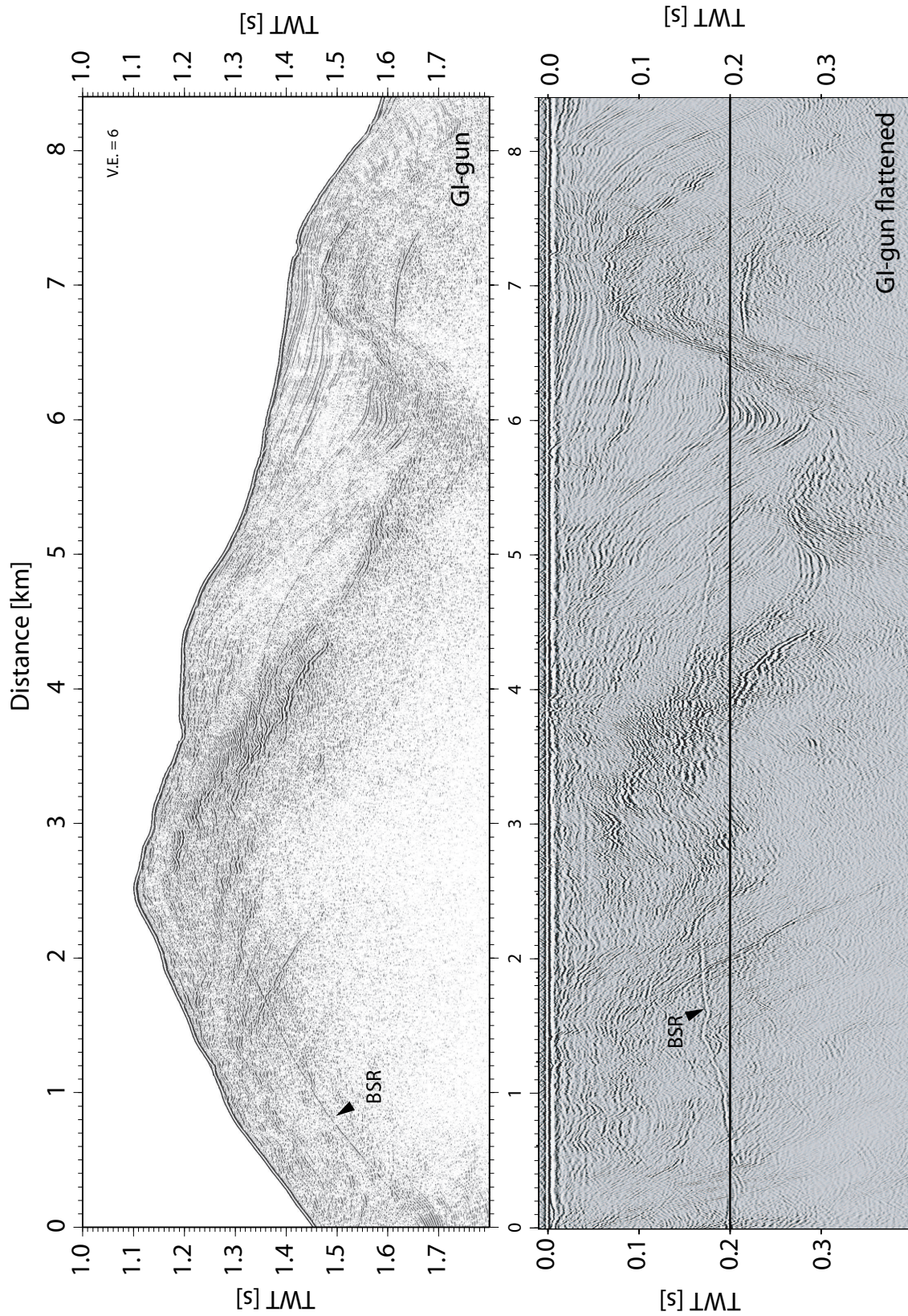


Figure 3.12: *Seismic time-migrated section of the SCS GI-gun data (upper panel). The data displayed in the lower panel is the same section as above, but statically shifted to a constant seafloor arrival to better resolve the varying depth of the BSR.*

3.4 Model discussion

The most surprising result of the traveltimes inversion is the relatively low seismic P-wave velocity in the GHSZ. The BSR is commonly assumed to mark an interface between high-velocity gas hydrate and underlying sediments of normal velocity (*Stoll and Bryan, 1979; Hyndman and Spence, 1992*) or sediments of low velocity containing free gas (*Dillon and Paull, 1983; Miller et al., 1991*). Whereas compressional velocity values of 1700-2400 m/s are known to be typical for gas-hydrated sediments (*Andreassen et al., 1990; Katzman et al., 1994; Lee et al., 1994; Minshull et al., 1994; Andreassen et al., 1995*), values below the sound velocity of sea water indicate free gas in the pore space. Existing seismic velocity analyses (*Hyndman and Spence, 1992; Singh et al., 1993; Katzman et al., 1994; Ecker and Lumley, 1994*) relate gas hydrate saturations of 1% to seismic P-wave velocities of 1700 m/s and above.

The inversion results suggest even lower concentrations of gas hydrates within the GHSZ. Only the occurrence of the prominent BSR indicates the presence of gas hydrates. Drill Site information of ODP Leg 204 (*Tréhu et al., 2003*) constrain the inversion result and the presence of mean low gas hydrate concentrations. Results of ODP 204 will be discussed in detail further below in Chapter 6. The inverted velocity model of line p173 is coincident with an existing multichannel seismic (MCS) reflection profile (*MacKay et al., 1992; MacKay, 1995*). The data of MCS line OR02 (*MacKay et al., 1992; MacKay, 1995*) is now processed with the velocity information obtained from the inversion result and a pre-stack depth focusing analysis is carried out. P-wave velocity gradients, derived from the traveltimes inversion, are only defined in the upper layer between the seafloor and the BSR. In order to include the velocity model into the MCS analysis, P-wave velocity gradients are linearly extrapolated to depths of 2500 m to image deeper arrivals, recorded in the MCS data. The two objectives of this analysis are (1) to test the inverted velocity model in the GHSZ and (2) to associate the velocity gradients with deeper geologic structures, which are imaged with the deeper penetrating MSC data. The depth-migrated MCS section overlain by the extrapolated velocity image is displayed in Figure 3.13. The algorithm used during the prestack depth-migration is based on the Kirchhoff integral solution, using the software package *SIRIUS*. The migration module computes traveltimes maps by using a maximum energy ray-tracing algorithm and generates, besides the stacked depth section, conventional focusing analysis files. The focusing analysis is a measure of how accurate the migration algorithm worked. Incorrect velocities will under- or overmigrate reflection arrivals and consequently lead to weaker focusing energy. During the migration process this focusing analysis is used to iteratively build an accurate velocity model.

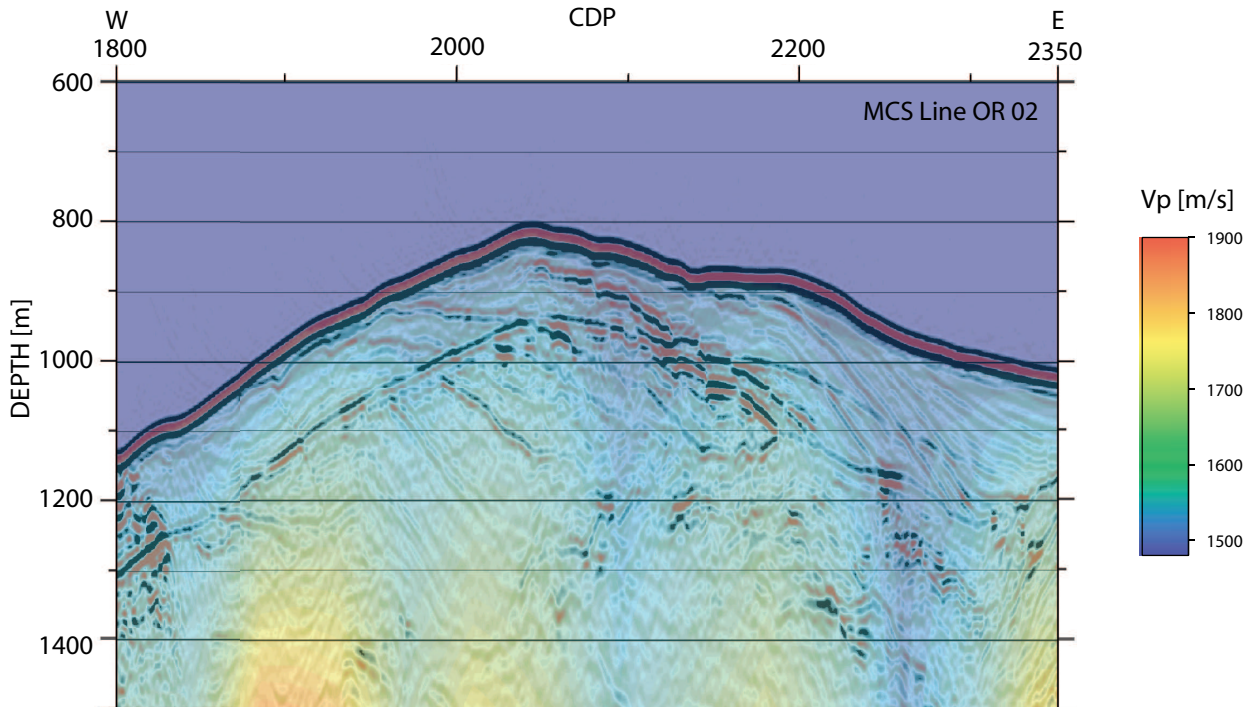


Figure 3.13: *Depth migrated MCS Line OR02 overlain with the velocity model, obtained by wide-angle reflection data. The inverted velocity model is extrapolated with a constant velocity gradient to deeper depths to match the deep penetrating MSC data.*

In general, the results of the focusing analysis confirm the velocities, obtained by the wide-angle OBS data, within the upper sedimentary layer. Although, two distinct features are presented here for further investigation. Locally high velocities on the western flank might indicate the presence of gas hydrate (compare with Figs. 3.5 and 3.15). Another explanation is the increase of velocities, due to a change in lithology. Here, the velocity anomaly is likely caused by a different sedimentary unit of higher velocities cross-cutting the BSR, and not by increasing velocities associated with the presence of gas hydrates above. The second focus is set on the presence of free gas below the BSR, indicative by low P-wave velocities. The depth-focusing analysis (Fig. 3.14) result in higher velocities below the BSR (upper panel, Fig. 3.14) between CMP 1941 and 1961, the area of the local high velocity anomaly, observed in the travelt ime inverted model (Fig. 3.5).

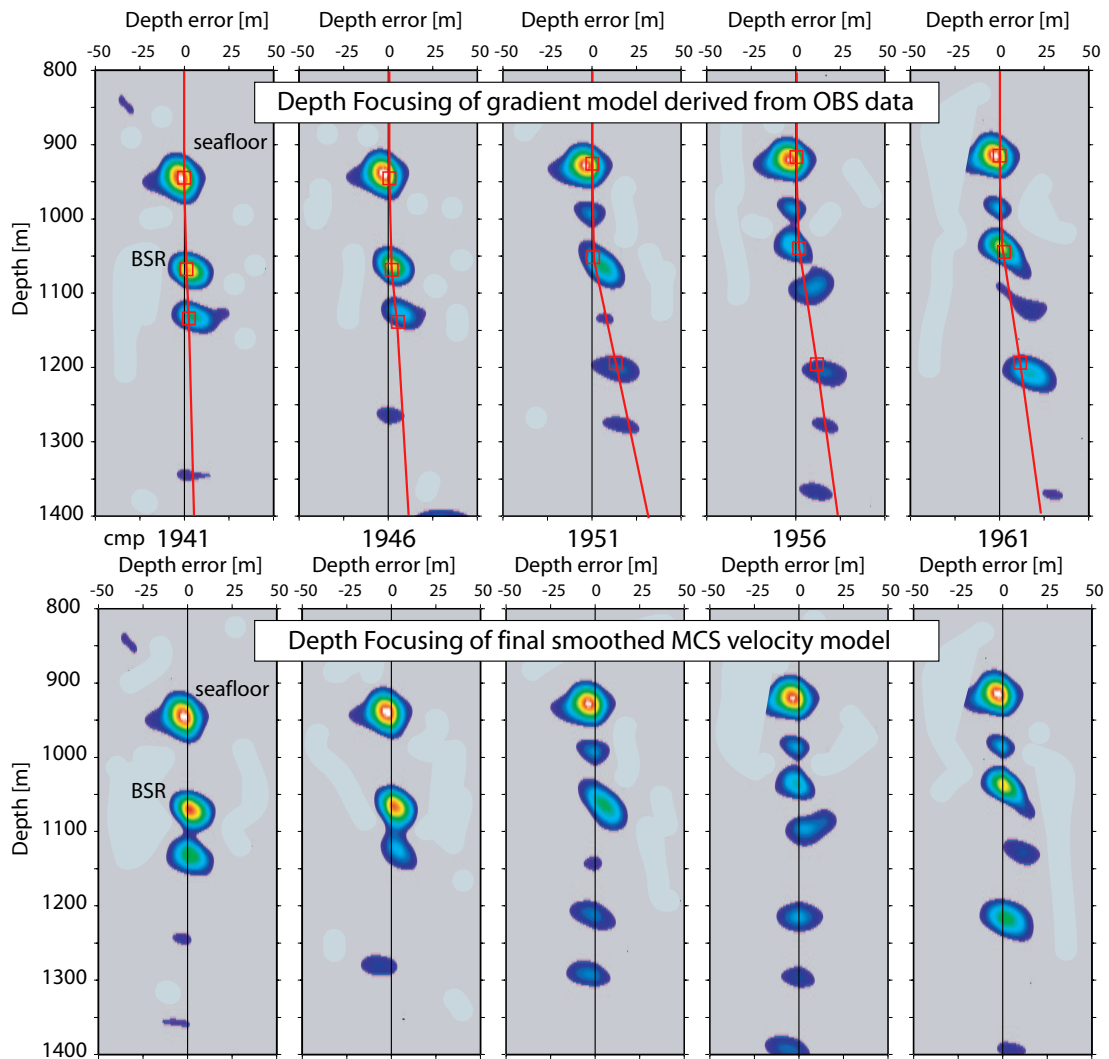


Figure 3.14: *Focal analysis of the migration process of the MCS data. CMP locations of locally high velocities in the final inverted velocity model are displayed.*

Ideally, focusing clusters (focs) should be in a vertical line at a 0 depth error (horizontal scale). The horizontal scale specifies the error of "unfocused" migration results and predicts the depth of an accurate (well focused) velocity. In the upper panel of Figure 3.14, a trend to higher velocities is clearly indicated by the positive depth error (focs move to the right) below the BSR. Seafloor and BSR focs are in vertical line, accurately imaged, indicative for correct velocities above the BSR. In the iterative approach of the migration process, velocities are corrected to satisfy the focus analysis. The focal images of CMP 1941 to 1961 of the final migration result are displayed in the lower panel of Figure 3.14. The entire velocity model and the pre-stack depth migrated section after the final iteration is displayed in Figure 3.15.

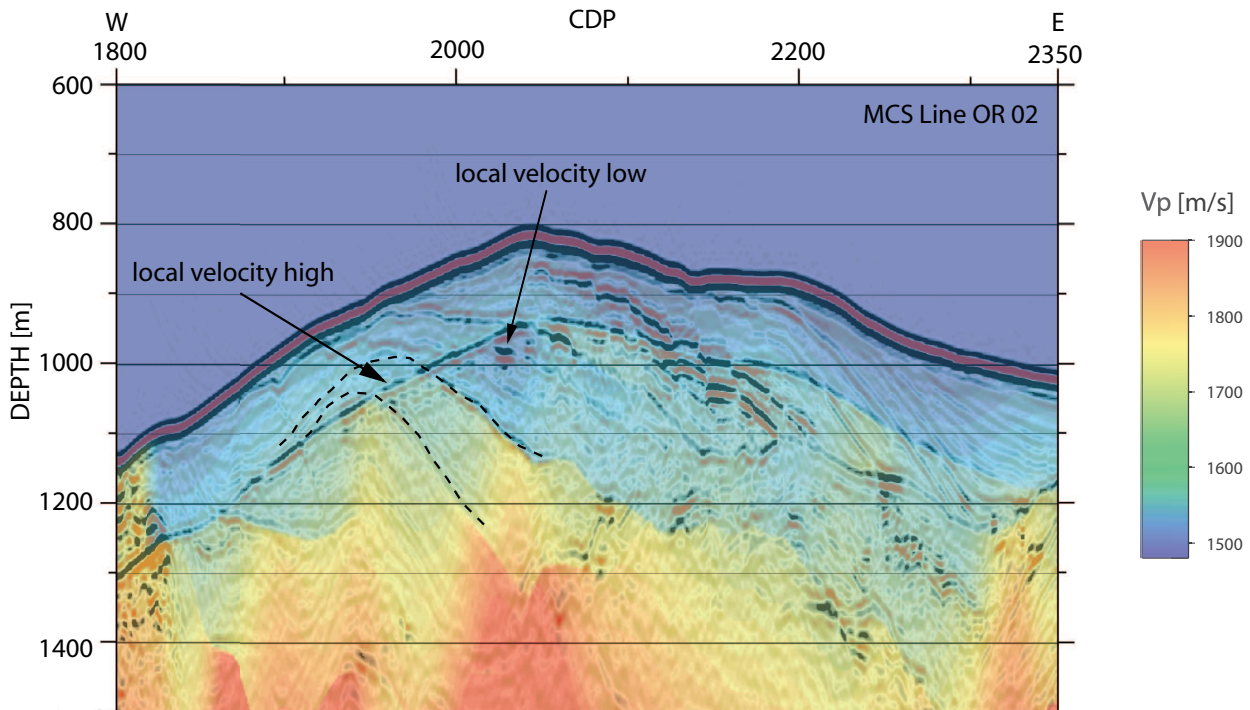


Figure 3.15: *Depth migrated MCS Line OR02 overlain with the velocity model, derived from the final iteration of the migration process.*

Returning to the origin of the local velocity high (Fig. 3.15), both explanations mentioned above are analyzed using the information of the migration/focusing results. In the case of hydrate bearing sediments, causing the increase of P-wave velocities, one would expect a decrease in velocity to the 'background' sediment velocity trend (without gas hydrate) below the BSR. In the other case, where velocities are caused by a different sedimentary unit cross-cutting the BSR, the same velocities should be present beneath the BSR. The results of the focusing analysis suggest an increase in P-wave velocities below the BSR with an even stronger velocity gradient as assumed before by the traveltimes inverted velocities. Consequently, it is likely that the velocity anomaly is caused by the change in lithology and not by the presence of higher concentrations of gas hydrates. Figure 3.15 reveals a strong link to a faulted sediment package of higher velocities cross-cutting the BSR in this area, which probably causes the anomaly, observed in the inverted velocity model. Again, results of ODP leg 204, discussed in Chapter 6 constrain this observation.

The second important aspect analyzed in the migration process, is the presence of free

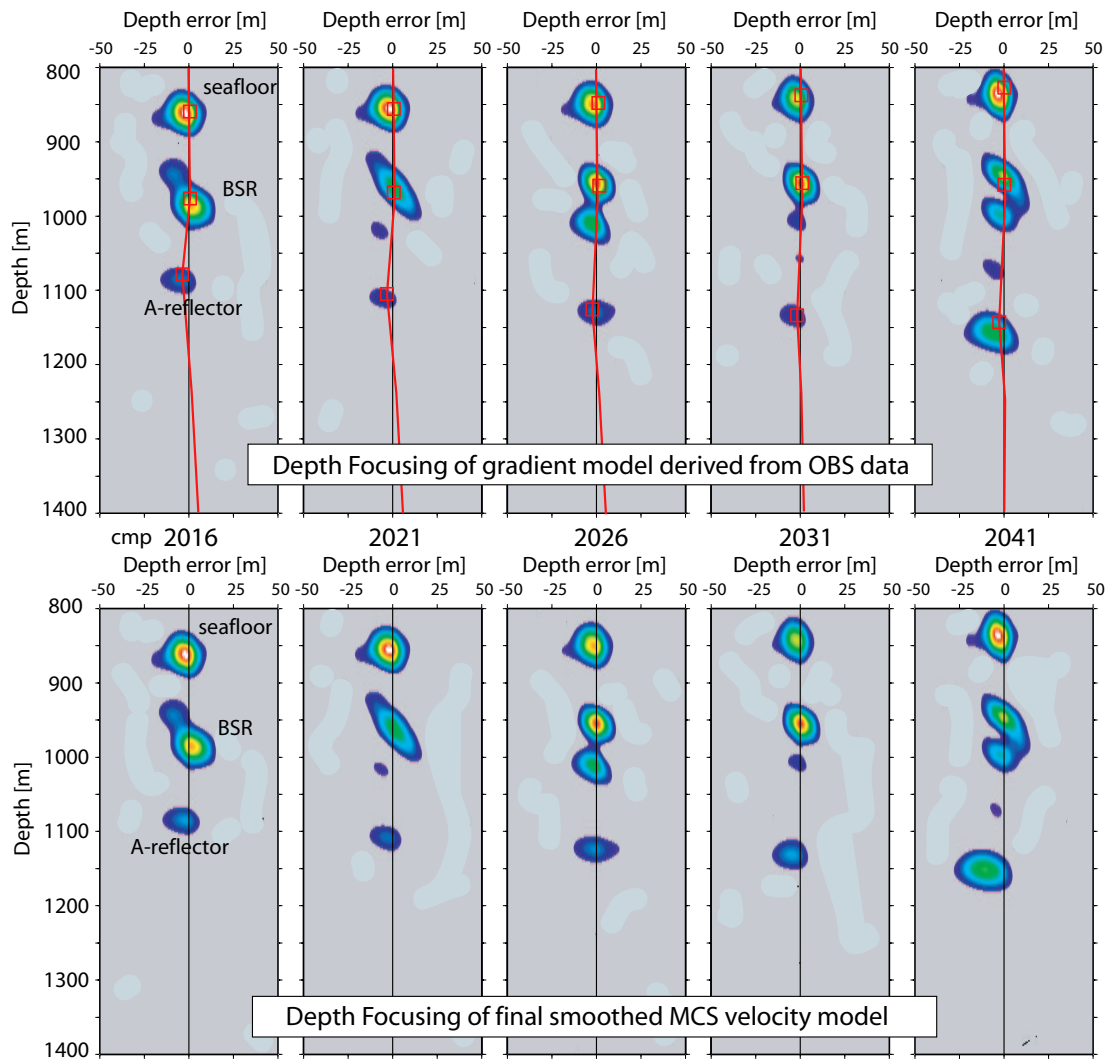


Figure 3.16: Focal analysis from the migration process of the MCS data. Displayed are CMP locations where the decrease in the P-wave velocity is observed.

gas beneath the BSR. A drastic decrease in P-wave velocities is linked to the occurrence of free gas (*Andreassen et al., 2003*). In contrast, the focusing analysis suggests a continuous and linearly increasing P-wave velocity with increasing depths, except for the area between CMP 2016 and CMP 2041 (Fig. 3.16). The strong reflection beneath the BSR in this area, dipping eastwards, the so-called A-reflector, is easily identified during the focusing analysis. Resulting focusing clusters of this reflection suggest slightly lower velocities between the BSR and the A-reflector. The maximum applicable change in P-wave velocity is from 1580 m/s to 1520 m/s at the BSR interface to obtain an accurate migrated depth image. The calculated depth error with a continuous veloc-

ity gradient is relatively small (~ 5 m), compared to the wavelength λ of the seismic signal, which is approximately 30 m. Traveltime inversion of OBS 31, located above the A-reflector, is used to constrain the possible decrease of the P-wave velocity in this region. The geometry of the dipping reflector is obtained from the depth migrated seismic section and introduced to the inversion model as a so-called floating reflector. A floating reflector does not influence the model parameters and no specific velocities are assigned to this reflector. Consequently it is not treated as a layer or an interface. Two velocity models are tested during the inversion (Fig. 3.17).

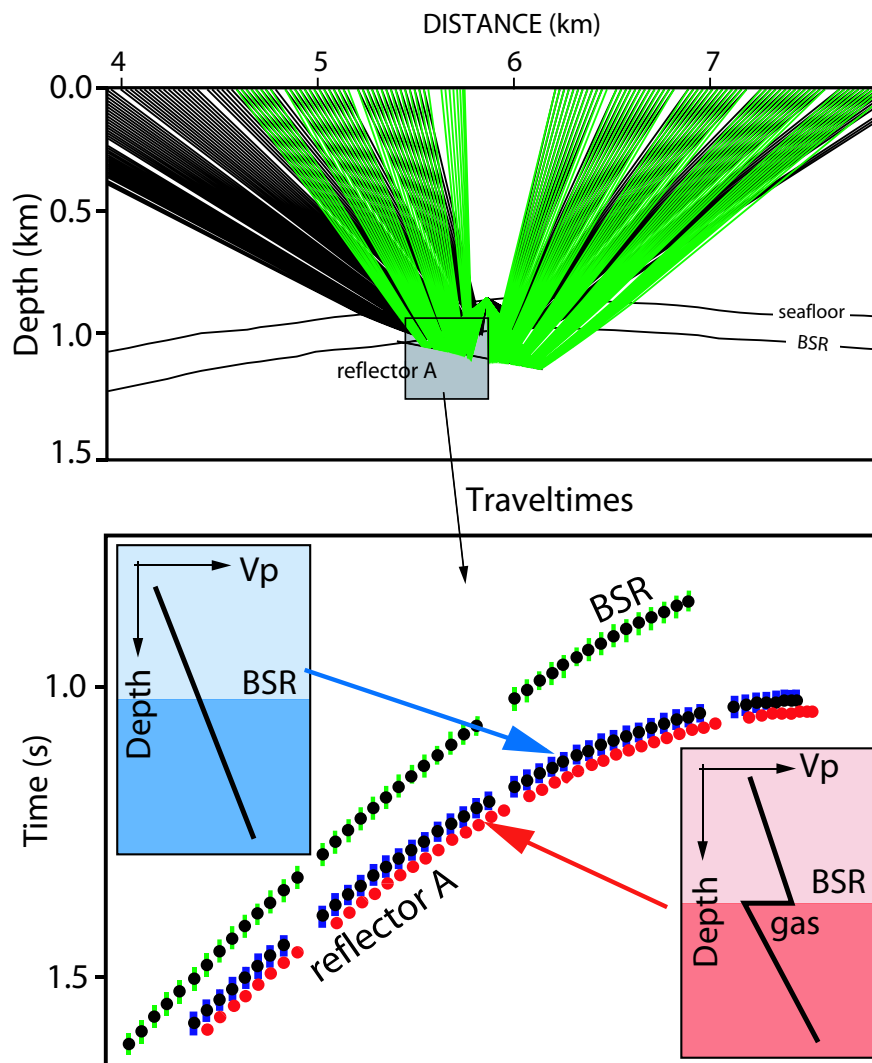


Figure 3.17: Result of the forward ray-tracing. The upper panel shows the ray coverage of the traced rays of the BSR and the floating A-reflector. The lower panel displays the picked and calculated traveltimes of a continuous gradient (blue) and a change to lower velocities (red) below the BSR.

The original constant velocity gradient produces a good traveltime fit in respect of the A-reflector. The inversion even suggests a slight increase in P-wave velocity below the BSR. A velocity decrease from 1580 m/s to 1520 m/s at the BSR, as suggested by the depth-focusing analysis, does not fit the picked arrivals of the A-reflector. The travel-times are very sensitive to the dip of the reflector and consequently the occurrence of a small velocity decrease cannot be ruled out. However, unlike the focal analysis of the MCS data, the tendency of various inversion runs yields a constant velocity gradient or even a possible increase of the P-wave velocity.

3.5 Summary

There is no direct evidence for a layer of decreased P-wave velocities caused by the presence of free gas. In contrast to this result, the existence of the BSR itself does predict at least small amounts of gas below the GHSZ. However, the velocity analysis predicts the thickness of this layer to be relatively small. The analysis of the P-wave velocity model suggest only small amounts of gas hydrates in the sedimentary layer above the BSR and leads to the conclusion that the BSR is mainly caused by free gas in a thin layer below the GHSZ.

4 Amplitude Analysis

4.1 Introduction

In the recent years, various theoretical, semi-empirical, and ad hoc models have been proposed to relate the gas hydrate saturation to seismic velocities. *Wood et al. (1994)*, *Yuan et al. (1996)*, and *Korenaga et al. (1997)* use *Wyllie et al. (1958)*'s time average equation to estimate the gas hydrate saturation after the velocity structure is obtained from seismic data. *Lee et al. (1994, 1996)* use a weighted equation, and *Ecker et al. (1998, 2000)* use a theoretical rock model to estimate the gas hydrate saturation. It is poorly understood how gas hydrates modify the acoustic and elastic properties of hydrated sediments (*Andreassen et al., 1995*), and the predictions obtained by different models vary widely even within one area. For example estimates of the gas hydrate saturation in the Blake Ridge area, offshore South Carolina, range from 50% of pore space by using the time average equation (*Wood et al., 1994; Yuan et al., 1996*) to 10-15% of pore space by using the weighted equation (*Lee et al., 1993*). In contrast, investigations of ODP Leg 164 at Blake Ridge result in an average methane hydrate saturation of 5 to 7 percent of porosity (*Paull et al., 1996*). From the results of the derived velocity model it is likely that the saturation of gas hydrates, at least along the inverted line p173, is restricted to only a few percent. A comparison of the inverted velocities to the velocities used in other velocity studies suggests a saturation of below one percent or even the absence of gas hydrates. Detailed studies have been carried out by *Carcione and Tinivella (2000)* to relate gas hydrate saturations to amplitude reflection coefficients by applying a Biot-type three-phase theory based amplitude versus offset (AVO) analysis. One of the results from *Carcione and Tinivella (2000)* is that for a given gas saturation below the BSR, it is difficult to evaluate the amount of gas hydrate at low concentrations. An important role on estimating the gas hydrate content within the sediments is the knowledge of the shear-wave velocity. Marine shear-wave reflection methods using the OBS acquisition system rely on the mode conversion either at the water bottom or at a subbottom reflector. The mode conversion is described in the equations given by *Zoeppritz (1919)*. Although mode-converted shear-waves are observed in the OBS data at Southern Hydrate Ridge, shear-wave amplitude analysis has found to be more promising at the Northern Hydrate Ridge, since the gas hydrate concentration is believed to be higher at Northern Hydrate Ridge (*Kastner et al., 1995; MacKay et al., 1995; Spence et al., 1995; Wood et al., 2000*). The amount of gas hy-

drate concentration has been estimated to about 5-10% in the GHSZ (*Westbrook et al., 1994*). Amplitude analysis on mode-converted shear-waves at the northern ridge was carried out by *Petersen (2004)*. In this study the amplitude considerations are focused only on P-wave investigations.

4.2 AVO considerations

The conventional approach to derive the physical parameters V_p , V_s , and density at a reflecting interface is the AVO analysis, based on the Zoeppritz equations. Various studies have been carried out in the past, applying this standard AVO technique to quantify the physical parameters at sedimentary interfaces. In this study the focus is set on the restrictions, that have to be made when applying standard AVO analysis on OBH/OBS data. The restrictions that have to be considered are mainly influenced by the following aspects:

- **Amplitude correction factors**

AVO analysis takes advantage of reflection amplitude variations with increasing incident angles at the reflecting interface. Amplitude correction factors have to be applied to the recorded data to obtain true amplitudes, necessary for the AVO analysis. These correction factors are essential for this method, because they dominate the AVO result.

- **OBH/OBS geometry**

When AVO analysis is applied to OBH/OBS data, the recorded reflection arrivals do not originate from one single reflection point. Due to the common-receiver geometry, OBH/OBS data record a reflection footprint of lateral extent (here about 150 m along the BSR to each side of the OBH/OBS). Amplitude variations recorded with OBH/OBS may be caused by lithological changes along this footprint and interfere with the AVO effect.

- **Tuning effect caused by thin layers**

The Zoeppritz equations are restricted to first order discontinuities. Thus, standard AVO methods, based on the Zoeppritz equations are not necessarily applicable on every reflection target. Here, the presence of a thin gas layer with gradually changing P-wave velocities below the BSR, causes a frequency dependent change of the AVO results, due to tuning effects.

In this Chapter, the first two restrictions are investigated in detail by focusing on amplitude correction factors and amplitude anomalies, caused by the asymmetric OBH/OBS geometry. The BSR interface is here assumed to be a first order discontinuity and a

conventional AVO analysis is applied to the data to compare theoretical results, based on the Zoeppritz equations. The effect of a thin layer below the BSR on the AVO result is discussed in Chapter 5, where the presence of thin layer is investigated in more detail. Here, the results are based on AVO analysis applied on a single interface.

4.3 Amplitude versus offset

4.3.1 Theory

AVO theory is based on the *Zoeppritz (1919)* equations, which express the reflection and transmission coefficients of a plane wave incident on a planar interface between isotropic and homogeneous media as a function of the angle of incidence and the properties of the media (Fig. 4.1).

The reflection of a compressional plane wave involves energy partition from an incident P-wave to (1) a reflected P-wave, (2) a transmitted P-wave, (3) a reflected S-wave, and

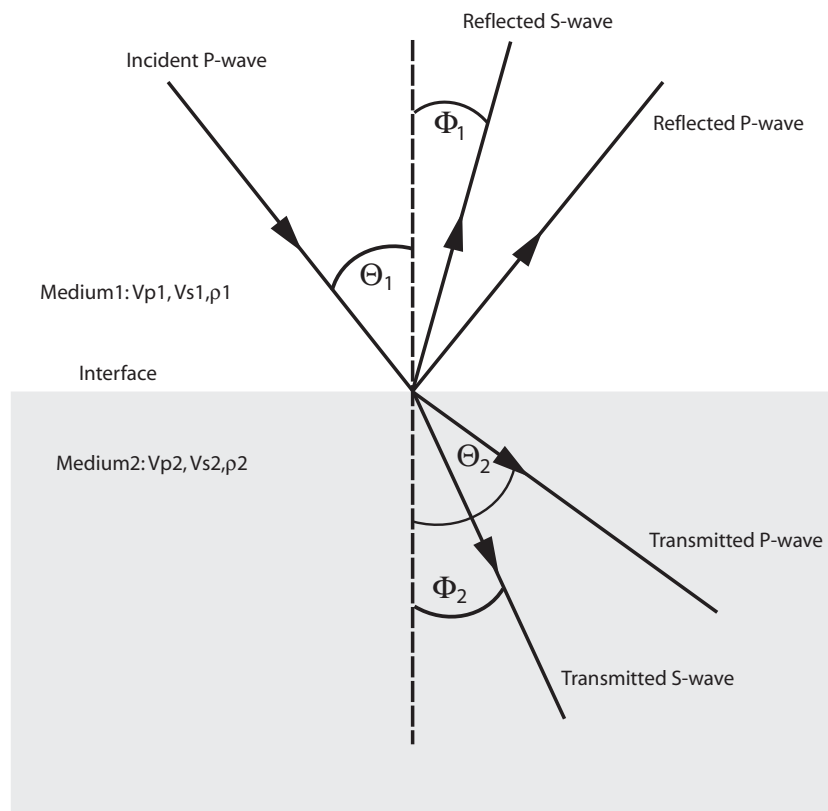


Figure 4.1: *Reflection and transmission at an interface between two elastic half-spaces for an incident P-wave.*

(4) a transmitted S-wave. The angles for the incident, reflected, and transmitted rays at the boundary are related to each other according to Snell's law,

$$p = \frac{\sin\Theta_1}{V_{p1}} = \frac{\sin\Theta_2}{V_{p2}} = \frac{\sin\Phi_1}{V_{s1}} = \frac{\sin\Phi_2}{V_{s2}}$$

where,

V_{p1} = P-wave velocity in medium 1,

V_{p2} = P-wave velocity in medium 2,

V_{s1} = S-wave velocity in medium 1,

Θ_1 = incident P-wave angle,

Θ_2 = transmitted P-wave angle,

Φ_1 = reflected S-wave angle,

Φ_2 = transmitted S-wave angle,

and p is the ray parameter.

The P-wave reflection coefficient as a function of incidence angle $R_{PP}(\Theta_1)$ is defined as the ratio of the amplitude of the reflected P-wave to that of the incident P-wave. Similarly, the P-wave transmission coefficient $T_{PP}(\Theta_1)$ is the ratio of the amplitude of the transmitted P-wave to that of the incident P-wave. Also, $R_{PS}(\Theta_1)$ is the ratio of the amplitudes reflected S-wave and incident P-wave, and $T_{PS}(\Theta_1)$ is the ratio of the transmitted S-wave and the incident P-wave amplitudes. At normal incidence, there are no converted S-waves and the P-wave reflection coefficient R_P is given by

$$R_P = \frac{I_{P2} - I_{P1}}{I_{P2} + I_{P1}} = \frac{1}{2} \frac{\Delta I_P}{I_{PA}} \approx \frac{1}{2} \ln(I_{P2}/I_{P1})$$

where I_P is the continuous P-wave impedance profile,

I_{P1} = impedance of medium 1 = $\rho_1 V_{P1}$

ρ_1 = density of medium 1

I_{P2} = impedance of medium 2 = $\rho_2 V_{P2}$

ρ_2 = density of medium 2

$I_{PA} = (I_{P1} + I_{P2})/2$

$I_P = I_{P1} + I_{P2}$.

The logarithmic expression is acceptable for reflection coefficients smaller than about ± 0.5 . The P-wave transmission coefficient T_P at normal incidence is given by

$$T_P = 1 - R_P$$

The variations of reflection and transmission coefficients with incident angle (and corresponding offset) is referred to as offset-dependent reflectivity and is the fundamental

basis for amplitude versus offset analysis. *Knott (1899)* and *Zoeppritz (1919)* invoked continuity of displacement and stress at the reflecting interface as boundary conditions. This leads to the reflection and transmission coefficients as a function of incident angle and of the elastic properties of the media (Zoeppritz equations). For small contrasts in the layer parameters and commonly encountered incident angles in seismic reflection applications, these equations can be accurately approximated (*Bortfeld, 1961; Richards and Frasier, 1976; Aki and Richards, 1980; Shuey, 1985*). For the analysis presented here, the *Aki and Richards (1980)* approximation is used:

$$R(\Theta) = a \frac{\Delta\alpha}{\alpha} + b \frac{\Delta\rho}{\rho} + c \frac{\Delta\beta}{\beta},$$

where

$$\begin{aligned} a &= 1/\cos^2\Theta \\ b &= 0.5 - ((2\beta^2/\alpha^2)\sin^2\Theta) \\ c &= -(4\beta^2/\alpha^2)\sin^2\Theta \\ \alpha &= (\alpha_1 + \alpha_2)/2 \\ \beta &= (\beta_1 + \beta_2)/2 \\ \rho &= (\rho_1 + \rho_2)/2 \\ \Delta\alpha &= \alpha_2 - \alpha_1 \\ \Delta\beta &= \beta_2 - \beta_1 \\ \Delta\rho &= \rho_2 - \rho_1 \\ \Theta &= (\Theta_i + \Theta_t)/2, \text{ where } \Theta_t = \arcsin((\alpha_2/\alpha_1)\sin\Theta_i) \end{aligned}$$

This approximation is appealing because it is written as three terms; the first involving P-wave velocity, the second involving density, and the third involving S-wave velocity. A comprehensive description of the AVO theory and practical methods is given by *Castagna and Backus (1993)*.

Two distinct characteristics are typical for a BSR reflection:

- the BSR reflection shows a clear phase-reversal compared to the seafloor
- the BSR reflection amplitudes increase with increasing incident angles (offsets)

The phase-reversal is commonly interpreted as the result of a negative impedance-contrast, due to a velocity inversion at the BSR. It has been widely accepted that the velocity inversion is caused by a high-velocity hydrated sediment layer overlying a low-velocity layer containing free gas at the phase boundary (GHSZ). Consequently the phase of the BSR signal is negative (Fig. 4.2). The absolute value of the reflection

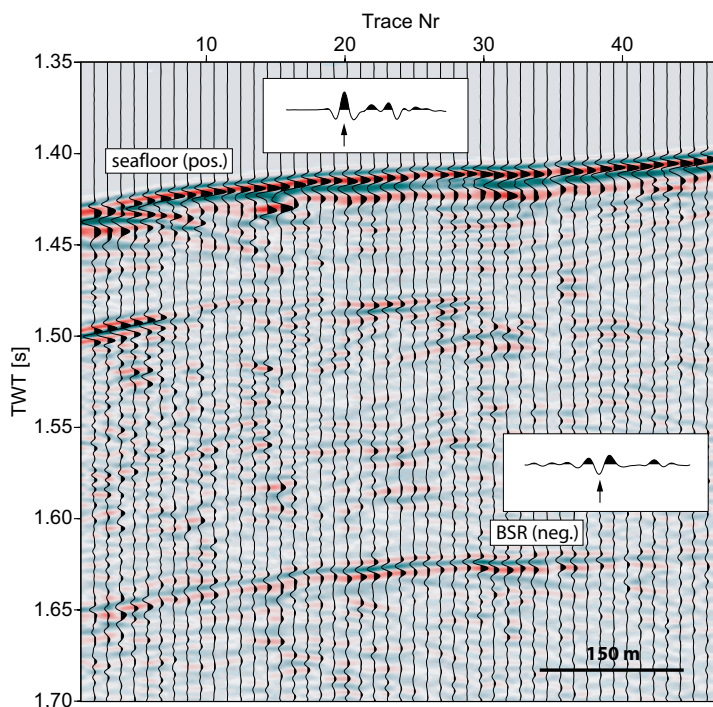


Figure 4.2: *Seismic section of the surface streamer presenting zero-offset data. The seafloor reflection phase is defined positive (trough-peak-trough), whereas the BSR phase is negative (peak-trough-peak), caused by the negative impedance contrast.*

amplitude in the OBH section increases with offset. The result is an angle-dependent amplitude reflectivity curve described by the Zoeppritz equations. In general, the P- and S-wave velocity and the density of marine sediments increase with depth as described in various investigations by *Hamilton (1971, 1972, 1976a,b, 1979b)*. The occurrence of free gas significantly changes the trend of the AVO-curve. *Rutherford and Williams (1989)* define three distinct classes for gas (in sand) AVO anomalies. Class 1 occurs when the normal incidence P-wave reflection coefficient is strongly positive and shows a strong amplitude decrease with offset and a possible phase change at far offset. Class 2, for small P-wave reflection coefficients, shows a very large percentage change in AVO. If the normal-incidence reflection coefficient is slightly positive, a phase change occurs at near or moderate offsets. Class 3 anomalies have a large negative normal-

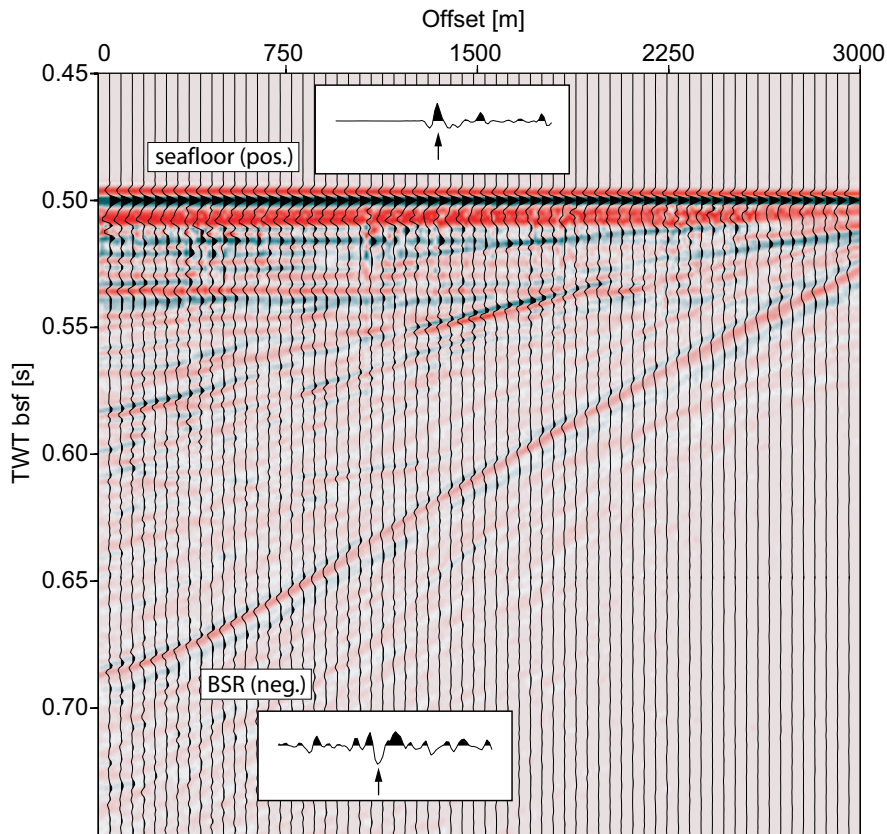


Figure 4.3: *Seismic section of wide-angle reflections, recorded with an OBH. The most prominent reflection is the BSR and its nearly constant amplitude trend over the entire offset range.*

incidence reflection coefficient, which becomes more negative as the offset increases. Class 3 is the classic bright spot.

After this classification the BSR is a class 3 bright spot. The data shown in Figure 4.3 are wide-angle reflections from an OBH. The data are statically shifted to a constant seafloor arrival. The amplitudes of the data shown in Figure 4.3 have not been corrected (geometrical spreading). However, the difference in the AVO-trend of the BSR compared to the other reflections can be described qualitatively. The BSR amplitudes in the data presented in Figure 4.3 maintain their value over the entire offset range. In contrast, all other reflections decay with increasing offset. Amplitude correction factors enhance the amplitudes with increasing offset. Consequently, amplitudes of the BSR are negative in polarity at vertical incidence and increase (more negative) with increasing offset to a class 3 AVO-trend. These AVO-trends can be analyzed and related to physical properties and consequently, to the gas hydrate content. An example

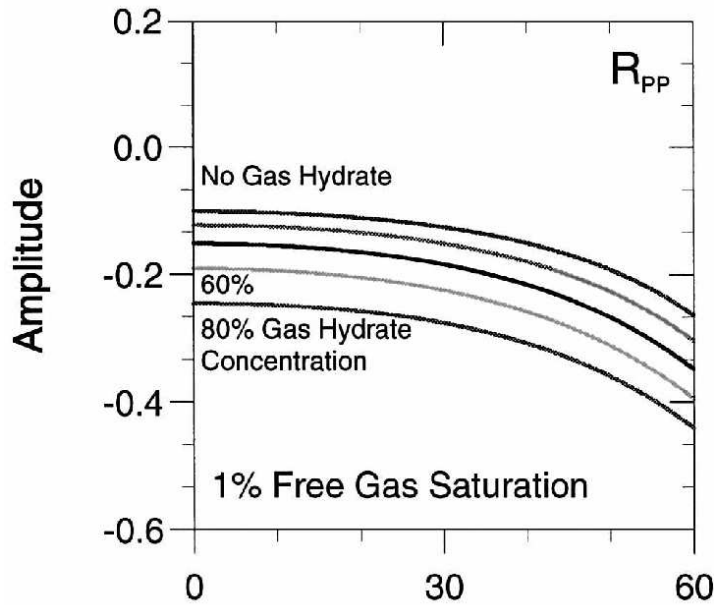


Figure 4.4: Computed variations of BSR P-wave viscoelastic reflection coefficient with angle of incidence for 1% free gas saturation and varying gas-hydrate saturations (taken from *Carcione and Tinivella (2000)*).

is shown in Figure 4.4, modified after *Carcione and Tinivella (2000)*. In this model 1% free gas is assumed beneath the BSR and AVO-trends were calculated for different gas-hydrate concentrations. The curve trends in Figure 4.4 are very similar to each other and only vary in their absolute values. The lower limit (no gas hydrate) is set to a vertical incidence reflection coefficient of about -0.1. *Haris (2003)* has applied a true amplitude migration on the MCS line OR02 (*MacKay, 1995*), which coincides with the main seismic line p173 analyzed in this thesis. *Haris'* analysis of angle-dependent reflectivity gathers (Fig. 4.5) result in a vertical-incident reflection coefficient of around -0.08. The absolute values of R_p are presented in Figure 4.5.

These two examples show the fundamental difficulties when the AVO analysis is applied to quantify the gas hydrate and free gas concentrations. The amplitudes of *Haris (2003)* displayed in Figure 4.5 show strong variations with changing angles. It is therefore the

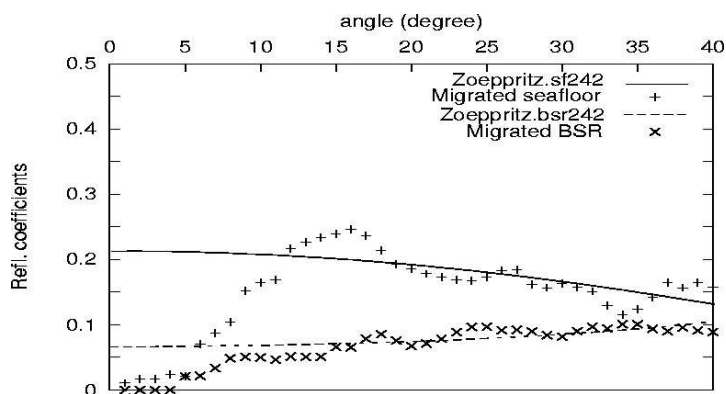


Figure 4.5: AVO-response from seafloor amplitudes and BSR (from *Haris, 2003*).

interpreters' choice to decide, which theoretical curve fits the observed amplitudes. Variations around 0.05 for the vertical-incidence reflection coefficient are not unusual. In the models analyzed by *Carcione and Tinivella (2000)*, displayed in Figure 4.4, an uncertainty in the zero-offset reflection coefficient of 0.05 would roughly result in an uncertainty of 30% in the gas hydrate saturation. Especially, when hydrate saturation is low, the ambiguity of the data results in too large uncertainties in the AVO analysis.

4.3.2 Amplitude corrections

Amplitudes are mainly affected by following aspects: (1) attenuation, (2) geometrical spreading, (3) source directivity and (4) receiver directivity.

Attenuation

Mechanisms for seismic wave attenuation in marine sediments are not clearly understood, neither are their effects on seismic pulses. However, from the number of contributing mechanisms identified, the most significant appear to be fluid-flow and frictional mechanisms. The fluid-flow mechanisms involve the flow of fluids in the pores and cracks of saturated and partially saturated rocks (*Winkler and Nur, 1982*). Frictional mechanisms involve friction between cracks and grains (*Johnston et al., 1979*). Generally the rate of attenuation appears to be proportional to frequency. As a result of attenuation, high-frequency components of pulses are lost more rapidly than low-frequency components. Therefore attenuation causes pulses to broaden with increasing traveltime. Definitions and terminology used in attenuation studies were summarized in *Toksöz and Johnston (1981)*.

Attenuation of P-wave amplitudes of the data presented in this study is believed to only have a constant effect on the absolute amplitude values. This effect is considered to be relatively small, since the depth interval investigated in this study is less than ~ 130 m. However, attenuation probably plays a more important role on shear-wave studies. Shear-wave attenuation on data collected at Northern Hydrate Ridge was carried out by *Petersen (2004)*. In this study, attenuation is not taken into account.

Spreading and Directivity

The aspects of source and receiver directivity as well as geometrical spreading can be discussed together. The sources and hydrophones used during the HYDGAS cruise do not show any varying radiation pattern or receiver characteristics. Therefore it is assumed that no directivity correction factor is necessary for the data in this study. However, the directivity pattern of the marine sources do in fact have a changing trend depending on the emitting angle. This change is due to the interference pattern of the

primary 'down-going' wave and the 'ghost' reflection. The source ghost is the down-going reflection from the free surface of the up-going wave from a source several meters below the sea surface (Fig. 4.6).

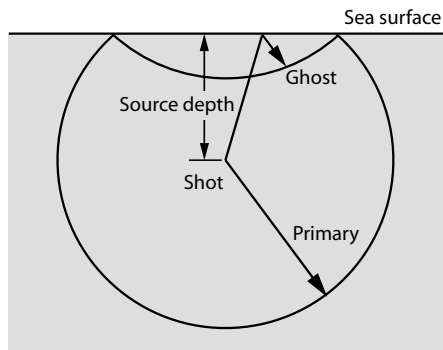


Figure 4.6: *A marine source towed at depth behind the vessel produces a direct down-going pulse and secondary "source ghost" caused by the reflection of the direct up-going pulse from the free surface.*

In most cases the down-going source pulse and the ghost interfere to form a single "effective" wavelet that propagates into the subsurface. An up-going compression recorded with a geophone causes a positive pulse, a down-going compression will give a negative pulse, whereas both waves will give a pulse of the same kind on a hydrophone. This observation can be used to attenuate near-surface reverberations when geophones and hydrophones are combined at OBH/OBS (*Sheriff and Geldart, 1995*). The 180° reversal of phase upon reflection at the free surface causes a hydrophone to see a polarity reversal of the ghost with respect to the primary impulse, whereas a velocity phone sees also the reversal of wave direction and hence sees the ghost and primary with the same polarity. Other methods of source-ghost deconvolution are given by e.g., *Lindsey (1960)* and *Hammond (1962)* but are not investigated further in this study. Before deepening the analysis on the ghost signal interference, geometrical spreading is discussed.

Geometrical spreading is related to the amplitude decay of a wavefront as it propagates with distance. A single shot is thought of as a point source that generates a spherical wave field. In a homogeneous medium, energy density decays proportionally to $1/R^2$ where R is the radius of the wavefront. Wave amplitudes are proportional to the square root of energy density, thus they decay with $1/R$.

The water column can be considered as a homogeneous layer with a constant seismic velocity (here 1480 m/s), therefore the decay is proportional to the one-way travel-time in the water column. In terms of amplitudes in the OBH/OBS data, the direct wave should be corrected for with a factor proportional to T , where T is the one-way traveltime. In case of a correctly applied spreading factor the amplitudes of the direct wave are expected to be constant (Fig. 4.7). Having applied a spreading factor of T (middle panel, Fig. 4.7), which theoretically is correct for the direct wave, the amplitudes still show a decreasing trend. The area marked as 'clipped data' refers to the

over-amplifying of the hydrophones, mentioned in chapter 4. These amplitudes have to be ignored. Constant amplitudes (lower panel, Fig. 4.7) and therefore corrected properly, are obtained after applying a spreading factor of T^2 , which is only applicable for the direct wave. This effect is linked to an interference pattern of the primary and the ghost signal, which is associated with amplitude changes. The correct amplitude factor depends on the takeoff-angle at the source, given by $1/\cos \Phi$. Amplitudes have to be multiplied by this factor, which in case of the direct wave is proportional to the traveltime T . Two synthetic seismograms (Fig. 4.8) are calculated to illustrate the interference effect.

A model is used, where the source depth is larger than the signal wavelength. This is implemented to completely separate the ghost signal and the primary arrival for the near offsets. In contrast to the lower panel of Figure 4.8, showing a clear interference effect, no ghost interference is calculated in the synthetic section displayed in the upper panel. The amplitudes and the effect of a correction factor of $1/\cos \Phi$ is displayed in

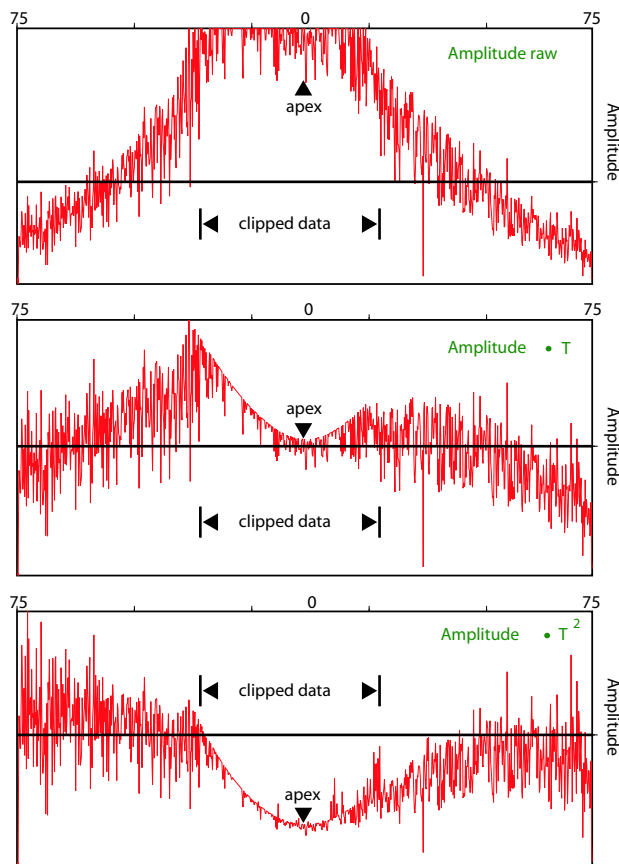


Figure 4.7: *Picked amplitudes of the direct water-wave collected with an OBH/OBS. The upper panel shows the raw amplitudes not corrected. Correction factors of T and T^2 are applied to the amplitude in the middle and lower panel, respectively.*

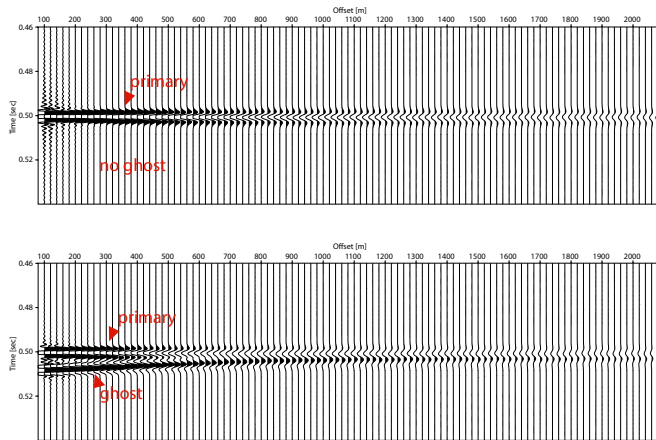


Figure 4.8: *Synthetic seismograms showing the effect of the ghost interference. Upper panel: No ghost reflection; Lower panel: computed with ghost-reflection. The difference is clearly visible in the range, where the ghost interferes with the primary arrival.*

Figure 4.9. To compensate for the ghost interference (blue curve), a correction factor of $1/\cos\Phi$ is applied to the amplitudes. The red curve in Figure 4.9 represents the amplitudes of both, primary and ghost, whereas the green curve displays amplitudes of a modeled direct arrival without ghost interference. Compared to the synthetic models, the recorded data already comprise phase interference at zero-offsets. This is due to the greater wavelength of the source signal of the collected data. The sources used during the HYDGAS cruise were towed roughly 5 m below the sea-surface. In conclusion, the results of this analysis provide an angle-dependent correction factor of $1/\cos\Phi$ to correct for the ghost interference. In total, the amplitudes of the OBH data need to be corrected twice: (1) for a spreading factor equal to the travel-distance of the recorded wave and (2) for an angle dependent correction factor.

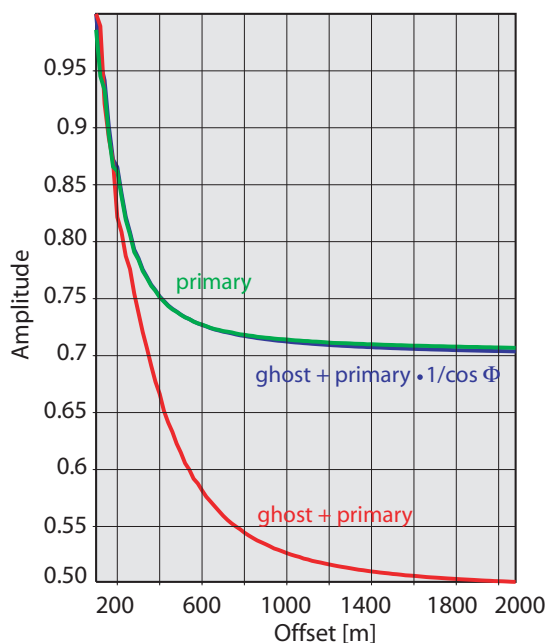


Figure 4.9: *Amplitudes of synthetic direct arrivals, calculated with and without ghost interference, respectively. The green curve represents amplitudes of the direct arrival without ghost interference (compare with Fig. 4.8, upper panel) The red curve represents the arrival interfering with the ghost signal (compare with Fig. 4.8, lower panel). By multiplying the red curve (ghost + primary) with $1/\cos\Phi$ the ghost interference is compensated (blue curve).*

4.4 AVO anomalies

On the western flank of the ridge, various amplitude variations along the BSR are observed (Fig. 4.10). Three ocean bottom stations (OBS 61,62 and 63, Fig. 4.10) recorded wide-angle reflections, shot with three different sources. The three OBS are located right above the observed amplitude variations and are used to localize amplitude anomalies related to subsurface heterogeneities. For a better understanding of the different processes used in the following analysis, a flowchart is presented in Figure 4.11. Before analyzing the data, a brief outline of the theoretical approach is presented first.

The theoretical approach is to subtract a mean sedimentary background-AVO trend from the picked anomalous OBH/OBS data in relation to the subsurface reflection point. In the first step the data is statically corrected for a constant direct arrival, as described earlier, to increase the coherency. Next, the raw amplitudes of the BSR are picked manually. With the given velocity model obtained from the travelt ime inversion, forward ray-tracing is carried out to derive the exact geometry of arrivals. The knowledge of the accurate ray-geometry is a fundamental objective for this method. In first place it defines the point at which the arrivals reflect at the BSR. Secondly, the ray-geometry provides necessary information on the angle of the emitting source signal. This is used to apply the angle dependent amplitude correction factors. After all correction factors are applied, the amplitudes are calibrated to a best fit theoretical AVO-trend, based on the *Zoeppritz (1919)* equations. Finally, the subtraction of the

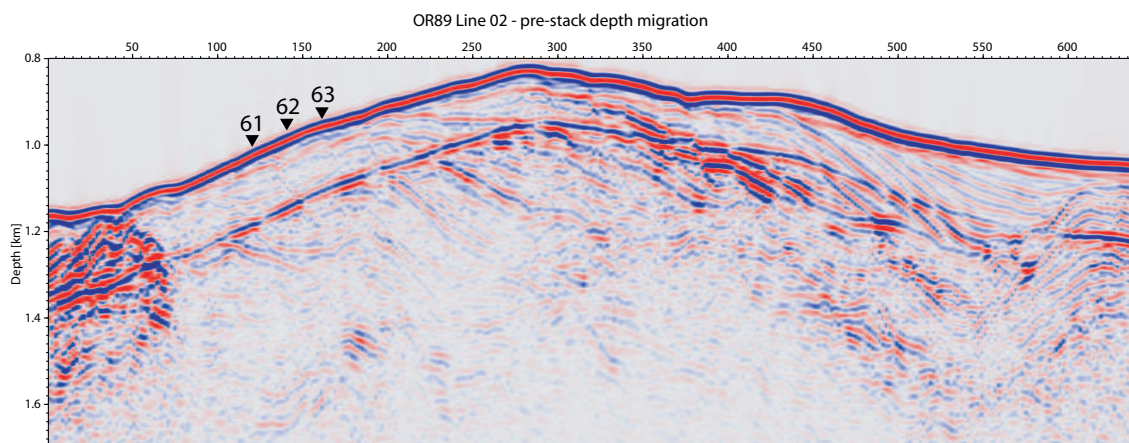


Figure 4.10: *True amplitude (TA) pre-stack depth migration of line OR02 (MacKay, 1995), coincident with the main seismic line p173 analyzed in this thesis and showing the location of OBS 61, 62, and 63, taken from Haris (2003).*

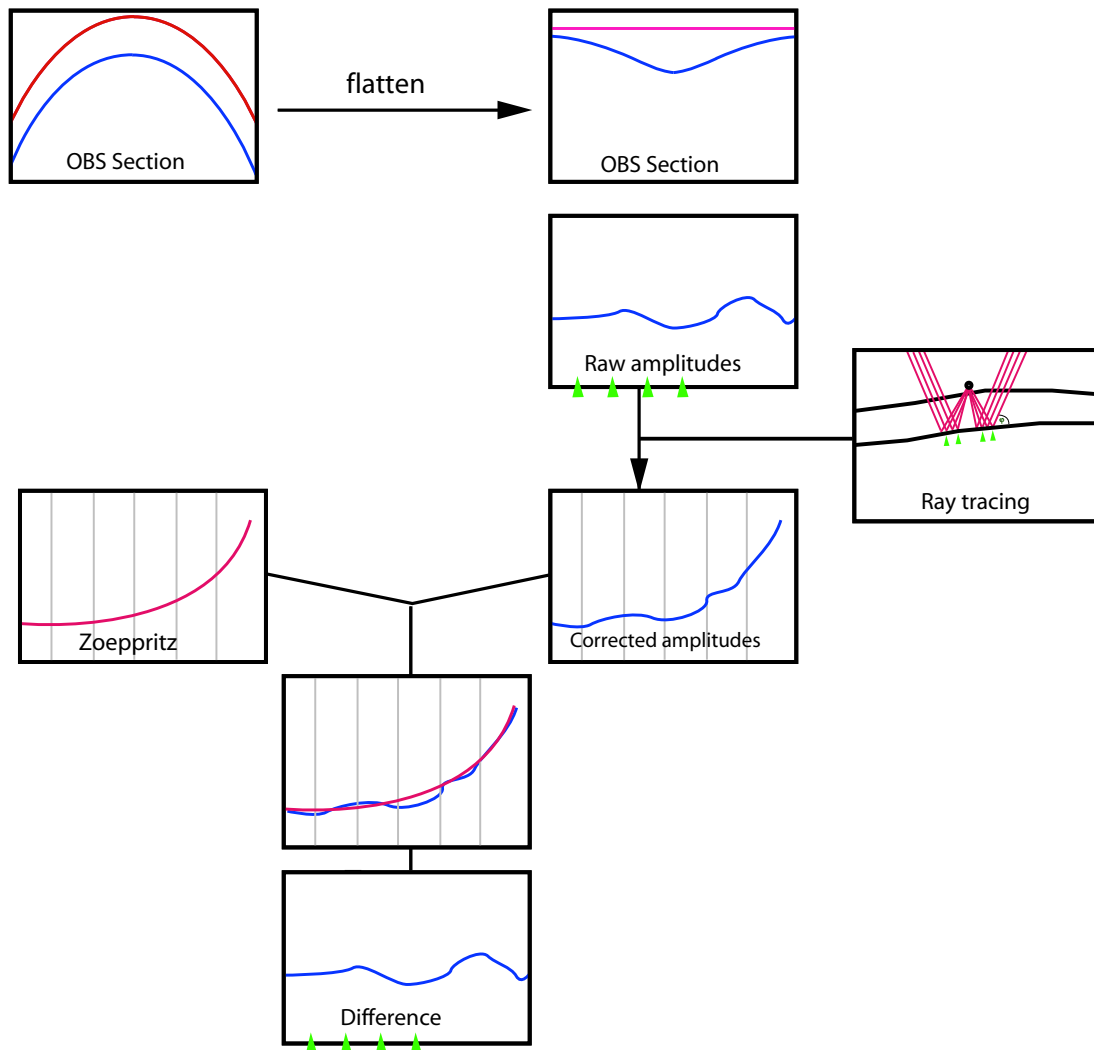


Figure 4.11: *Flowchart presenting the main steps of the analysis method described in this chapter.*

theoretical curve from the picked amplitude curve results in an amplitude pattern, directly linked to the subsurface.

One aspect of investigating wide-angle reflections recorded with OBH/OBS is the asymmetric acquisition geometry. Conventional multi-channel seismic (MCS) data is acquired by towing the streamer close to the sea surface, while the vessel moves along the desired line. The purpose of multi-channel seismics lies in the multi-coverage (multi-fold) of subsurface reflections for different angles (offsets). This means that one single point in the subsurface provides reflection arrivals of different angles (CRP - common reflection gathers). In a strict sense, only amplitudes from one single reflection point

can be used for conventional AVO.

In contrast to MCS data, reflection arrivals recorded with ocean bottom instruments (common-receiver geometry) originate from different subsurface locations (Fig 4.12). The reflection point moves or 'smears' to a lateral extending footprint.

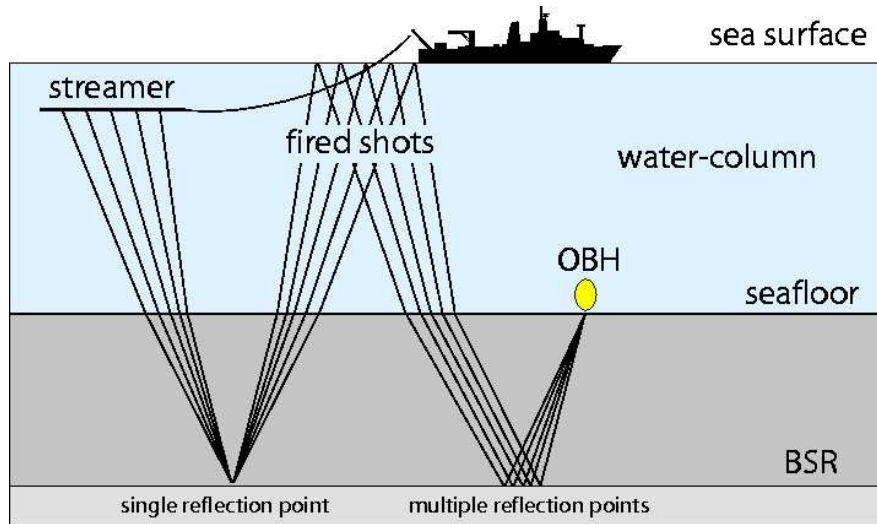


Figure 4.12: *Cartoon showing the two different receiver geometries. Single reflection points are multi-covered in the MCS (streamer) configuration. OBH/OBS record reflections from a range of subsurface point.*

Thus, when analyzing wide-angle OBH/OBS data, we have to keep in mind, that reflections do not originate from a single subsurface point. Depending on the depth of the reflector, the reflection footprint can have an extent of several hundred meters. Observed amplitude anomalies in the AVO-curve therefore likely occur due to sub-seafloor variations along this footprint. These anomalies do not necessarily have to complicate AVO analysis. The method used here, takes advantage of the asymmetric OBH/OBS geometry to relate AVO anomalies to subsurface variations.

At the beginning of the analysis process, the raw reflection amplitudes of the BSR are picked manually. Figure 4.13 presents the amplitude picks of the three OBS hydrophone data and the seismic sections, respectively. Amplitudes were picked from GI-gun-, airgun- and sparker-data. The most prominent observation in all sections is that the amplitudes of the BSR remain nearly constant over the entire offset range. In comparison, other than the BSR reflection show a decreasing trend in amplitudes with increasing offset. The amplitudes are now assigned to the sub-seafloor reflection point (along the BSR), from where they were reflected. Forward modeling, using the ray-tracing method, is used to derive the necessary ray geometry. Not only the reflection

point at the BSR is determined, but the incident angles at the BSR interface are calculated as well. After assigning the raw amplitudes to a subsurface coordinate and having derived the incident angles for each reflection point, raw amplitudes are corrected and calibrated to known reflection coefficients. As it shown in Figure 4.13, the amplitudes of the BSR are roughly constant over the entire offset range. An AVO analysis applied on the raw amplitudes would yield wrong interpretations. Only after

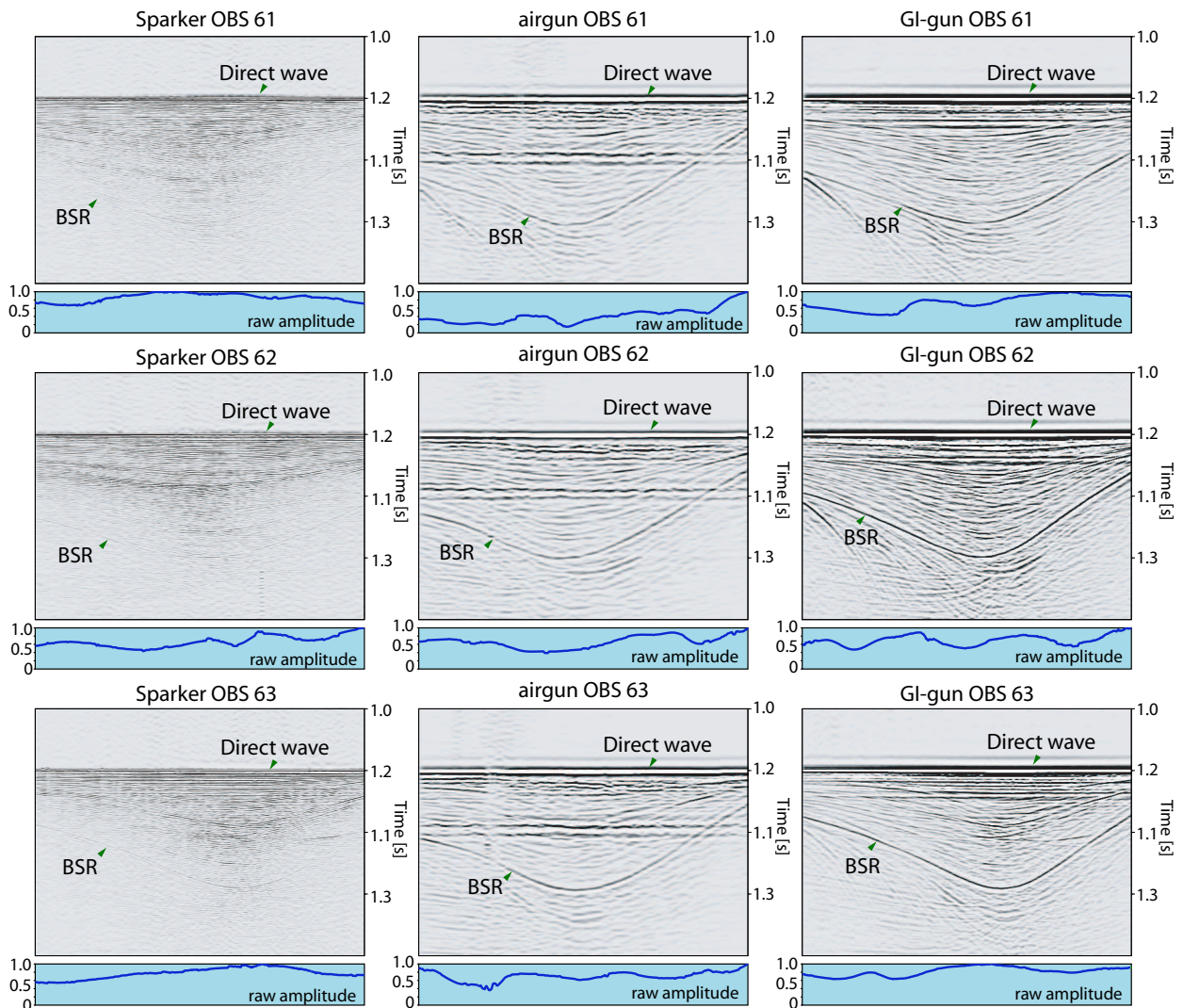


Figure 4.13: *Seismic OBS sections (hydrophone component) statically shifted to a constant direct arrival. Underneath each section, the picked BSR amplitudes are presented. From left to right: sparker, airgun and GI-gun data. From top to bottom OBS 61, OBS 62 and OBS 63, respectively. Normalized raw amplitude values are displayed.*

applying amplitude correction factors, the true AVO trend can be determined. In the data presented here, the mean trend of the raw BSR amplitudes is roughly constant and therefore, the true AVO trend is mainly influenced by the applied correction factors. In other words, the amplitude correction process will essentially determine the resulting AVO trend. Returning to the AVO analysis of the three OBS stations 61, 62, and 63, correction factors are now applied to the picked raw amplitudes (Fig. 4.14). The necessary information of take-off angles and the travel-distances are derived from ray-tracing methods. The raw corrected amplitudes are calibrated to the vertical incidence reflection coefficient of the BSR, derived from SCS data, which are calibrated to the seafloor reflection coefficient. The seafloor reflection coefficient is derived from both, streamer (SCS) and OBH (on rope) data. The reflection coefficient obtained from the SCS data is calculated by picking the primary seafloor reflection and the first multiple reflection respectively (*Backus, 1959*). The reflection coefficients range from ~ 0.19 to 0.21 , and are having a mean value of 0.2 . To derive the reflection coefficient from OBH data, only stations not fixed at the seafloor can be used, due to the 'clipped' first arrivals, which are caused by the coincident arrival of the direct wave and the seafloor reflection. Hence, OBH floating 200 m above the seafloor are used to pick amplitudes of the seafloor and the first multiple. The resulting seafloor reflection coefficient of 0.19 fits the range of the SCS data. The picked raw amplitudes, corrected for spreading,

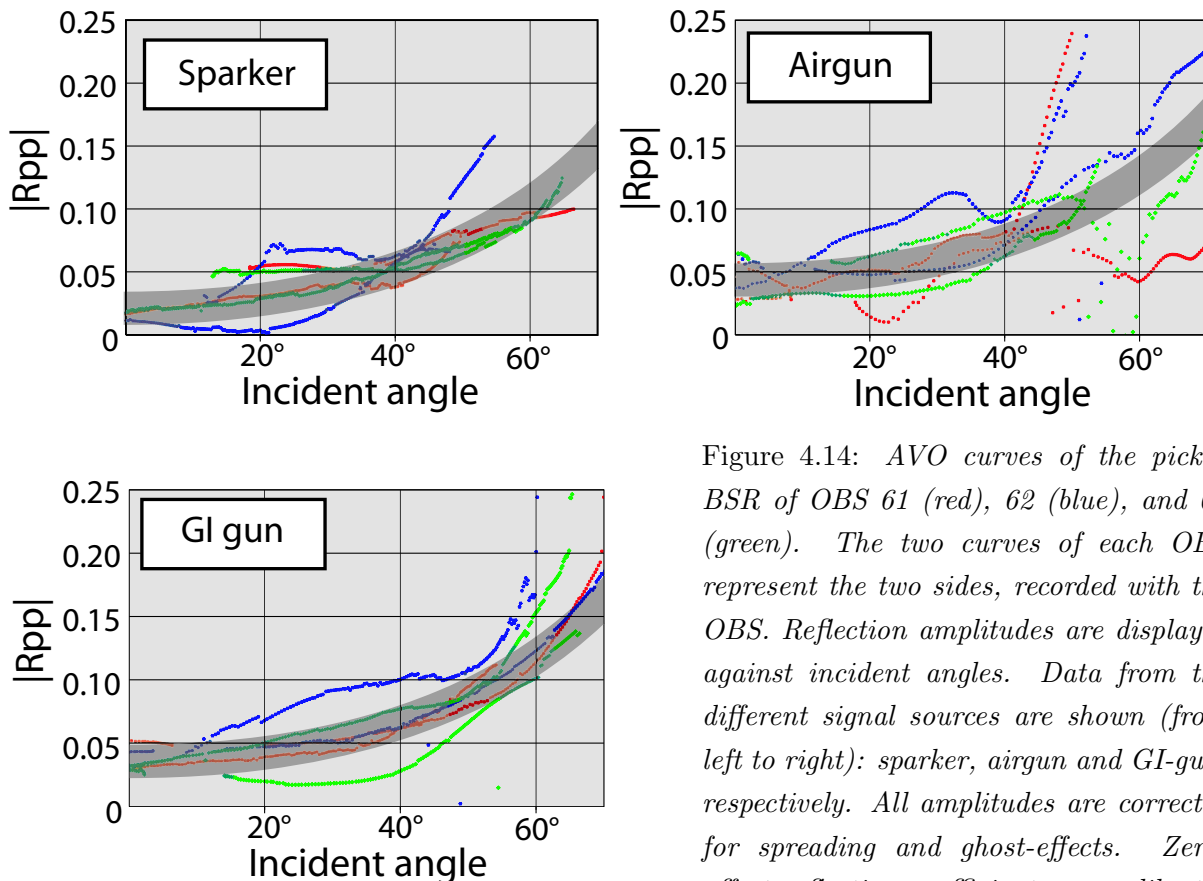


Figure 4.14: AVO curves of the picked BSR of OBS 61 (red), 62 (blue), and 63 (green). The two curves of each OBS represent the two sides, recorded with the OBS. Reflection amplitudes are displayed against incident angles. Data from the different signal sources are shown (from left to right): sparker, airgun and GI-gun, respectively. All amplitudes are corrected for spreading and ghost-effects. Zero-offset reflection coefficients are calibrated to the SCS data.

ghost-effect and calibrated to a seafloor-reflection coefficient of 0.2 are displayed in Figure 4.14.

The next step involves the subtraction of a mean best-fit theoretical AVO curve, based on the Zoeppritz-equations (Fig. 4.16). This method basically removes the AVO-trend from the wide-angle reflection data and projects the amplitudes to a pseudo vertical-incidence domain, which are then comparable to the zero-offset section of the streamer data (Fig. 4.15).

While finding an accurate theoretical trend, the interest is focused on reducing the AVO-trend to a plain level. Good correlation of the AVO anomalies only occur locally, e.g. arrow in Figure 4.16. This anomaly is present in the airgun data of OBS 61 and OBS 62. In the GI-gun data, this anomaly is at OBS 61, but not at OBS 62. Comparing the amplitude variations analyzed above with the migrated MCS data (Harris, 2003) displayed in Figure 4.10, the anomaly coincides with a stronger reflection between OBS 61 and OBS 62. Other correlations are not confidently constrained.

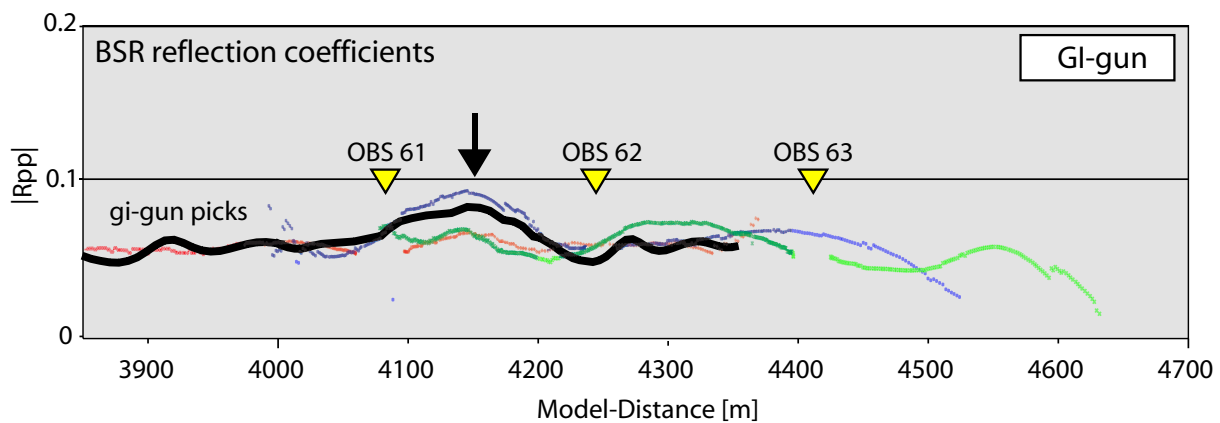


Figure 4.15: *Projected BSR reflection coefficients, derived from the AVO curves of OBS 61 (red), 62 (blue), and 63 (green), as in Figure 4.15, now reduced to the vertical incidence case. The high amplitudes between OBS 61 and 62 correlate with the amplitudes of the SCS data (black line).*

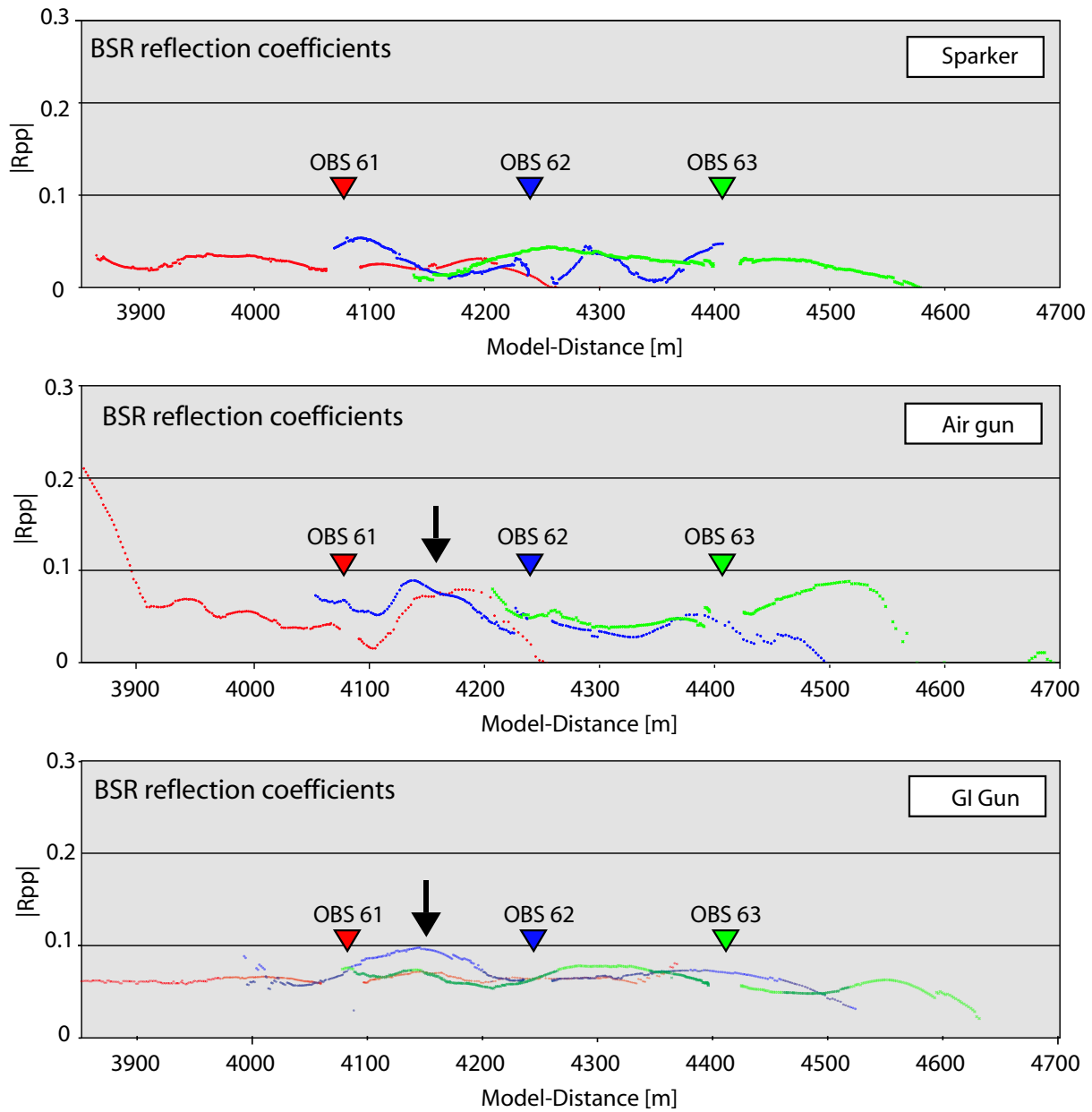


Figure 4.16: Projected BSR reflection coefficients of OBS 61 (red), 62 (blue), and 63 (green), as in Figure 4.15, now reduced to the vertical incidence case. Amplitudes of (from top to bottom) sparker, airgun and GI-gun. The higher reflection (arrow) between OBS 61 and OBS 62 can be derived from two adjacent instruments.

4.4.1 Summary

Only one prominent amplitude anomaly can be related to variations along the BSR, which is also observed in the migrated MCS section. All other anomalies correlate locally but no clear trend is noticeable. Because the AVO trend is very sensitive to the amplitude correction factors, the inversion of an accurate velocity model is inevitable for this method. Correction factors are mainly calculated from forward modeling methods and therefore indirectly derived from the velocity depth distribution and the geometry of the BSR reflector. Consequently, inaccurate velocity models provide incorrect amplitude correction and geometry parameters and finally lead to false AVO results and consequently to dislocations of the anomalies. Thus, the good correlation of this anomaly in the OBS data can be seen as an additional constraint for the accuracy of the inverted velocity model.

4.5 Quantitative AVO

4.5.1 AVO on OBS 61-63

In this paragraph standard AVO-analysis, based on the Zoeppritz equations, is used to derive the following seismic parameters: P-wave velocity V_P , S-wave velocity V_S and density ρ at the BSR interface in this high velocity region. The corrected amplitudes of the GI-gun data of OBS 61, 62, and 63 are used to derive these parameters. Depending on the seismic source, the reflection coefficients derived from the single channel streamer (SCS) data, result in different values for the BSR reflection coefficient. This frequency dependency will be presented in more detail further below. The results of AVA modeling done by *Haris (2003)* in this region provided a vertical incidence reflection coefficient at the BSR of about -0.6 (compare Fig. 4.5). The data of OBS 61, 62 and 63 are now calibrated to this value. The resulting AVO-response is presented in Figure 4.17. The shaded area in the left panel of the Figure represents the possible theoretical curves fitting the data. The seismic parameters used for the calculation are displayed in the right panel. The red line in the right panel of Figure 4.17 represents the mean value for the parameter range. A slight decrease in the density values is used here, whereas a constant density-gradient also fits the data within the uncertainty. Shear-wave velocities show the strongest variations, as they mainly influence the shape (curvature) of the AVO curve. Shear-wave velocities predicted by *Hamilton (1976a)* for a depth of ~ 150 m support values of from 370 m/s to 400 m/s. The change of the S-wave velocity at the BSR is preferred to be less drastic as the analysis predicts. The P-wave velocities above the BSR, ranging from 1560 m/s to 1620 m/s correlate

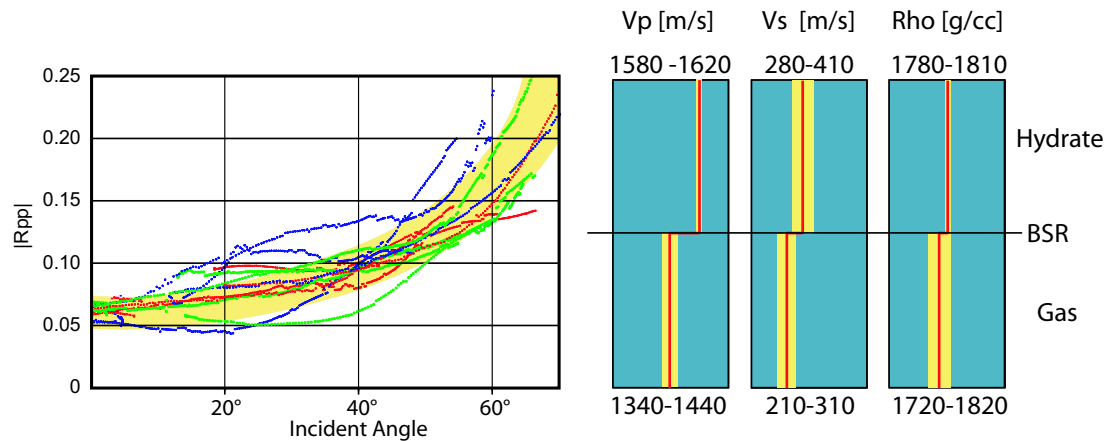


Figure 4.17: *AVO response (left panel) of OBS 61 (red), 62 (blue) and 63 (green), calibrated at a vertical incidence BSR reflection coefficient of -0.06. The shaded area illustrates the possible theoretical curves fitting the data. The seismic parameters V_P , V_S , and ρ , used for the calculation of the theoretical curves, are displayed in the right panel.*

with the inverted velocity model and the results of the velocity analysis in this region. These are related to relative 'faster' but not hydrated sediment. To summarize the results of this analysis, one important aspect can be concluded: The amplitude variations along the BSR are not necessarily related to hydrate formation above it. Strong amplitudes might be the result of a higher impedance contrast due to higher velocities caused by lithological changes. Amplitude variations can additionally be caused by varying gas saturations underneath the BSR. Consequently, amplitude variations need to be interpreted in combination with geologic units above the BSR and possible saturation changes of the free gas below. Therefore, additional interest is focused on the low P-wave velocities below the BSR, here between 1340 m/s and 1440 m/s. These are probably related to free gas in the sediment. These velocities are derived from amplitudes that were calibrated to a vertical angle reflection coefficient at the BSR of -0.06. Smaller reflection coefficients of about -0.04 result in a less drastic decrease of the P-wave velocities. Therefore, it is difficult to quantify the amount of free gas beneath the BSR, since an accurate calibration to acoustic log data is needed. The other aspect, which have to be considered, is the assumption of the BSR representing a first order discontinuity, to allow the standard Zoeppritz-based AVO analysis. To investigate this effect, an AVO analysis is applied to a log-based synthetic seismogram in comparison to a real data set, presented in the next section.

4.5.2 AVO modeling at ODP Site 1244

ODP leg 204 (see Chapter 6 for details) provided acoustic log information to verify the amplitude analyses. At ODP Site 1244, acoustic logs (Fig. 4.18) are used to compare calculated synthetic sections (Fig. 4.19) with the GI-gun data of OBH 66. OBH 66 is located roughly 200 m away from Site 1244, but is the closest of all deployed stations (compare Fig.6.7). In the log of Site 1244, there is no significant decrease in V_p below the BSR. However, a significant BSR is clearly visible in the recorded data of OBH 66 (lower panel, Fig. 4.19). The amplitudes of the recorded data are calibrated to the seafloor reflection coefficient of the synthetic modeled seafloor ($R_{Seafloor} = 0.19$). The reflection arrivals in the synthetic seismogram (upper panel, Fig. 4.19) do not show a significant BSR, due to the strong reflection pattern of the deeper arrivals. However, by picking the BSR amplitudes of the modeled and recorded data set, the trend is very similar (Fig. 4.19, red curves below each seismogram). Theoretical AVO curves of different physical properties are calculated and presented in Figure 4.20. A good fit (green curve) for the vertical reflection coefficient of 0.02 is achieved when V_p decreases from 1580 m/s to 1520 m/s and V_s and the density remain unchanged at the interface

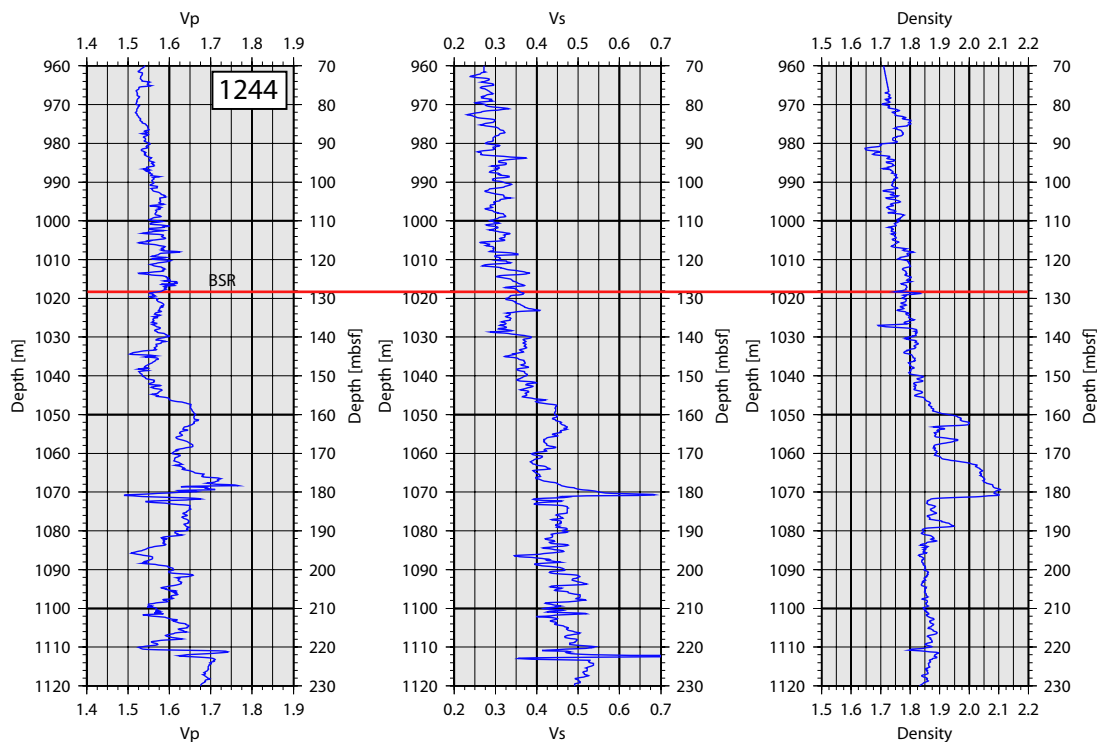


Figure 4.18: Sonic log (V_p and V_s) and density log of Site 1244. The red line marks the depth of the BSR. There is no significant decrease in V_p below the BSR, which might suggest the presence of free gas.

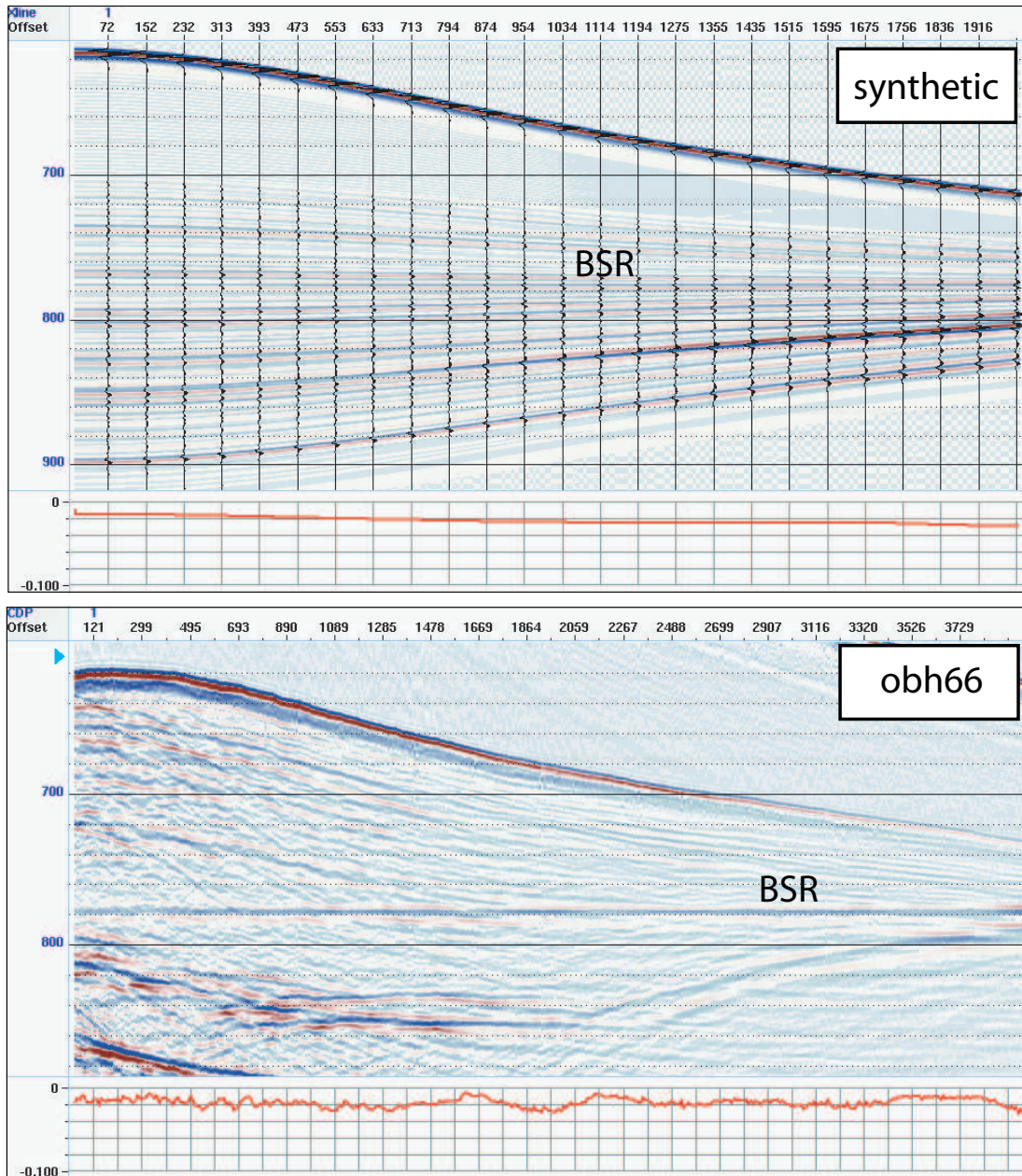


Figure 4.19: *Synthetic seismogram calculated with an extracted GI-gun source wavelet (top panel) and recorded data of obh66 (bottom panel). Both sections are statically shifted for a constant BSR arrival. The amplitudes of the BSR are displayed within the panels below the data.*

(a.). However, the trend with increasing incident angles does not correlate very well. In panel (c.) a decrease of both, V_s and V_p is calculated, whereas the density remains unchanged. A similar result to panel (a.) is observed with a less steep AVO-trend. Panels (b.), (d.), (e.), and (f.) are all very similar, and all models fit the data. Panel (f.) is chosen as the preferred model. Here, V_p is decreasing from 1580 m/s to 1490 m/s, V_s is increasing from 360 m/s to 380 m/s, and the density is slightly increasing

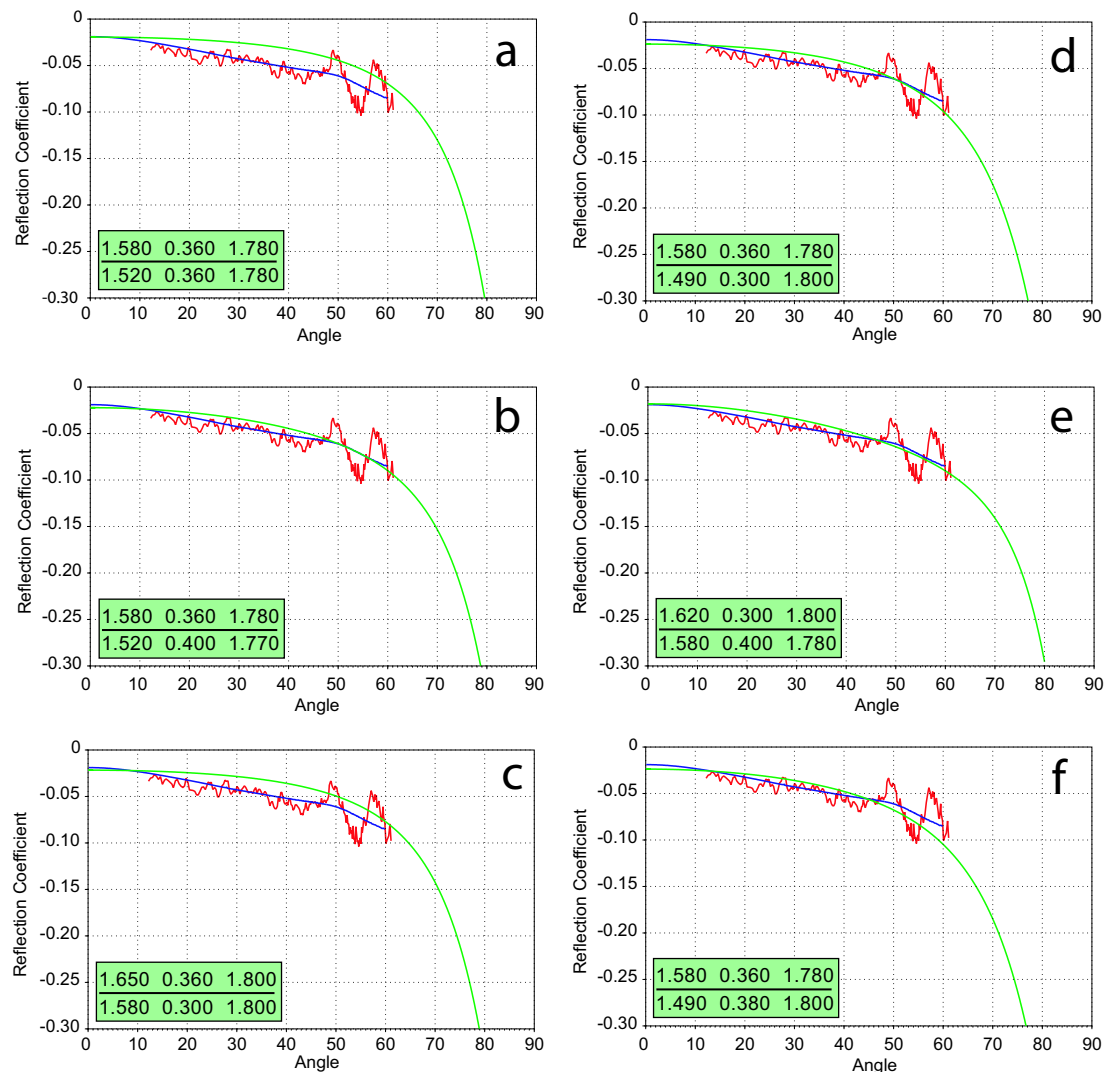


Figure 4.20: Theoretical curves after *Zoeppritz (1919)* (green) for different values of V_p , V_s , and density (a-f). Red curve displays the amplitudes of the real data obh66 and blue curve: synthetic amplitudes calculated from the logs of Site 1244. V_p , V_s and density (from left to right) used for the calculation are displayed in the inlet of each panel, representing the top and bottom parameters for the BSR interface

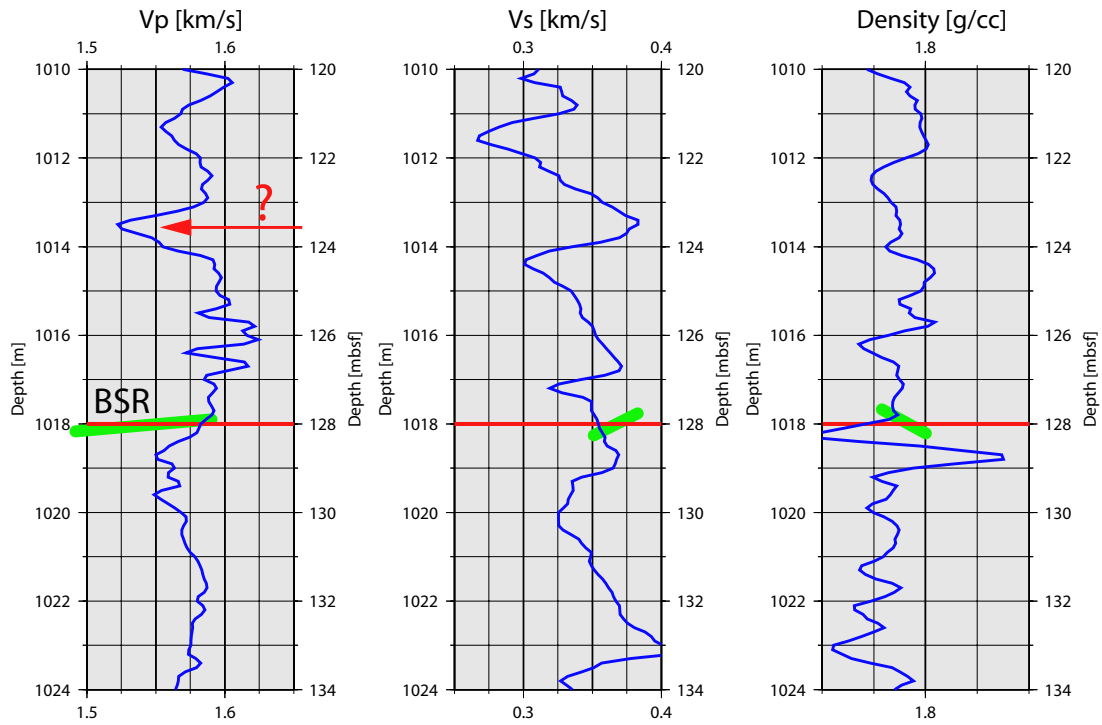


Figure 4.21: Close-up of the physical properties, logged at Site 1244. The BSR was defined at a depth of ~ 128 mbsf (below seafloor). The green bars mark the preferred model parameters, derived from the AVO analysis.

from 1780 g/cc^3 to 1800 g/cc^3 . A comparison of these parameters to those logged during the ODP Leg 204 is presented in Figure 4.21. The close-up of the logs show no significant change neither in V_p , V_s nor in the density. The preferred model parameters are displayed with green bars in Figure 4.21. Although the change of parameters at the BSR interface does not correlate very well, the general range of the parameters derived from the AVO analysis is within the logged values (blue curve). The biggest mismatch of the compared values is within V_p . This is assumed to be the result of the escaped gas before actual logging was carried out. Therefore, it is difficult to quantify the amount of free gas beneath the BSR by means of log-modeling.

4.5.3 Summary

The AVO analysis provides a good estimate on the physical-parameter range near the BSR interface. The analysis of the three OBS results in a V_p -velocity of about 1600 m/s at the top of the BSR, which is near the velocity of 1620 m/s, derived from the travelt ime inversion. The velocities below the BSR are lower with values of between 1340 and 1440 m/s, which is a clear indication for the presence of free gas. The

analysis at ODP Site 1244 shows a similar result. The general parameter range is within the values, obtained from the sonic and density log of ODP Site 1244. However, the preferred model, derived from the theoretical AVO curves, suggest a decrease of V_p of 1580 to 1490 m/s below the BSR. The analysis suggests that free gas must be present below the GHSZ, as indicated by the decrease of the P-wave velocity. Because the existence of a gas layer of several 10 m is in contrast to travelttime considerations, the only possibility to satisfy both observations is the presence of a relatively thin gas layer.

4.6 Conclusion

The AVO analysis, presented here, is severely influenced by amplitude correction factors and the asymmetry of the OBH/OBS geometry. While amplitude correction factors mainly contribute to the general AVO-trend, the OBH/OBS geometry is responsible for a reflection footprint and consequently produces amplitude anomalies within the AVO-trend. The knowledge of an accurate velocity-depth distribution is essential for considering these two aspects. An inaccurate velocity model inevitably leads to incorrect amplitudes and consequently to misinterpretations of the AVO results. The correlation of significant amplitude anomalies in adjacent OBH/OBS data sets can be used to verify the velocity model. By applying standard AVO analysis, the general range of the physical parameters at the BSR interface can be determined with the comparison to theoretical models, based on the Zoeppritz equations. However, the ambiguity in the P-wave velocity below the BSR is probably due to the approximation of the BSR representing a single interface. The existence of a thin gas layer below the BSR and the general effect on the AVO analysis is discussed in the following chapter.

5 Frequency Analysis

5.1 Introduction

A number of different amplitude variations of the BSR amplitudes are observed across Southern Hydrate Ridge. Their characteristics are:

- at low frequencies: high amplitudes and large amplitude variations
- at high frequencies: low amplitudes and small amplitude variations
- a change of the seismic wavelet along the BSR

The BSR seems to disappear in the high frequency data (sparker) compared to the continuous reflection in the GI-gun data at medium frequency ranges, and it has maximum amplitudes at the low frequencies generated by the airgun-array in the MCS data (Fig. 5.1). Certainly, the first explanation is a frequency-dependent amplitude behavior caused by attenuation effects. However, attenuation causing these strong amplitude

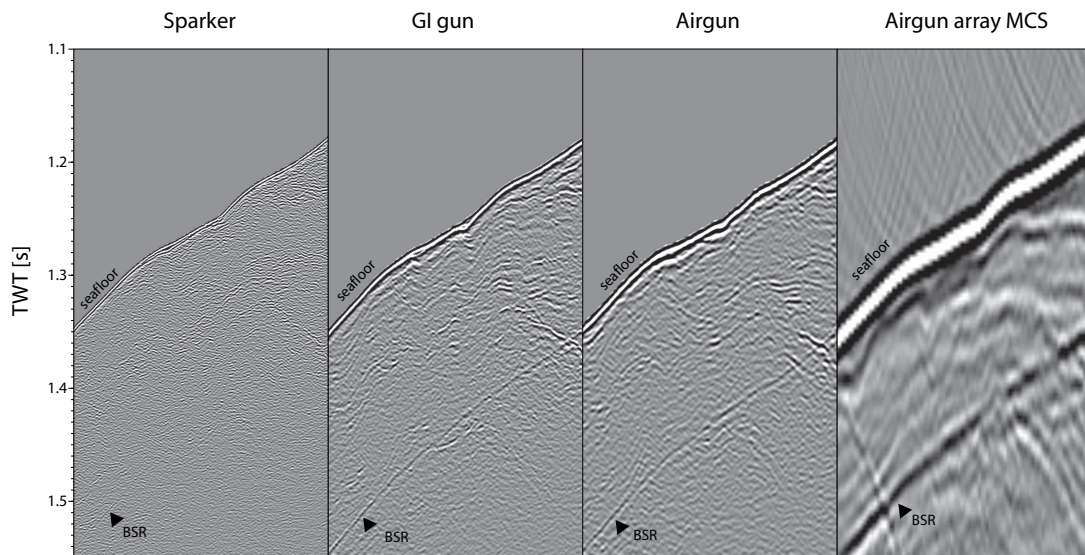


Figure 5.1: *Seismic images of the western flank of Southern Hydrate Ridge, showing four different frequency responses. The BSR shows maximum amplitudes at low frequencies (airgun array MCS , 30-70Hz, right panel) and minimum amplitudes at high frequencies (sparker , 150-300Hz, left panel). Intermediate frequencies (Gi-gun and airgun array, 80-180Hz) clearly image a continuous BSR.*

variations infers a decrease in the signals frequency pattern at the BSR compared to the seafloor. This effect cannot be observed in neither data. Therefore it is assumed that attenuation only plays a minor role in the observed amplitude variations. The variations are best explained by introducing a smoothed velocity gradient at the BSR instead of a sharp interface, as shown before in previous works (e.g. *Chapman et al., 2002*).

Chapman et al. (2002) restricted the analysis to a single negative gradient, where P-velocities drop from 1800 to 1550 m/s within a transition zone of 5 – 10 m, without considering a thin layer, which causes velocities to increase from low velocities to the original background velocity.

Various numerical models have been developed by other investigators to study the reflection behavior of thin beds. *Neidell and Poggiagliolmi (1977)* discussed the importance of seismic modeling in stratigraphic studies and the use of reflection amplitudes and waveforms in the quantitative analysis of stratigraphic reservoirs. Complex trace analysis has been studied by *Voogd and Rooijen (1983)* and *Robertson and Nogami (1984)* to evaluate resolution of thin beds. *Widess (1973)* determined the minimum thickness that can be resolved in the time domain as one quarter of the period of the dominant wavelength. He also discussed the response of a thin layer to a vertically incident seismic pulse, but he neglected the influence of internal multiples. *Koefoed and Voogd (1980)* showed that multiples are more significant for large reflection coefficients and provide limits to the linear response of thin layers. Dispersion of the reflected wave was determined by *Robertson and Nogami (1984)* for normal incidence on a wedge-shaped reflector. The analysis has often been limited to layers of sufficient thickness for the top and bottom reflected wavelets to be resolved. When the thickness is less than the tuning thickness (*Kallweit and Wood, 1982*), the two reflections are not resolvable in the time domain, and thickness information is encoded in the amplitude and shape of the reflected wavelet. The effect of a thin layer on reflecting amplitudes and AVO analysis, represented by a low-velocity wedge in the velocity model is investigated here. By analyzing the amplitude response of the BSR and the tuning effects at different frequencies for vertical incidence, the thickness of this thin layer is determined. The general effect on the amplitudes reflected from this thin layer for oblique angles is then analyzed qualitatively at the end of this chapter to verify the thickness estimation.

5.2 Thickness estimation

The varying amplitude responses of different frequencies are tested by forward modeling of synthetic vertical-incident traces. Hereby, the main interest is focused on varying the thickness of the low-velocity layer from 1 to 20 m. Different shapes and sizes of a

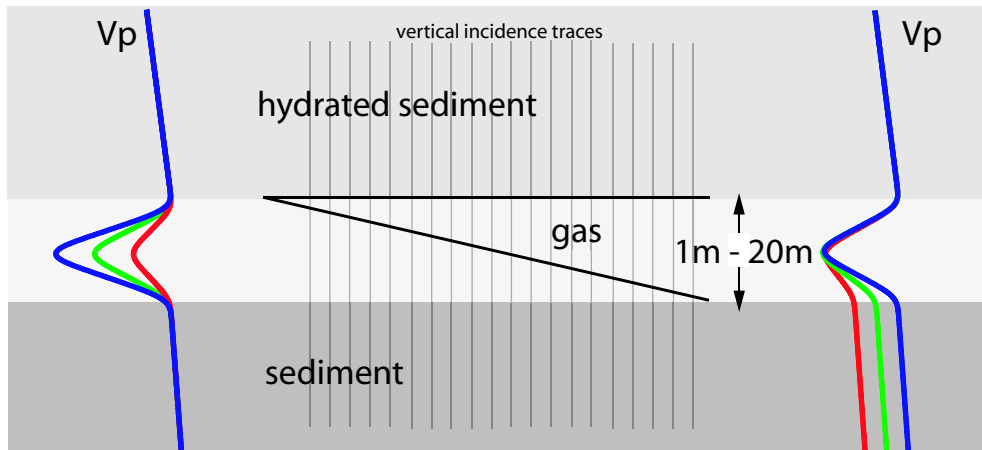


Figure 5.2: *Cartoon to describe the low velocity wedge model. Vertical-incidence synthetic traces are calculated for layer thicknesses of 1 to 20 meters. The shape and size of the wedge vary in different test runs.*

low-velocity wedge are modeled, representing the different amounts of gas saturation in the low-velocity layer (Fig. 5.2). By introducing a thin layer with a thickness smaller than the dominant wavelength of the incident signal, a single wavelet is reflected by interference from the top and the bottom of the gas layer. The amplitudes of the wavelet are influenced by the layer thickness and are in relation to the frequency of the signal. This relationship between layer thickness and frequency is used to compare different sources of the collected SCS data and to determine the thickness of the gas layer by calculating synthetic models.

The source signals for calculating the synthetic traces were Ricker-wavelets (*Ricker, 1945*) of 50, 100, 150, and 200 Hz representing the MCS-airgun, HYDGAS-airgun, GI-gun, and sparker, respectively. The term 'MCS-airgun' refers to the airgun-array used during the acquisition of line OR02 (*MacKay, 1995*), which is coincident with the airgun line during the HYDGAS cruise. The main frequency of the MCS-airgun array is about 50 Hz, compared to the HYDGAS-airgun of 100 Hz, GI-gun 150 Hz and sparker 200 - 400 Hz, respectively (compare Table 2.2). A 200 Hz Ricker-wavelet is used to simulate the sparker data. The primary sparker signal shows moderate interference with the receiver ghost signal and was recorded by the streamer as a wavelet with four half-cycles (compare Fig. 2.5). The amplitudes of the sparker data are picked in the frequency domain at 200 Hz.

5.2.1 Change in velocity

In a first run the effect of different amounts of gas in the low-velocity wedge is analyzed. For this purpose synthetic seismograms are computed for three models: a decrease from 1590 m/s to (1) 1480, (2) 1520, and (3) 1550 m/s, respectively.

The comparison of relative amplitudes of the collected SCS and MCS data requires additional modeling of the seafloor. In the analysis presented here, all reflection amplitudes are normalized by the amplitude of the seafloor reflection within this study. By investigating the relative amplitudes, it is accounted for possible inconsistencies in the source strength from shot to shot. The seafloor reflection coefficient is set to a value of 0.2. The resulting synthetic traces for the 100 Hz signal are displayed in Figure 5.4.

The picked relative amplitudes of the synthetic traces are plotted against the layer thickness in Figure 5.3. Two effects are observed: (1) The amplitudes vary relative to the layer thickness. As expected, the maximum amplitudes are observed at a layer thickness corresponding to the tuning thickness ($\approx \lambda/4 = 4m$) of the dominant wave-

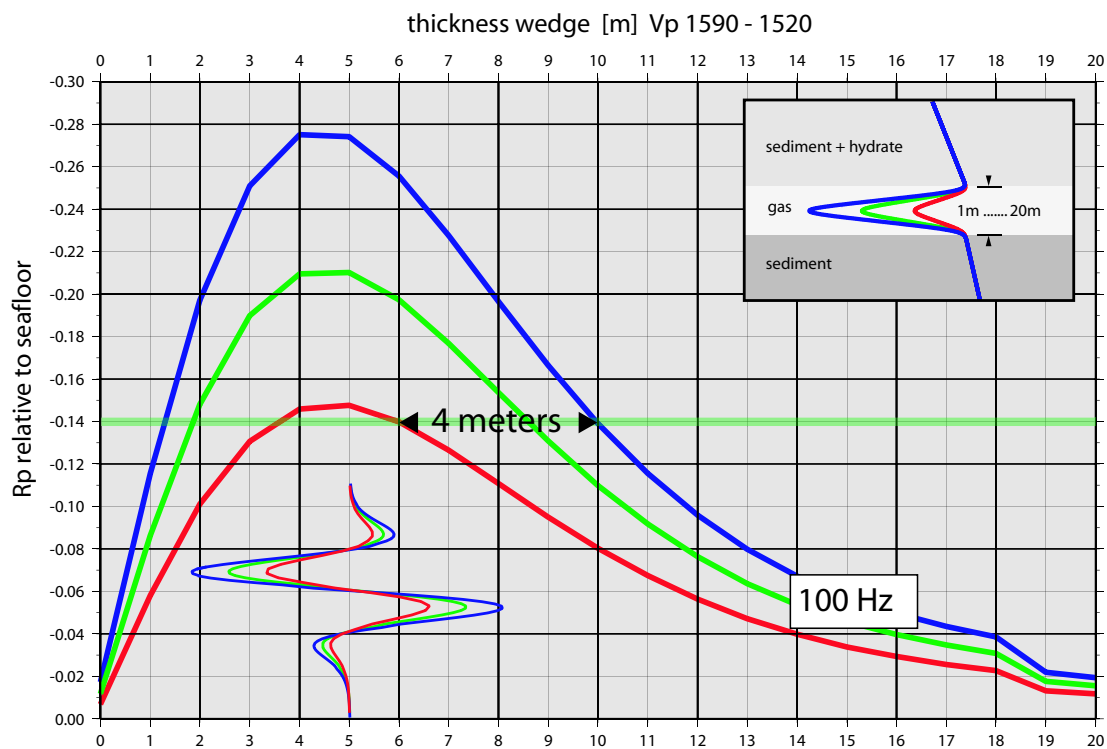


Figure 5.3: As the thickness of the gas layer increases (from left to right, 1-20 meters) the amplitudes of the BSR signal changes with a maximum value at 4 m thickness. The effect of varying gas concentrations, causing a change V_p is resulting in a average uncertainty within the thickness estimation of 4 meters.

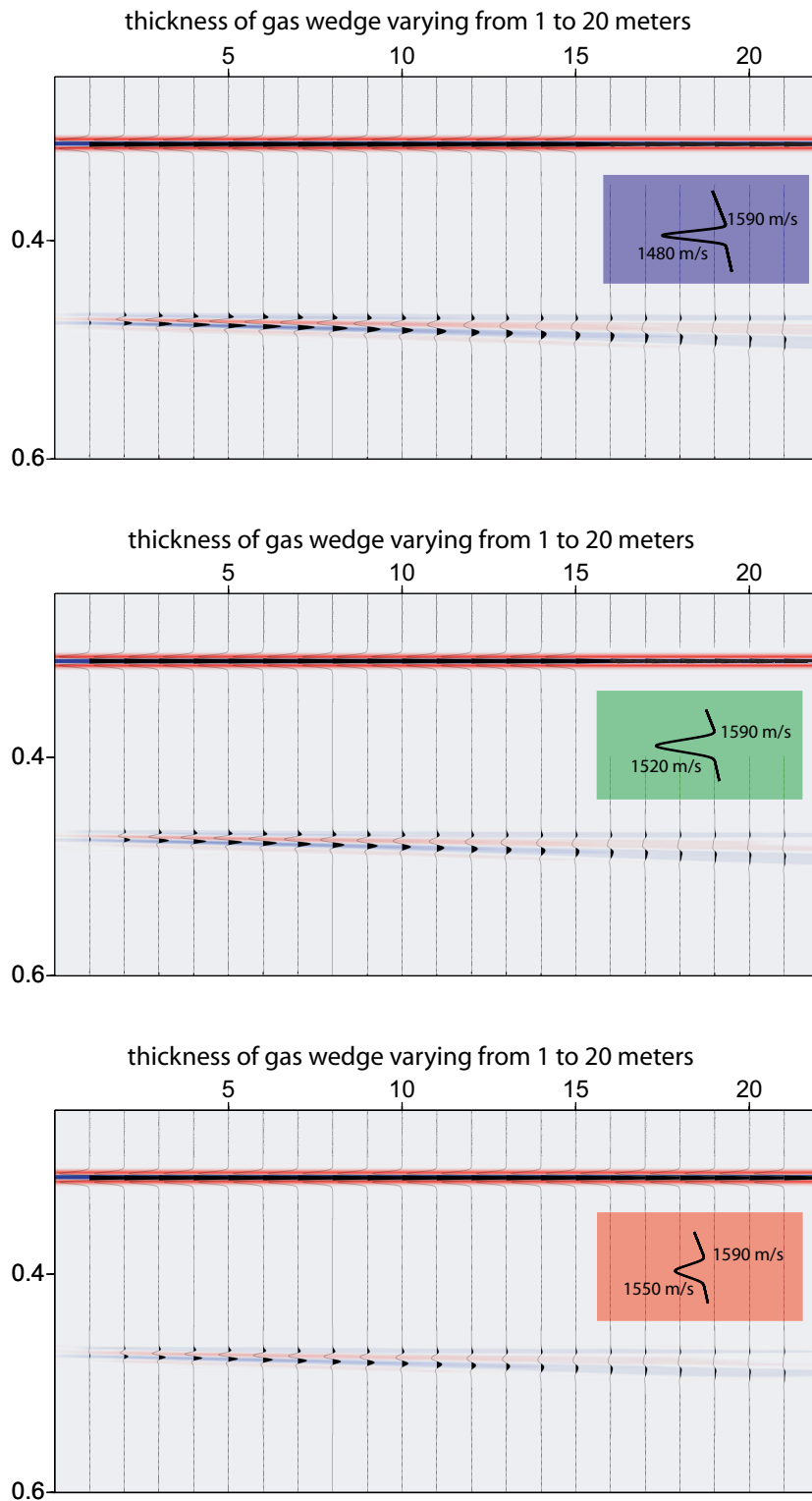


Figure 5.4: *Synthetic seismograms of the modeled gas wedge. As the thickness of the gas layer increases (from left to right, 1-20 meters) the shape and size (amplitude) of the BSR signal changes. Variable gas concentrations, modeled by changing the p-wave velocity, only effect the absolute amplitudes (compare with Fig. 5.3).*

length. After the tuning thickness is reached amplitudes decay with increasing layer thickness. The difference of a 50 Hz signal compared to a 150 Hz signal is illustrated in Figure 5.5. Maximum amplitudes are reached at a tuning width of 3 m and 9 m for 150 and 50 Hz, respectively. For a layer thickness of 8 m, the 50 Hz signal provides higher amplitudes than the 150 Hz signal, which is also observed in the real data sets: Low frequency sources (airguns) produce higher amplitudes than high frequency sources (sparker).

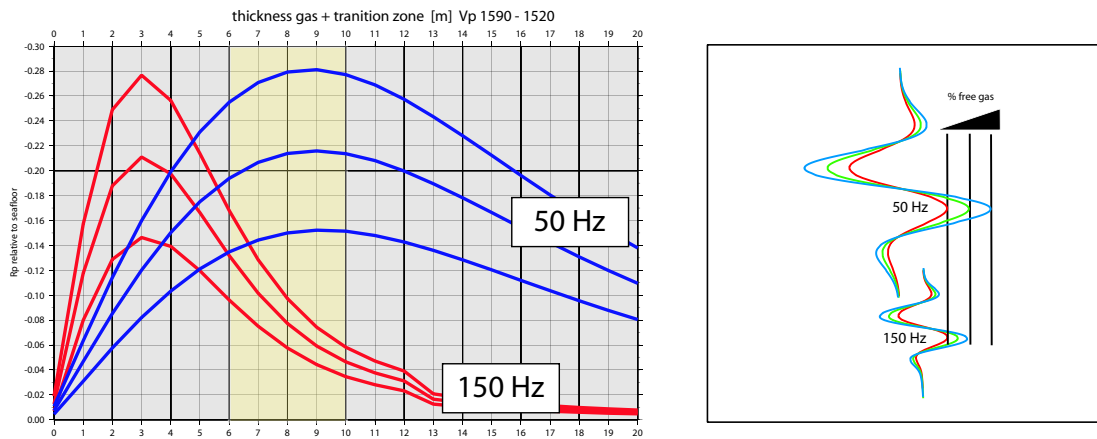


Figure 5.5: The amplitudes (left panel) are calculated for three cases of gas layers, containing different V_p velocities. The amplitudes show more variability for a 50-Hz signal than for a 150-Hz signal at an assumed thickness of 8 m (left, yellow shaded). A close-up of the reflection signals at a thickness of 8 m is displayed in the right panel to point out the amplitude variations.

(2) The amplitude variation as a function of P-wave velocity represents layers with different amounts of free gas (Fig. 5.3). Higher amplitudes are achieved when the P-wave velocity decreases in the wedge. For a constant layer thickness of 8 m, the amplitude variations of the 150 Hz signal are smaller than the amplitude variations of the 50 Hz signal. In contrast, when assuming a constant relative reflection amplitude, the effect of varying the P-wave velocity in the wedge, shows an uncertainty of 4 m in layer thickness (Fig. 5.3).

In conclusion, amplitude variations are observed, which are caused by the interference of signals reflected from the top and bottom of the wedge. This amplitude pattern varies with the amount of gas, represented by changing the P-wave velocities in the wedge.

5.2.2 Change in gradient

The effect of different velocity gradients in the upper and lower layer on the amplitudes is illustrated in Figure 5.6. Different velocity gradients are caused by gas hydrates in the sediment above the gas layer. A background non-hydrated velocity gradient is assumed for the layer below the low-velocity wedge. This reflects different velocities above and beneath the gas layer. Again, only the 100 Hz signal is displayed as an example for the synthetic results (Fig. 5.7). The velocity of the upper sediment layer is constant at 1590

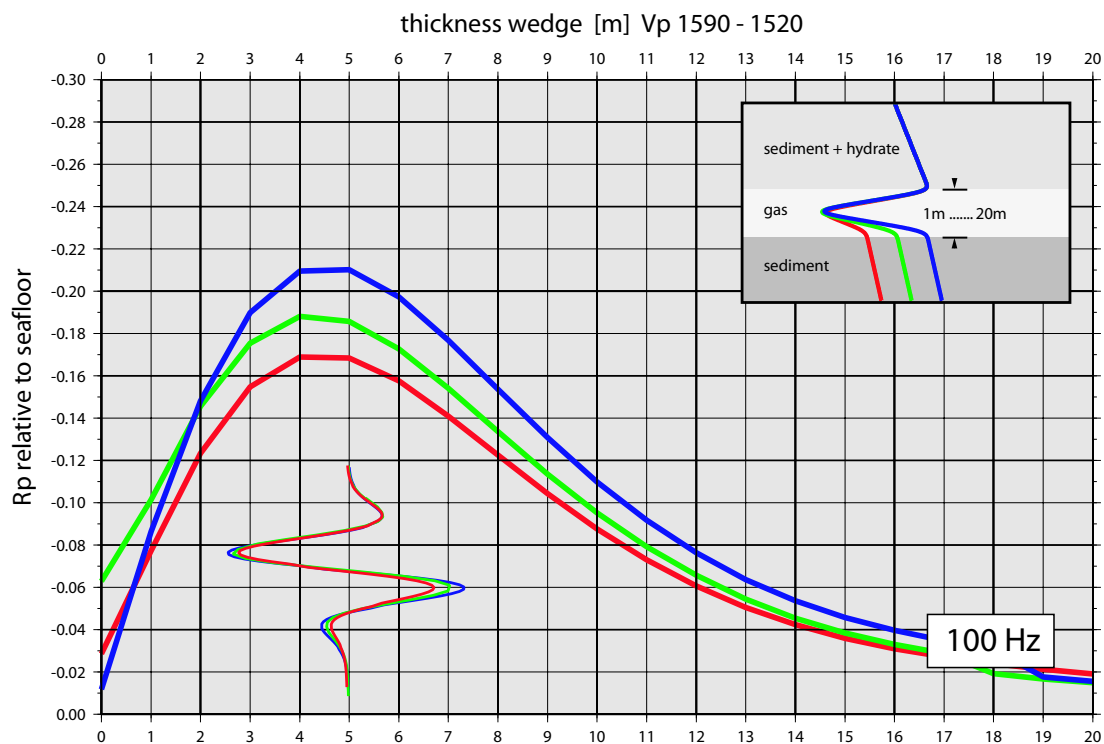


Figure 5.6: As the thickness of the gas layer increases (from left to right, 1-20 m) the amplitudes of the BSR signal change with a maximum value at 4 m thickness. The effect of different background velocity gradients is resulting in a phase change of the signal. The amplitudes for different background velocities are only minorly affected.

m/s, whereas the lower sediment layer varies while modeling different background non-hydrated velocity gradients. The effect of modifying the background velocity gradient on the reflecting wavelet, displayed in Figure 5.6, is mainly manifested in the phase of the reflecting signal. The absolute values of the varying amplitudes are less dominant than the effect of modifying the P-wave velocities in the wedge. In conclusion, different velocity gradients, due to hydrated sediment above the gas layer, mainly contribute to the phase shift of the reflecting signal, whereas the amount of gas in the low-velocity wedge has a greater influence on the reflecting amplitudes.

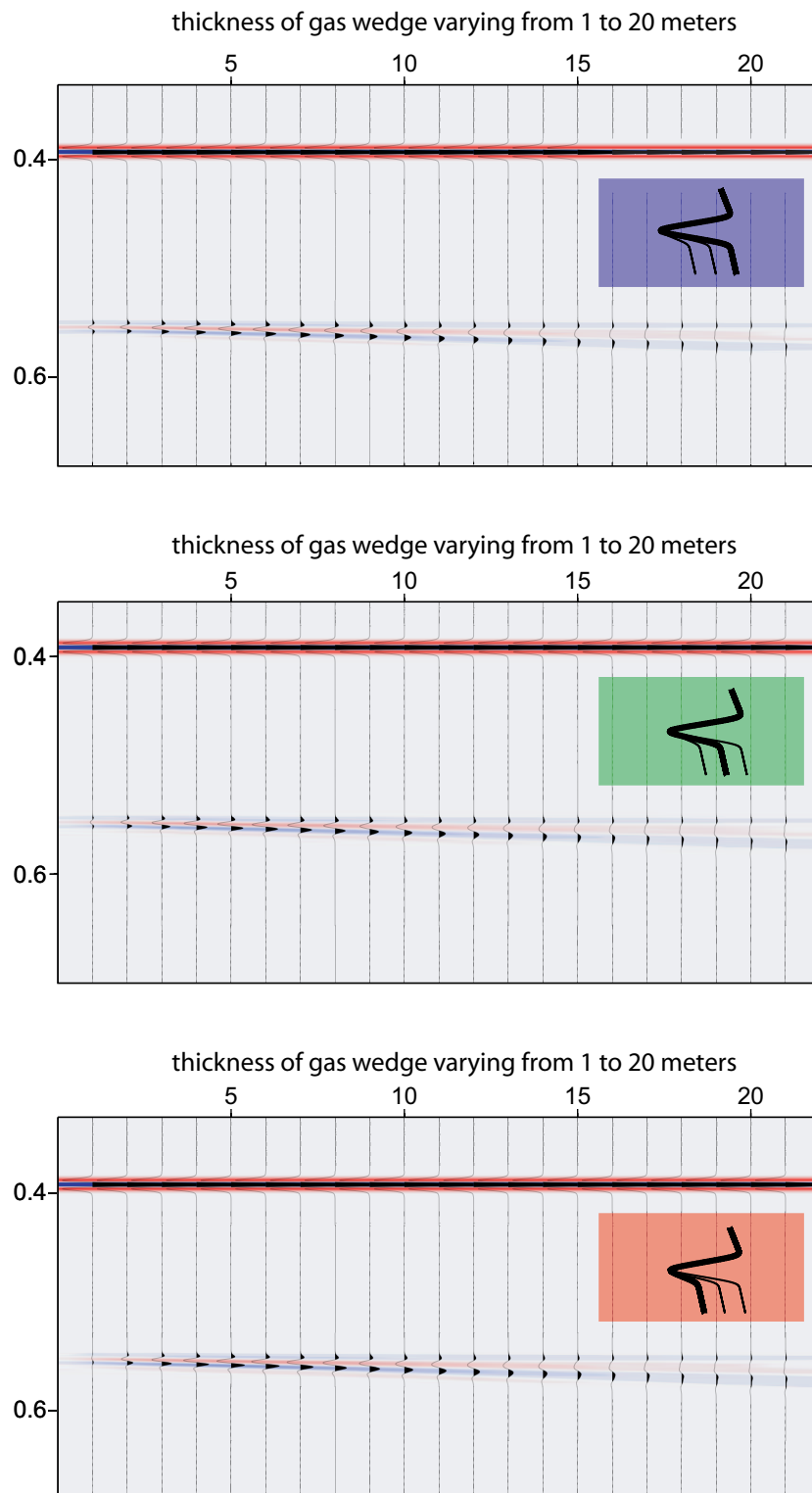


Figure 5.7: *Synthetic seismograms of the modeled gas wedge. As the thickness of the gas layer increases (from left to right, 1-20 m) the shape and size (amplitude) of the BSR signal changes. Variable background sediment velocities, mainly affect the phase of the BSR signal. This variation has less influence on the absolute amplitudes compared to changing the amount of free gas in this layer (Fig. 5.3).*

5.2.3 Thickness estimation

The results of the synthetic models are now compared with the real data. Therefore the amplitudes of the reflections of the seafloor and the BSR are picked to determine the relative reflection amplitudes. Amplitude picking is restricted to the western flank, because strong reflections are cross-cutting the BSR at the eastern flank of the ridge. Only picks of confidently identified phases are taken into account. Due to lateral variations, the amplitudes are picked along a ~ 2 km long segment of the BSR at the western flank. The normalized distribution of BSR amplitudes of the different sources used in this analysis are presented in Figure 5.8. The normalized distribution is plotted against the picked relative reflection amplitudes. The distribution of the picked amplitudes is required to derive the mean relative reflection amplitudes. The high-frequency streamer-data of the sparker signal does not resolve the BSR over the entire length. Consequently the number of picks is less than the number of picked amplitudes from the GI-gun data. The distribution is normalized (Fig. 5.8) for a better

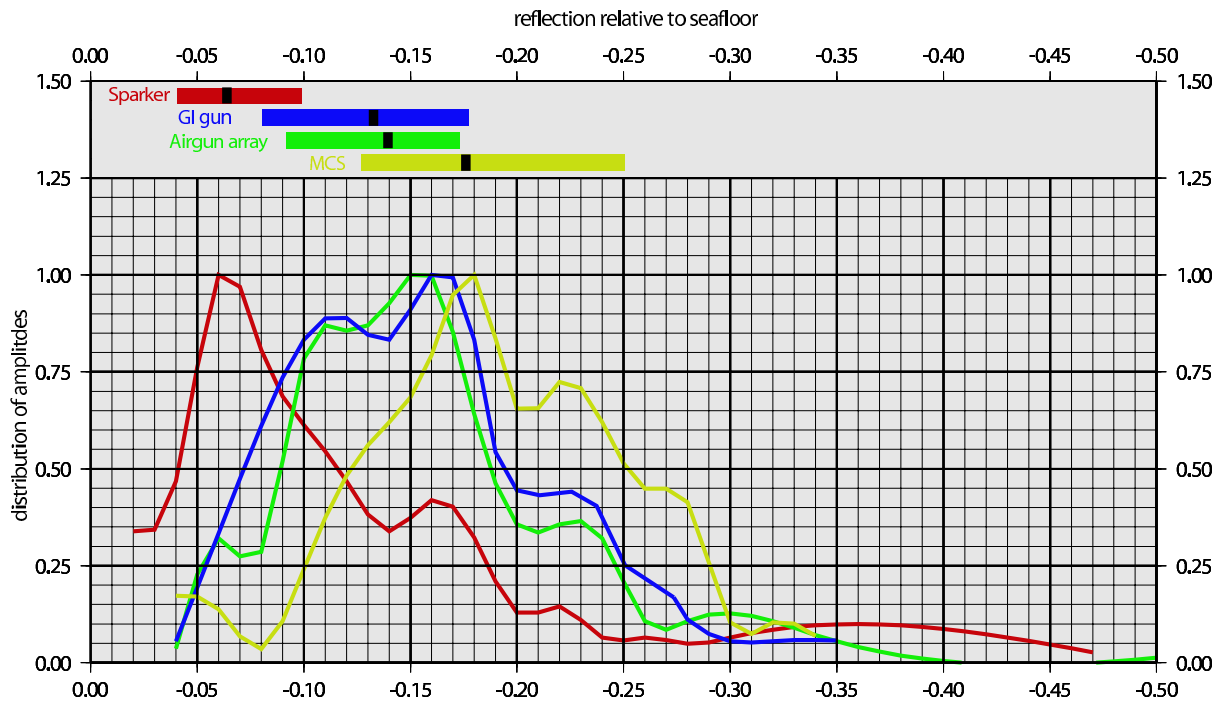


Figure 5.8: *Relative distribution of BSR amplitudes. The high frequency sparker data (red) reflect a weak BSR with an average reflection value below 0.1. The intermediate frequencies of the airgun array and Gi-gun (green and blue) share the same mean reflection value between 0.1 and 0.18. Maximum amplitudes in the range of 0.13 and 0.25 are only reached in the low frequency data of the MCS airgun array (yellow).*

comparison. The low frequency MCS-airgun (yellow) reveals the highest amplitudes. They vary between -0.13 and -0.25. For a constant seafloor reflection coefficient of 0.2 this computes to an absolute reflection coefficient at the BSR in the range of -0.026 and -0.05. The amplitude values of all sources are presented in Table 5.1.

	Sparker	GI-Gun	HYDGAS-Airgun	MCS-Airgun
Frequency	200 Hz	150 Hz	100 Hz	50 Hz
Rel. amplitude	-0.04 to -0.1	-0.08 to -0.18	-0.09 to -0.17	-0.13 to -0.25
Abs. amplitude	-0.008 to -0.02	-0.016 to -0.036	-0.018 to -0.034	-0.026 to -0.05
Reference	-0.065	-0.135	-0.134	-0.177

Table 5.1: *Relative and absolute BSR reflection amplitudes of the sources used in this study. The reference value is obtained by picking amplitudes of a single location.*

Because the amplitudes were averaged over a 2 km long segment, a reference value is given, marked by the black bar in Figure 5.8. This reference value was picked at a single location for all sources. The relative reflection amplitudes are now compared to the theoretical amplitude trends, provided by the synthetic model results (Figs. 5.10 and 5.9).

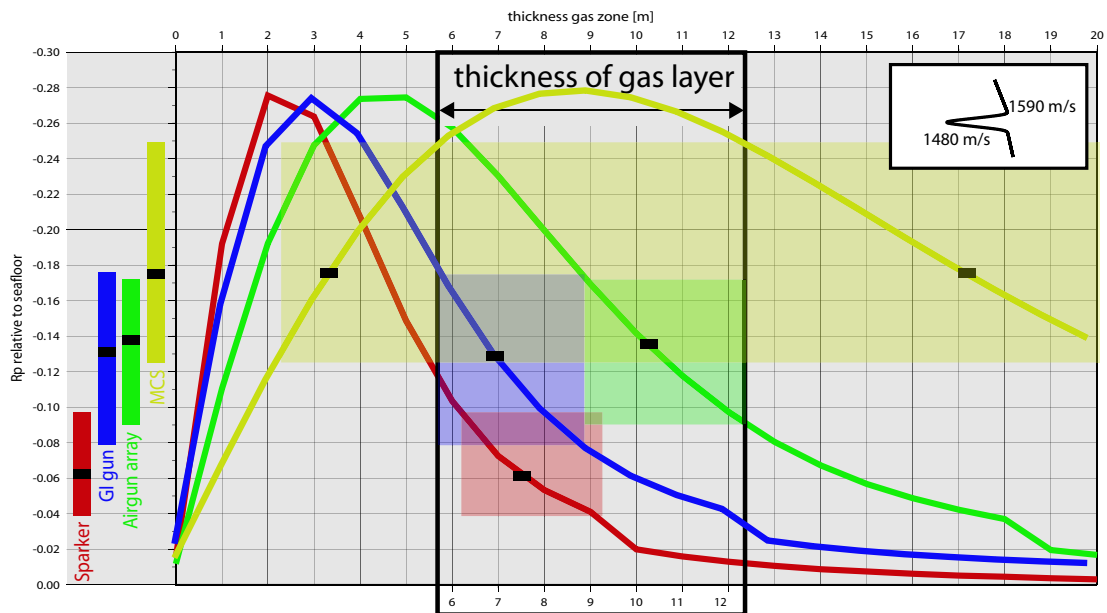


Figure 5.9: *Relative amplitudes of the BSR for each source is plotted for a wedge model with V_p decreasing from 1590 m/s to 1480 m/s. Depending on the signal wavelength, the reflection amplitudes vary when changing the thickness of the gas layer (colored curves). Each source frequency results in different maximum (tuned) amplitudes. Shaded zones mark the area, where real data amplitudes (upper panel) coincide with model curves. The averaged thickness of the gas layer (box) ranges from 6 to 12 m.*

The theoretical curves in Figure 5.9 represent the results of a low-velocity wedge of minimum P-wave velocities of 1480 m/s. On the left side of Figure 5.10, the amplitude distribution of the real data set is plotted. In the main frame, the relative reflection amplitudes are plotted against the layer thickness of the low-velocity layer. The amplitude responses of 50, 100, 150, and 200 Hz are color-coded as yellow, green, blue and red line, respectively. Each curve has its maximum amplitude corresponding to its tuning thickness. By comparing the amplitudes of the real data set with those of the synthetic models, the respective color-coded bars on the left (real data) have to be extended into the main frame until they overlap with the respective color-coded curve (synthetic). The overlapping region, marked by the shaded areas, then defines the layer thickness of the gas layer. The resulting layer thickness of the thin gas layer, averaged over the 2 km segment is determined to 6 and 12 m for this model. However, the reference amplitudes for a single location (black bar in Fig. 5.9) result in a large thickness-range and the theoretical amplitudes are in general higher than the average amplitudes of the real data. Therefore, the preferred model for the comparison with the observed reflection amplitudes is a velocity distribution of 1590 m/s above the gas

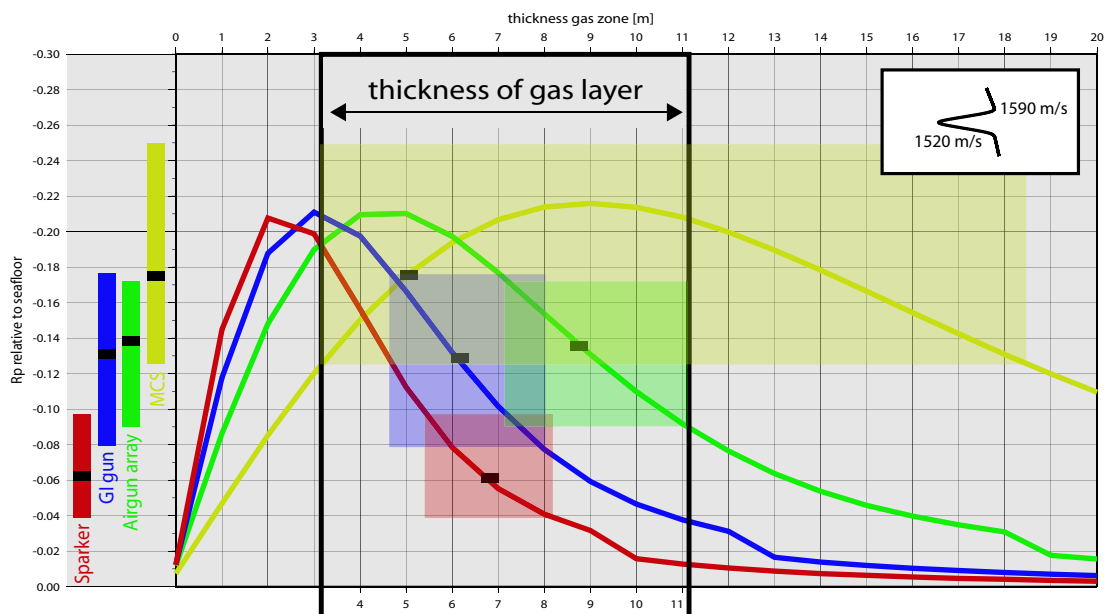


Figure 5.10: *Relative amplitudes of the BSR for each source is plotted for a wedge model with V_p decreasing from 1590 m/s to 1520 m/s. Depending on the signal wavelength, the reflection amplitudes vary when changing the thickness of the gas layer (colored curves). Each source frequency results in different maximum (tuned) amplitudes. Shaded zones mark the area, where real data amplitudes (upper panel) coincide with model curves. The averaged thickness of the gas layer (box) ranges from 3 to 11 m.*

wedge reaching minimum velocities of 1520 m/s in the gas wedge (Fig. 5.10). The model used here has a slightly smaller velocity 'non-hydrated' gradient, resulting in a P-wave velocity of 1560 m/s for the lower sediment layer. The thickness for the gas layer for this model is determined to 3 - 11 m. The thickness estimation of the single location (black reference bar in Fig. 5.10) ranges from 4 to 9 m. Higher velocities in the wedge and consequently lower velocity contrasts at the upper interface, do not result in reflection amplitudes in the range of the observed amplitudes in the data set.

5.2.4 Summary

Three distinct amplitude variations are observed at the BSR: (1) high frequencies generate a weak BSR amplitude compared to high amplitudes at low frequencies, (2) amplitude variations along the BSR are higher at low frequencies, and (3) a phase shift in the BSR signal. The phase shift in the BSR signal is a clear indicator for a signal interference at the BSR interface. Synthetic seismic modeling of thin gas layers at different frequencies result in amplitude variations, due to tuning effects, which are then compared to the the amplitude variations of the collected data. This comparison results in layer thickness of 3 to 11 m along a 2 km segment across the western flank of the southern ridge. Additionally, these models predict a low P-wave velocity of about 1520 m/s for the gas layer, overlain by a sediment layer with a P-wave velocity of 1590 m/s. Higher P-wave velocities for the gas layer result in low amplitude contrasts, which are not observed in the real data set. Lower P-wave velocities, representing higher amounts of gas, result in a shift of the layer thickness to larger thicknesses. In contrast, the thickness is limited by the results of the velocity analysis. In conclusion, a model with low-hydrated sediments with a P-wave velocity of 1590 m/s above a thin gas layer, ranging between 3 and 11 m in width, with velocities of around 1520 m/s are predicted along this 2 km BSR segment. How this thin gas layer effects the AVO analysis is presented in the next section.

5.3 Thin beds and AVO

5.3.1 Introduction

Studies show that the AVO response of a thin layer depends upon the thickness of the layer (*Almoghrabi and Lange, 1986*) and may differ significantly from the AVO response of a simple interface. *Juhlin and Young (1993)* conclude that the effect of a low-velocity thin layer is less than that of a high-velocity thin layer with a comparable simple interface AVO response. They also conclude that this effect is valid for low-impedance contrasts. When the impedance contrast is high, the energy of P-wave multiples and converted shear-waves must be included (*Juhlin and Young, 1993*).

5.3.2 Thin bed analysis

The BSR amplitudes in the MCS data decrease with increasing offsets, whereas they remain constant in the GI-gun data of the OBH (lower two panels of Fig. 5.11). In fact, amplitudes in the OBH data seem to be slightly increasing with offset. For comparison the seafloor reflection amplitudes were picked and plotted next to the BSR amplitudes in the upper two panels of Figure 5.11. Note, that the horizontal offset-scale of the middle

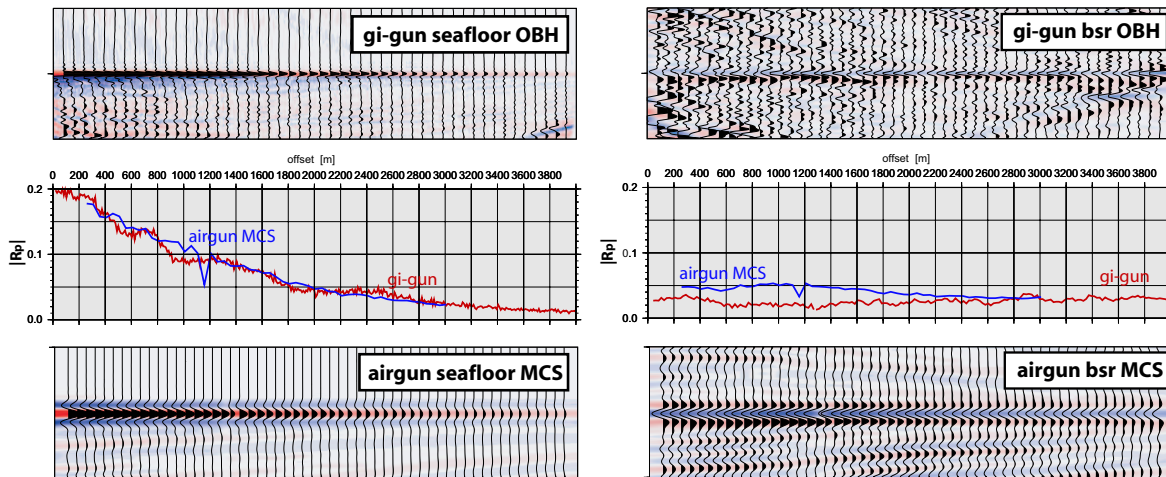


Figure 5.11: Comparison of real data BSR and seafloor reflection signatures. The upper two panels show recordings of an OBH, seafloor reflection (left) and BSR (right). The OBH data hold high frequencies (150 Hz) compared to reflections of the low frequency MSC airgun array (50Hz). The MCS data are displayed in the lower two panels, seafloor reflection (left) and BSR (right). The picked amplitudes (middle panel) show the different amplitude trends at the BSR. The MCS-airgun signal is decreasing in amplitude with larger offsets (blue), while the GI-gun amplitudes (red) show a slight positive trend.

panels is not identical with the offset scales in the seismic panels. Due to the different receiver geometry of the streamer and the OBH, the offsets of the MCS data were correlated to those of the OBH data. The OBH used for this analysis is positioned 200 m above the seafloor. Calculated geometrical spreading corrections show no significant effect on the relative amplitudes. The amplitudes of the seafloor in both data sets are calibrated to a reflection coefficient of 0.2. Seafloor amplitudes of both data sets show a similar negative trend, displayed in the middle/left panel of Figure 5.11. By comparing the BSR amplitudes of both data sets, a change in trend is observed. Amplitudes in the MCS data are decreasing with offset in contrast to a constant amplitude trend in the OBH data. Although the difference seems to be relatively small, they could have been generated by a frequency-dependent AVO behavior of the thin gas layer. The MCS data was shot with a 50 Hz airgun compared to the 150 Hz Gi-gun data of the OBH. Synthetic acoustic models are analyzed with regard of AVO effects to investigate the frequency-dependent behavior. The same models used before in the frequency analysis are now calculated for an offset range from 0 to 2000 m. Different velocity models are calculated with varying thickness of the low-velocity layer, similar to the frequency analysis where only the vertical-incidence case was investigated. The computed amplitudes are displayed in Figure 5.12. Three distinct AVO-trends relate to the different thicknesses of the gas layer (red, green and blue AVO-curves, Fig. 5.12). Figure 5.13 shows the response of both frequencies for near-vertical incidence in relation to the changing thickness. The curves in the two panels of Figure 5.12 show the AVO responses of the different layer thicknesses. The blue curves mark the AVO-trend before the tuning thicknesses are reached, 4 m (150 Hz) and 9 m (50 Hz), respectively. The AVO-curve steepens (more curvature), when the tuning thickness is reached, but the zero-offset amplitudes remain unchanged (green curves). After the tuning thicknesses are passed, zero-offset amplitudes decrease again, but with a steeper AVO-trend. Hence, for one given vertical-incidence reflection coefficient two different AVO-trends can be expected. This trend is controlled by the relation of the layer thickness and the dominant frequency. The upper panel of Figure 5.12 shows a 150 Hz wavelet, which is used to calculate the AVO response, representing the GI-gun signal. The AVO trend starts to change at a layer thickness of ~ 4 -6 m. In contrast, the 50 Hz signal, representing the MCS-airgun, reproduces a change in the AVO trend at ~ 9 -12 m. Thus, assuming a layer thickness of 8 m, two different trends can be expected for the GI-gun and MCS-airgun signal. This analysis supports the suggested model of a thin layer. The layer thickness of 8 m fits the result of the frequency analysis for vertical incidence, where a layer thickness of between 3 and 11 m was determined.

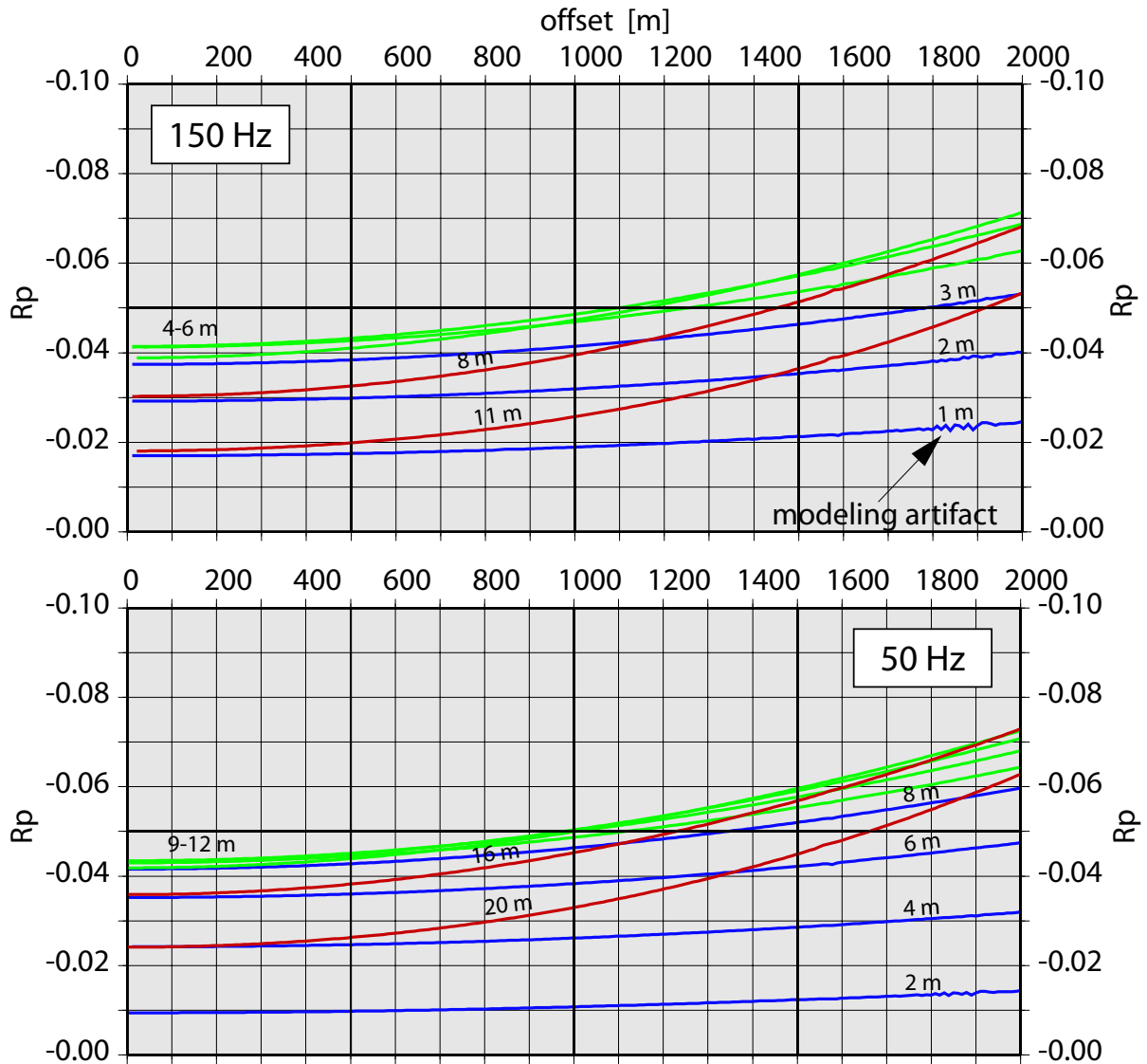


Figure 5.12: AVO trend, picked from synthetic acoustic modeling. The upper panel shows the response of a simulated GI-gun (150Hz) compared to a 50 Hz signal like the airgun in the lower panel. Blue curves mark the amplitude trend before reaching the tuning thickness of 4 m for 150Hz and 9 m for 50 Hz, respectively. Green curves display amplitudes within the tuning range. Note the changing trend as the thickness of the gas layer is reaching the tuning thickness. Red curves represent amplitudes of layers which exceed the tuning-width. The gi-gun amplitudes of the real data follow the red curves, whereas the low frequency MCS data show a less pronounced trend (blue curves).

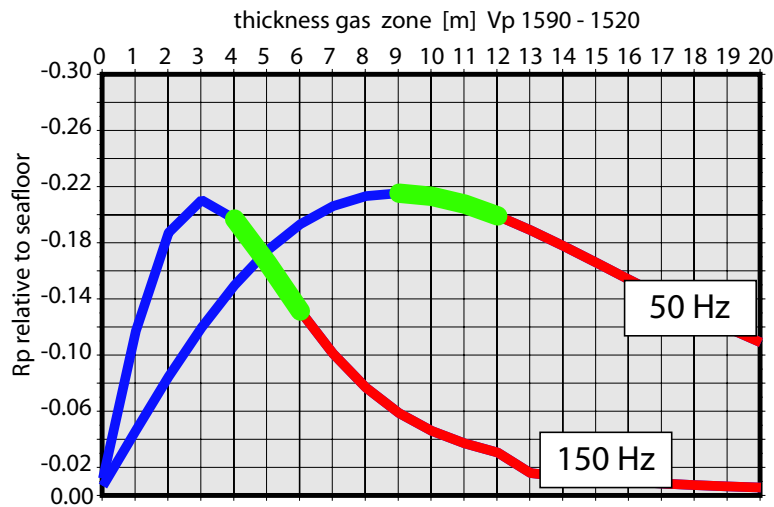


Figure 5.13: Amplitude response of the 50 and 150 Hz signal for the vertical incidence case at different layer thicknesses.

5.4 Conclusion

The amplitude variations of the BSR are caused by tuning effects at different frequencies of a thin gas layer below the BSR. Synthetic modeling of zero-offset traces are compared to the different frequency response of the collected data. The comparison of the amplitudes of the modeled and collected data result in an average thickness of 8 m for the thin gas layer. The effect of this thin layer on AVO investigation is most apparent at low frequencies (50 Hz). A change in the general AVO-trend is observed at a change of layers below and above the tuning thickness, depending on the signal frequency, whereas the absolute amplitudes are mainly controlled by the vertical-incidence interference. Thus the tuning effects of a thin layer result in different AVO-trends, depending on the signal frequency. When applying a standard AVO analysis on a thin layer, this effect has to be considered and additional information on layer thickness and frequency content is needed to calibrate the amplitudes at zero-offset.

In this study, the amplitudes of the collected data at different frequencies correlate with a thin gas layer of about 8 m below the BSR, when considering vertical-incidence reflections as well as the analysis of the general AVO trend.

6 ODP Leg 204 & Interpretation

6.1 Introduction

Two years after the HYDGAS cruise in 2000, a total of nine sites were cored and logged during ODP Leg 204 at Southern Hydrate Ridge (Fig. 6.1) to determine the distribution and concentration of gas hydrates in an accretionary ridge and adjacent slope basin, to investigate the mechanisms that transport methane and other gases into the GHSZ, and to obtain constraints on physical properties of gas hydrates in situ (Tréhu *et al.*, 2003).

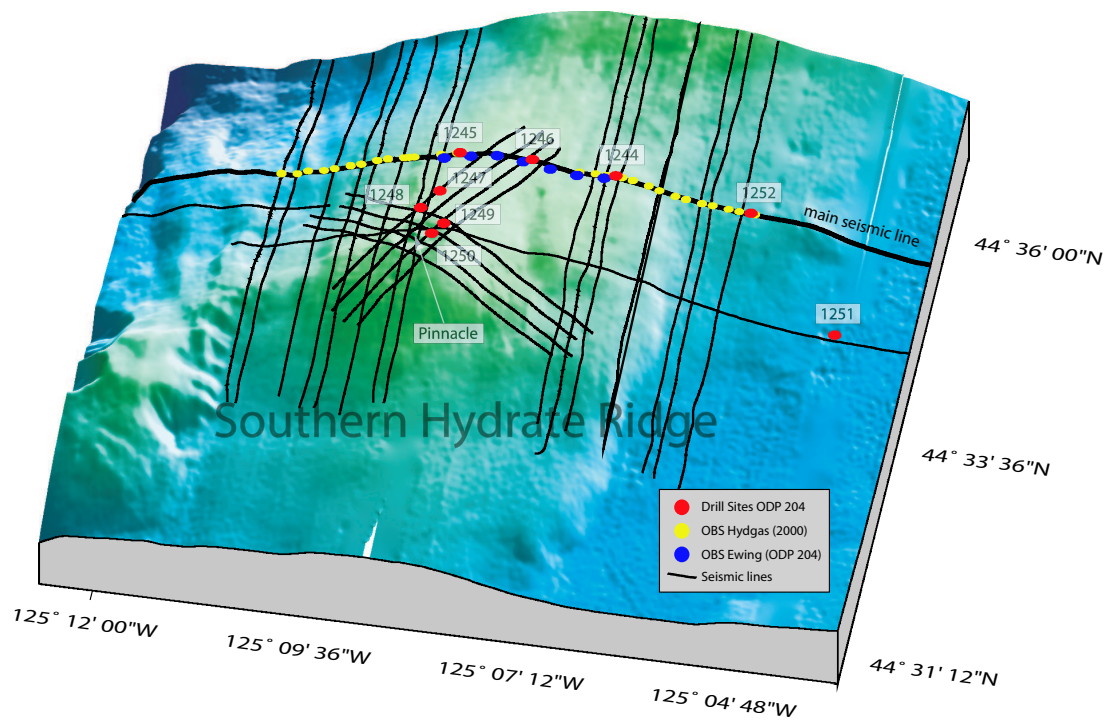


Figure 6.1: 3-D bathymetry of Southern Hydrate Ridge. Ocean bottom instruments were deployed during HYDGAS in 2000 (yellow) and during ODP Leg 204 in 2002 (blue) along the main seismic line, P173 and OR02. ODP Drill Sites are marked in red.

The northern summit was drill site location of Ocean Drilling Program Leg 146 in 1992 (*Westbrook et al.*, 1994). At the time of the HYDGAS survey in 2000, advanced plans for drilling the southern summit existed and Site proposals were known. The seismic experiments at the southern ridge were designed to combine seismic work with the results of the planned ODP leg (Fig. 6.1).

Apart from the velocity analysis of Chapter 3, investigations were carried out before ODP Leg 204 and did not include results obtained by ODP drilling. The OBS data collected within the scope of ODP leg 204 was implemented in the velocity inversion. The primary experiment during this cruise was a two-ship vertical seismic (VSP) experiment conducted with R/V Ewing and the drill ship JOIDES Resolution (*Bangs and Pecher*, 2002). As a second experiment seismic data with OBS were acquired. One part of these experiments was the deployment of seven OBS along a seismic line coincident with line p173 and OR02 (*MacKay*, 1995). The deployment of these OBS was especially designed to complement the HYDGAS deployment (Fig. 6.1).

In this chapter the seismic results, presented in this thesis, are compared to the results of ODP Leg 204 and a combined analysis with the integrated log information is carried out. The following general results were obtained from seismic data collected before ODP leg 204:

- The observations in the velocity model predict P-wave velocities, which gradually increase from 1520 m/s at the seafloor to 1580 m/s at the BSR. This infers relatively low concentrations of gas hydrates. This result was compared to other velocity studies and an estimate of around 1% for the gas hydrate concentration was determined. An area of locally higher P-wave velocities at the western slope of the ridge was first interpreted as a possible indication of locally higher concentration of gas hydrates. This was revised by multi channel seismic (MCS) data observations. It was assumed that the high velocities were likely due to a sediment sequence of higher velocities cross-cutting the BSR and not caused by higher amounts of gas hydrates within this region.
- In general, the depth-focusing analyses during the migration process of the MCS data did not resolve a layer of reduced P-wave velocities below the BSR. However, a relatively thin layer of low P-wave velocities, caused by the presence of free gas, could not be ruled out, as a result of the limited vertical resolution.
- Frequency dependent amplitude investigations suggested the presence of a thin low-velocity layer below the BSR, presumably caused by low concentrations of free gas. The thickness of this gas-layer was assumed to be between 3 and 11 meters, averaged over the western slope of the ridge.

In the following sections primary results of ODP Leg 204 are discussed and acoustic

sonic logs as well as bore hole information is presented. The quantifications of gas hydrate concentrations and free gas saturation derived from the various methods, described by *Tréhu et al. (2003)*, are all obtained from the works of the Scientific Party of ODP Leg 204 (*Tréhu et al., 2003*).

6.2 Previous studies

One of the surprising results of the inverted velocity model is that it shows 'typical' sediment velocities between the seafloor and the bottom simulating reflector (BSR). Here, 'typical velocities' is referred to the absence of an expected increase of the P-wave velocity, due to hydrate formation. Because methane hydrate has a P-wave velocity of 3.3 km/s (*Sloan, 1998*), it generally increases the lower P-wave velocity of sediment without gas hydrates. This general increase of P-wave velocities, linked to hydrate formation, was observed at Blake Ridge by *Hornbach et al. (2003)* (Fig. 6.2). P-wave velocities related to gas hydrates are above 1600 m/s.

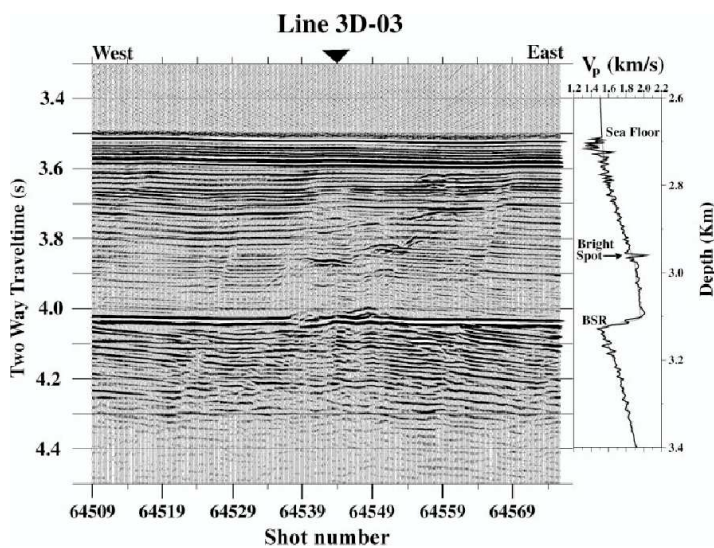


Figure 6.2: *Small migrated section showing the typical characteristics of hydrate bearing sediments: prominent BSR at ~ 4 s TWT, gradual velocity-increase (right panel) down to the BSR depth and amplitude blanking due to hydrate formation, drastic P-wave velocity decrease beneath the BSR and strong reflectivity, due to the presence of free gas, from *Hornbach et al. (2003)*.*

Tinivella and Carcione (2001) estimated the gas-hydrate concentration and free-gas saturation from log and seismic data at Blake Ridge. The models used in this estimate to obtain the wave velocities of sediments saturated with water and gas hydrate were developed by *Carcione and Tinivella (2000)*. The wave velocities of a porous medium saturated with a mixture of water and free gas were derived from the theory of *Tinivella and Carcione (1990)*. This model assumes that the free gas is uniformly distributed in the pore space. *Tinivella and Carcione (2001)* introduced a second approach to model a patchy saturation of free gas (*Dvorkin et al., 1999*).

The theoretical P-wave velocity of water-saturated sediments (broken line) and the VSP wave velocity (solid line) are compared in Figure 6.3. Due to the consolidation

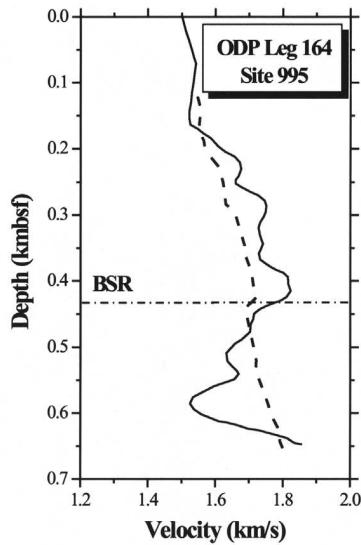


Figure 6.3: *Theoretical P-wave velocity of water-saturated sediments (broke line) and VSP wave velocity (solid line) at ODP Leg 164, site 995, Blake Ridge, from Tinivella and Carcione (2001).*

associated with the presence of hydrate, the velocity anomaly of hydrated sediments can be used to estimate the presence of gas hydrates. The anomaly caused by a relative decrease of the P-wave velocity was used to estimate the concentration of free gas beneath the BSR. *Tinivella and Carcione (2001)* estimated the amount of gas hydrate concentration relative to the P-wave velocities (Fig. 6.4).

By comparing the velocity anomalies with the hydrate concentration, a change of ~ 100

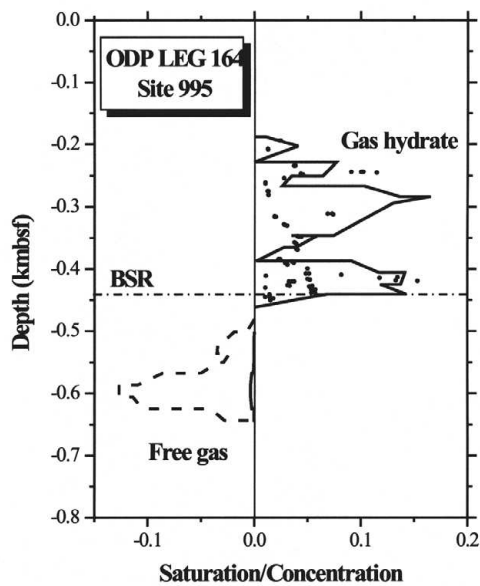


Figure 6.4: *Theoretical concentrations of gas hydrate and free gas (solid line, positive and negative values, respectively) compared to the corresponding experimental values (dots). The broken line represents the theoretical free-gas profile obtained with the patchy-saturation model. The experimental gas-hydrate concentration was obtained from measurements of the chlorinity content (ODP, Leg 164, Site 995, Blake Ridge), from Tinivella and Carcione (2001).*

m/s would result in $\sim 10\%$ hydrate concentration, or ~ 20 m/s in $\sim 2\%$, respectively. The experimental values (dots) were obtained from measurements of the chlorinity content (ODP Leg164, Site 995, Blake Ridge). These values show slightly lower concentrations of gas hydrates. Similar results were obtained from analyses (*Tinivella and Carcione, 2001*) at the Cascadia accretionary-wedge sediments offshore Vancouver, where even higher P-wave anomalies are observed.

Tinivella and Carcione (2001) predicted the saturation of free gas to be 10% for the patchy model and nearly 1% for the model, for which the gas phase is uniformly distributed in the pore space. These values correspond to a P-wave velocity anomaly of about -200 m/s. The absolute P-wave velocity thereby was ~ 1580 m/s (Fig. 6.3). The difference of an assumed patchy-saturation gas model and a uniform-saturation model is presented in Figure 6.5.

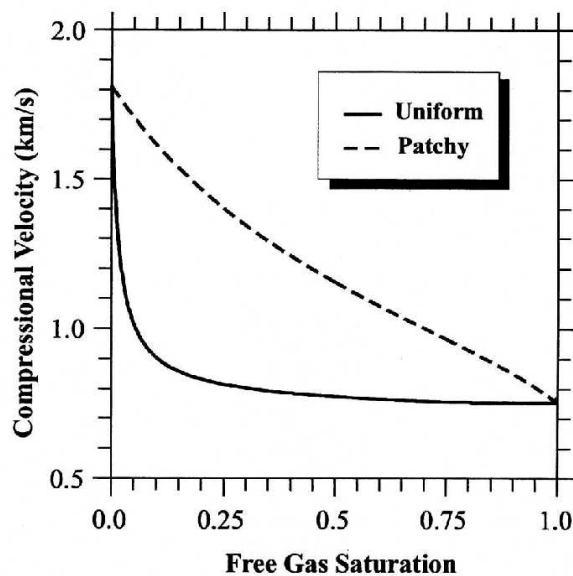


Figure 6.5: Difference between the P-wave velocities calculated with the patchy-saturation model (broken line) and uniform-saturation model (solid line) versus free-gas saturation, from *Tinivella and Carcione (2001)*.

Pecher and Holbrook (2000) concluded that a lateral increase in velocity of about 50 m/s corresponds to a lateral increase in hydrate saturation from 2% to 7% of pore space. This mainly resulted from a very uniform sediment strata at Blake Ridge. In a less uniform environment, (e.g. an accretionary margin), a change of V_p by about 50 m/s would likely be indistinguishable from lateral sediment variations.

Compared velocities for example at a BSR offshore Peru (*Minshull et al., 1994; Pecher et al., 1996*) suggest velocities of far greater than 1600 m/s (Fig. 6.6).

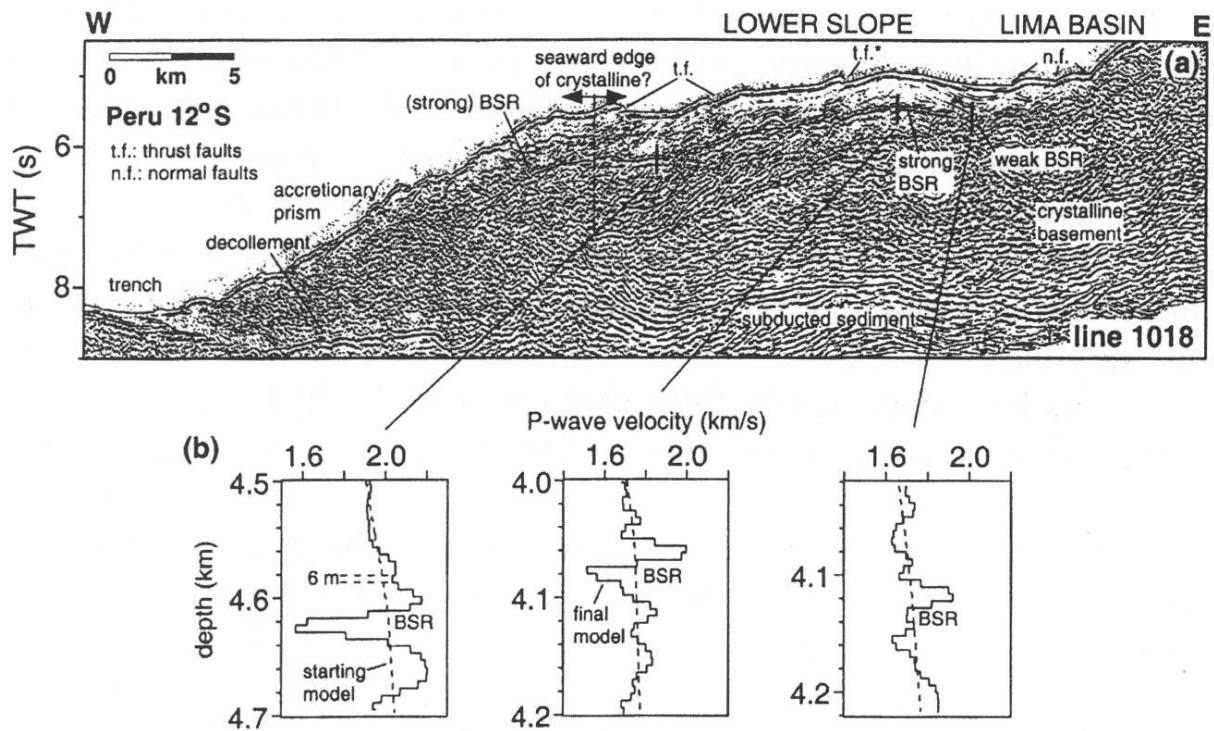


Figure 6.6: *BSR off Peru. Structural interpretation according to von Huene et al. (1996) Velocity depth profiles from waveform inversion across the BSR Minshull et al. (1994); Pecher et al. (1996), from Pecher and Holbrook (2000).*

The quantification of the gas hydrate saturation in this study is based on qualitative comparisons to these studies. The velocities obtained from the travelt ime-inversion are in general below 1600 m/s (Fig. 6.7). Average P-velocities at the BSR are roughly 1580 m/s. The comparison with these P-wave studies results in an estimation of about 1% gas-hydrate within the pore space over the entire GHSZ along profile p173.

Since the travelt ime inversion only accounted for the BSR reflection, the resulting velocity model represents the average velocity gradient within the GHSZ. Small scale changes of the P-wave velocity were not resolved during the inversion process.

6.3 The gas hydrate stability zone

Along profile p173 three Sites were drilled during ODP 204 (Fig. 6.7). Two of these Sites, 1244 and 1245, provided acoustic sonic log measurements. The Conventional Wireline Logging (CWL) sonic logs of Site 1244 (Fig. 6.8) and Site 1245 (Fig. 6.9) during ODP 204 confirm the velocities obtained from the seismic investigations. Additional logging was performed during ODP 204, using the P-wave logger of the 'Multisensor Track' and the 'Hamilton Frame' to obtain P-wave velocities of the upper 10 meters (illustrated as light blue curve in Figs. 6.8 and 6.9). Both logging systems are based on transmitting a 500-Hz pulse through the core and the split core, respectively. Green and blue logs represent the two passes of the conventional wireline logging (CWL). Site 1245 had "the worst hole conditions" and the second pass had to be reprocessed (G.

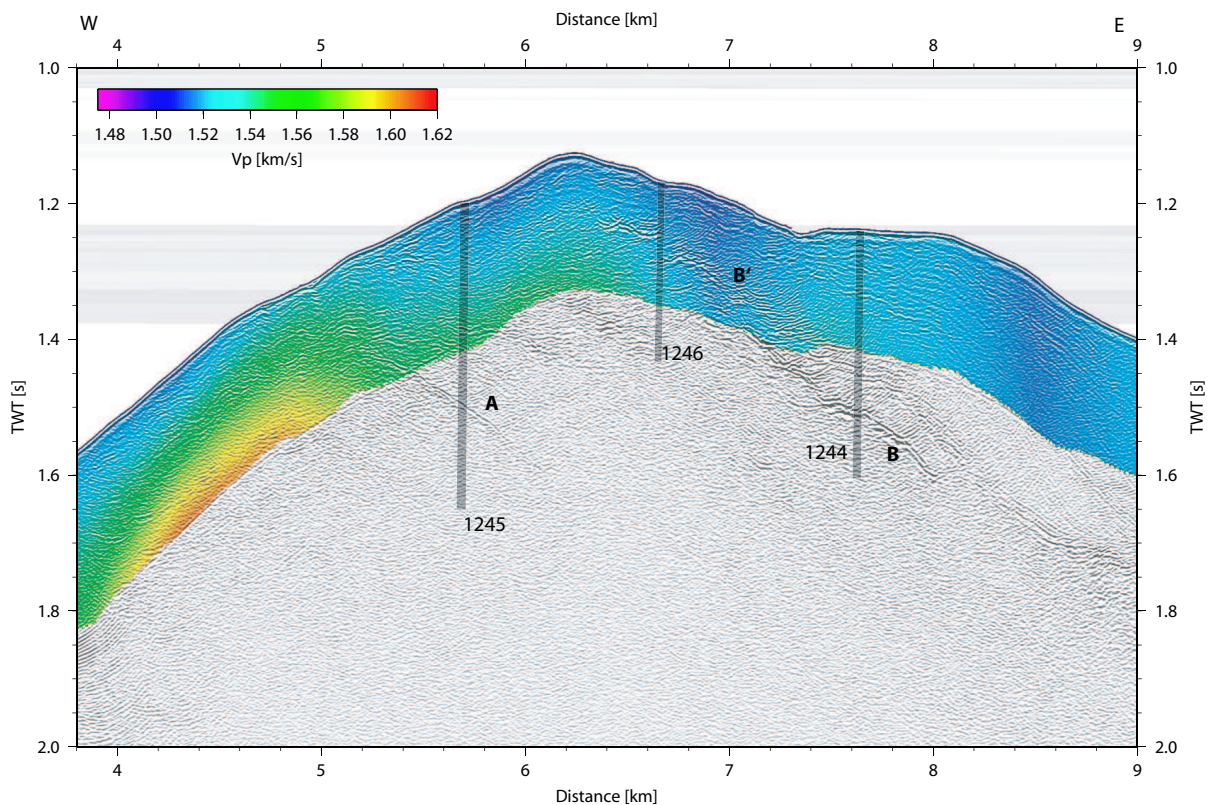


Figure 6.7: *Seismic GI-gun profile, water migrated, overlain with the velocity model, obtained from combined streamer and ocean bottom hydrophone data. OBS deployed during HYDGAS (yellow). New seismic data from OBS recordings (red circles) provide relevant data between the two 'yellow' deployments in addition to well log data of Site 1244, 1245 and 1246.*

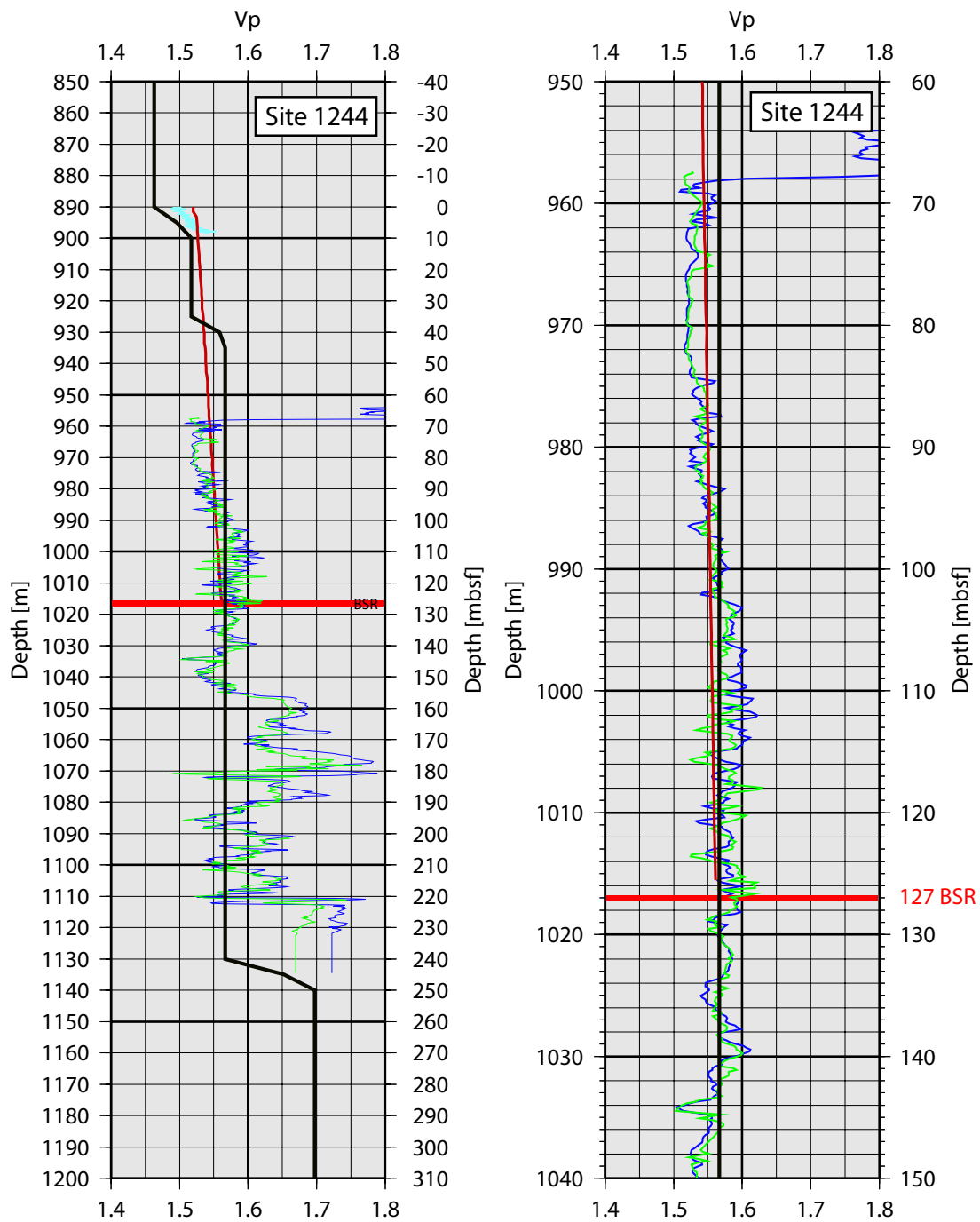


Figure 6.8: *P*-wave velocity log from ODP Site 1244 and a close up (right panel). The log consists of two passes (green and blue). Velocities, derived from the migration analysis of the MCS data are marked as black curves. The inverted velocities from ocean-bottom instruments are display in red. Additional to conventional wireline logging (CWL, green and blue) the upper 10 m of cores were logged and are displayed in light blue.

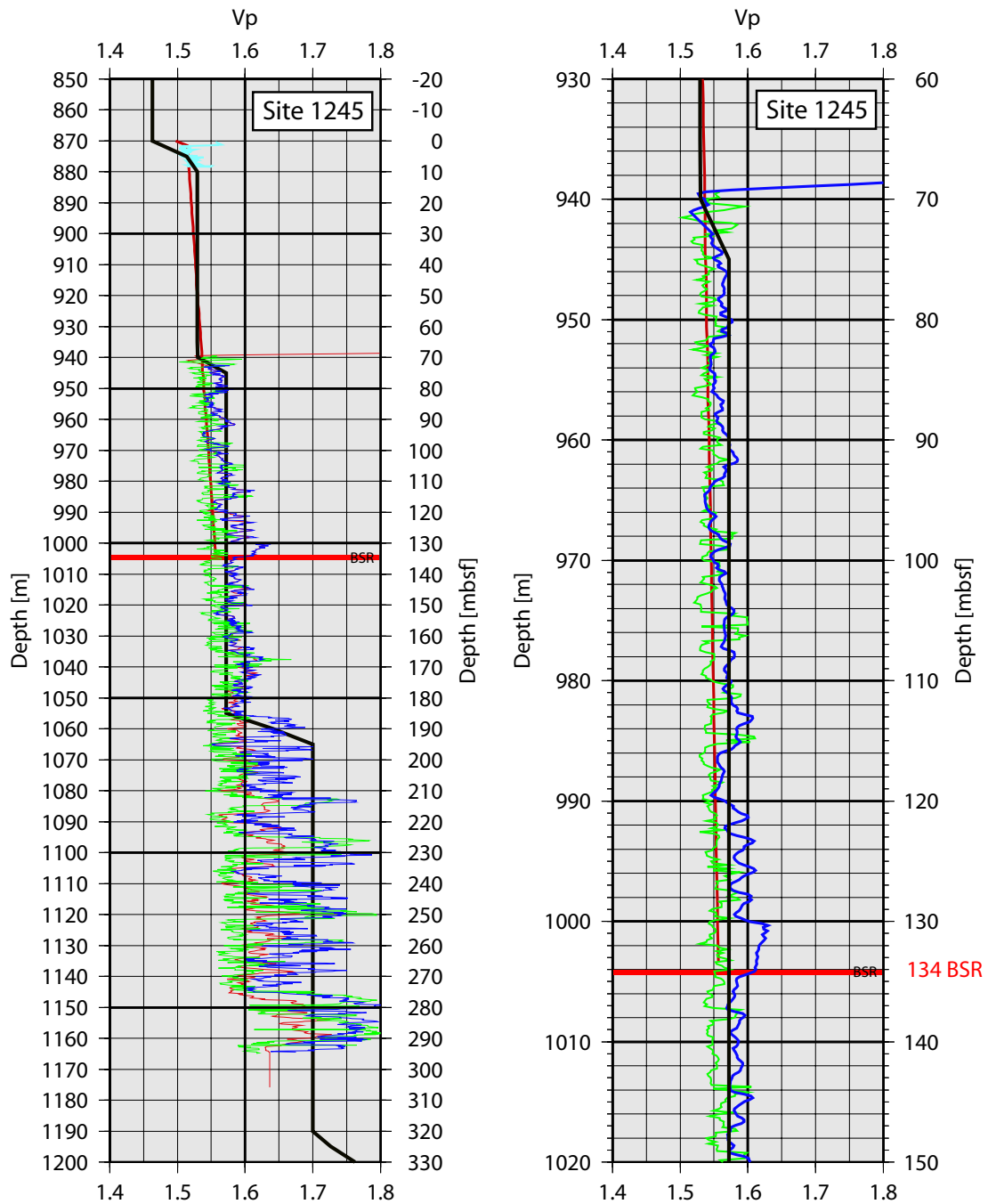


Figure 6.9: *P*-wave velocity logs from ODP Site 1245 and a close up (right panel). The log consists of two passes (green and blue). Velocities, derived out of the migration analysis of the MCS data are marked as black curves. The inverted velocities from ocean-bottom instruments are display in red. Additional to conventional wireline logging (CWL, green and blue) the upper 10 m of cores were logged and are displayed in light blue. Note the red curve, see text for details.

Guerin, Borehole Research Group, pers. commun.). The requested "new" pass (Fig. 6.9, red) agrees with the "old" log (Fig. 6.9, green) down to a depth of about 180 mbsf and follows the trend of pass 1 (Fig. 6.9, blue) with a shift of about +20 m/s. The reprocessed pass 2 as well as pass 1 do not resolve a velocity increase at a depth of ~ 190 mbsf, which was observed in the old pass 2 and was constrained with the MCS data. The velocity-depth profile, inverted from the OBS data (Fig. 6.9, red) ends at the depth of the BSR and correlates with both logs, the Hamilton frame logs for the upper 10 m and the deeper CWL logs below ~ 70 mbsf. The BSR depth of 125 m for site 1244 and 133 m for site 1245 obtained from the velocity analysis fits the results of ODP within an uncertainty of less than 5 m. Other proxies of ODP 204, defining the base of the gas hydrate stability zone (GHSZ), differ in depth of ± 5 m, allowing the conclusion that the inverted velocity model and the determination of the BSR depth before ODP was very accurate.

At Site 1245, and at all other sites with exception of those near the summit, no unambiguous indicators of gas hydrate were found in the upper ~ 40 m beneath the seafloor. All proxies indicate that gas hydrate is present sporadically between 40 mbsf and the BSR at 134 mbsf (*Tréhu et al., 2004*). The mean gas hydrate content at Site 1245 is $1.74\% \pm 0.15$ of pore space averaged over the gas hydrate stability zone (*Tréhu et al., 2004*). Site 1244 shows greater values and has a mean value of 3.24 ± 2.19 (*Tréhu et al., 2004*). These values were averaged over different holes drilled at each sites. The holes at 1244 showed a greater variability with two holes indicating gas hydrates contents of $> 5\%$ averaged over the GHSZ (*Tréhu et al., 2004*).

These values do not necessarily correlate with the results obtained from the velocity model. Although, the derived hydrate concentration of $\sim 1\%$ is within the uncertainty at Site 1245. At Site 1244 the presumed $\sim 1\%$ is below the mean value of 3.24%. However, in both cases the concentration of 1% is lower than the average results of ODP 204. *Tréhu et al. (2004)* concluded that the average gas hydrate content of the sediments (apart from the region near the summit) in the GHSZ is generally $< 2\%$ of pore space, although this estimate may increase by a factor of 2 when patchy zones of locally higher gas hydrate content are included in the calculation. These patchy zones, structurally and stratigraphically controlled, contain up to 20% hydrate in the pore space when averaged over zones ~ 10 m thick (*Tréhu et al., 2004*).

However, the patchy zones of locally higher amounts of gas hydrate are not resolved in the traveltimes inversion. The effect of thin hydrate layers on the average hydrate concentration of the entire GHSZ is demonstrated in Figure 6.10. The theoretical approach of this analysis is to evaluate the influence of a high-velocity hydrate layer on the V_{RMS} velocity. Above the BSR a thin hydrated layer is inserted containing a higher P-wave velocity. The thickness is then varied until the V_{RMS} velocity of the entire

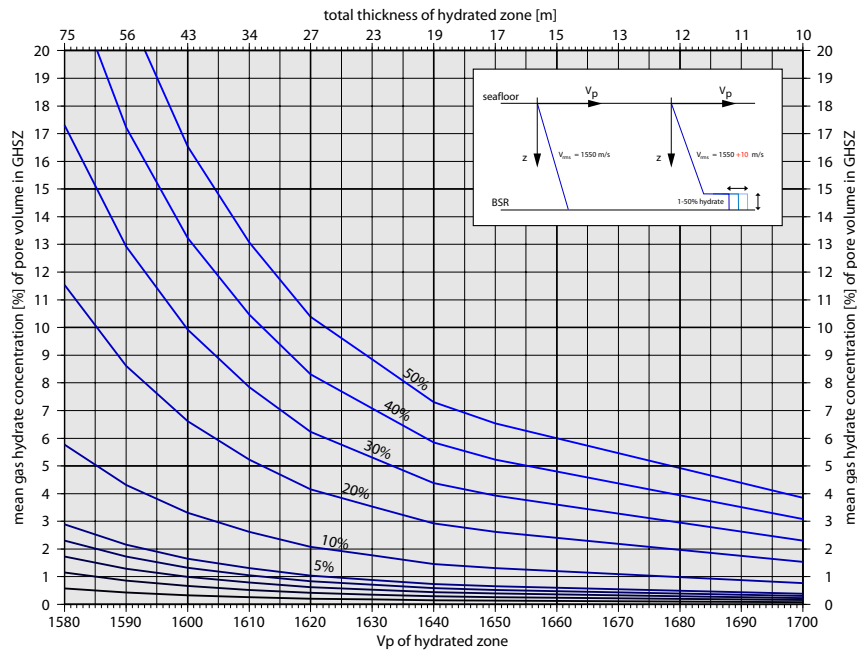


Figure 6.10: *The effect of a thin hydrated layer containing higher amounts (1-50%) of gas hydrate on the V_{RMS} of the entire GHSZ. Thin hydrated layers of higher P-wave velocities can be within the uncertainty of (10 m/s) of the average velocity-depth profile.*

GHSZ reaches a value of 10 m/s faster than the initial velocity. Thus, the maximum thickness of the hydrated layer is controlled by its defined P-wave velocity, since both, thickness and velocity, influence the V_{RMS} velocity. For a given P-wave velocity and hydrate concentration in the hydrated layer (Fig. 6.10, bottom axis and blue curve, respectively) the maximum allowed thickness (top axis) within the uncertainty of 10 m/s is calculated. In Figure 6.10 the effect of the hydrated layer is plotted against the average hydrate concentration over the entire GHSZ of 130m (left axis).

Peak velocities above the BSR, obtained from the sonic logs, are 1620 m/s. Peak values for hydrate saturation are 10% (Tréhu *et al.*, 2004). Consequently, assuming an uncertainty of 10 m/s within the velocity profile, a layer containing 10% of gas hydrate with a P-wave velocity of 1620 m/s, results in a maximum layer thickness of 27 m and an average hydrate concentration of 2% within the entire GHSZ. In conclusion, the predicted amount of 1% for the gas hydrate content, derived from the velocity analysis, correlates with the results of ODP 204 when considering thin hydrated layers of higher concentrations and an uncertainty of 10 m/s in the velocity model. This effect is even stronger when free gas is assumed within the GHSZ. Layers of high-velocity hydrate

combined with layers of low-velocity free gas result in moderate velocities averaged over the entire zone. *Milkov et al. (2004)* found evidence for the co-existence of gas hydrate, free gas, and brine within the GHSZ at Sites near the summit.

The inverted low velocities at the eastern flank of the ridge are in contrast to the results of ODP. The two holes from Site 1246 result in hydrate concentrations of 1.0% (1246A) and 5.0% (1246B) of pore space within the GHSZ (*Tréhu et al., 2004*). The low velocities at Site 1246 are related to the strong reflectivity pattern cross-cutting the BSR at that Site. This reflectivity pattern is assumed to be a pathway for upward migrating fluids and/or free gas, causing these relative low velocities. This strong reflectivity pattern is referred to as Horizons B and B', and sampling B and B' was the primary objective of drill Site 1244 and 1246. At Site 1246 both reflections, B and B', are within the GHSZ, compared to Site 1246, where both horizons are below the GHSZ. The principal scientific results of ODP suggest a model, where Horizon B' contains free gas at Site 1244 and that the disappearance of a observed density anomaly at Site 1246 results from the replacement of free gas by gas hydrate. The analysis of this model is still in progress. In postcruise studies future efforts will be focused on modeling the seismic response of these horizons as it changes from a fluid-rich layer beneath the BSR to a hydrate-bearing layer above it and to constrain the source and evolution of the fluids using geochemical data. Horizon B is caused by a pair of high density and low-porosity layers ~2.5m thick and spaced 10 m apart, and is believed to be formed by a turbidite sequence with a complicated internal structure indicating deposition, erosion, and redeposition. Electrical resistivity, Infra Red (IR) temperature, and geochemical measurements refer Horizon B as to a zone where gas hydrate preferentially forms.

Locally higher velocities at the western flank of the ridge (Fig. 6.7), reaching velocities of 1620 m/s at the BSR have been interpreted during the velocity analysis as a distinct sediment package of higher velocities, cross-cutting the BSR. During ODP 204, the top of this sediment unit was drilled at Site 1245 at an estimated depth of 310 mbsf. Unfortunately acoustic logging ended at 300 mbsf, but an increase in P-wave velocities at ~300m mbsf, derived from MCS data, can be correlated to a change in lithology from mainly clay and silty clay with frequent sand-rich turbidites to claystone and silty claystone with glauconite layers and turbidites.

At Sites 1244, 1245 and 1246 along the main seismic profile, roughly 1.5 km north of the summit, various proxies (electrical resistivity anomalies, low-temperature anomalies, low chloride concentration and gas volumes measured from pressure core samplers) for the presence of gas hydrate indicate that hydrate is distributed over a broad depth range. At sites away from the summit all proxies indicated that the presence of hydrate starts at ~20 - 50 meters below seafloor, although no indications for a top of the occurring hydrate zone was found within the seismic data. Furthermore, proxies indicate

that hydrate concentration probably varies considerably on scales of millimeters to tens of centimeters. Exceptions are Site 1251 in the eastern slope basin (Fig. 6.1), where hydrate is concentrated in a 12-m-thick tone just above the BSR, and sites near the summit, where it is concentrated near the seafloor. Unfortunately no wide-angle reflection data was collected at the location of Site 1251. However a strong BSR reflection within the SCS and MCS data indicates higher concentrations of gas hydrate just above the BSR (compare Figs. 2.11 and 2.12). At Site 1249 near the summit of Southern Hydrate Ridge cores contained hydrate in massive chunks, lenses, nodules and thin plates. The summit was crossed during the HYDGAS cruise with 8 sparker profiles to image the sub-seafloor in the vicinity of a ~50-m-high carbonate spire, the so-called 'pinnacle' (Fig. 6.11). *Tréhu et al. (2004)* estimates the average gas hydrate content in the upper 20-40 mbsf to be 30-40%. Below ~30 mbsf hydrate concentrations are similar to, or only slightly higher than, the concentrations beneath the flanks of southern Hydrate Ridge. Similar results were obtained at Sites 1248 and 1250, although the near-surface zone of hydrate content at Site 1250 is thinner (~15 m) (*Tréhu et al., 2004*). This zone can be correlated with the strong, chaotic reflectivity pattern within the sparker lines displayed in Figure 6.12. Overall, the gas hydrate distribution within the gas hydrate stability zone is highly variable over the entire southern ridge.

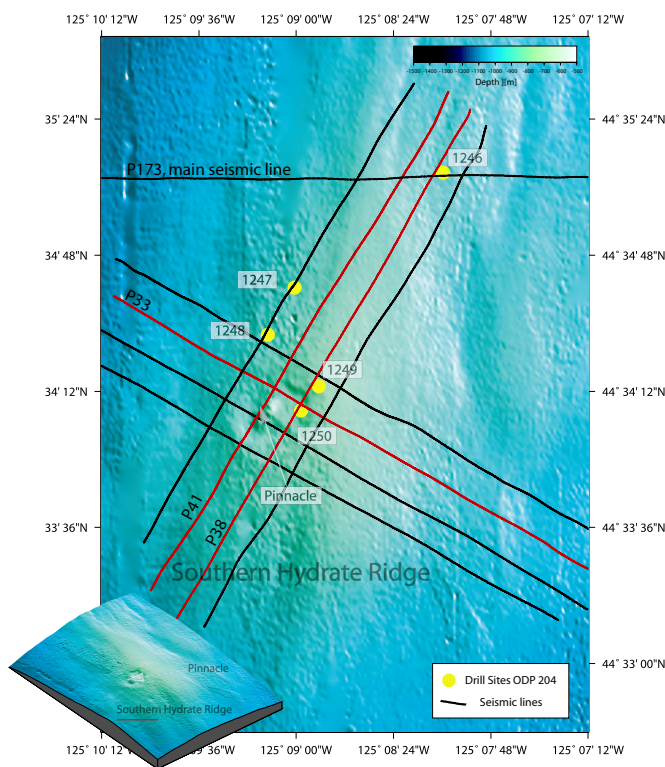


Figure 6.11: Map showing the bathymetry of the summit of Southern Hydrate Ridge. Eight high-resolution seismic sparker-profiles (SCS) were acquired during the HYDGAS cruise to image the sub-seafloor near the pinnacle, a ~50-m-high carbonate spire.

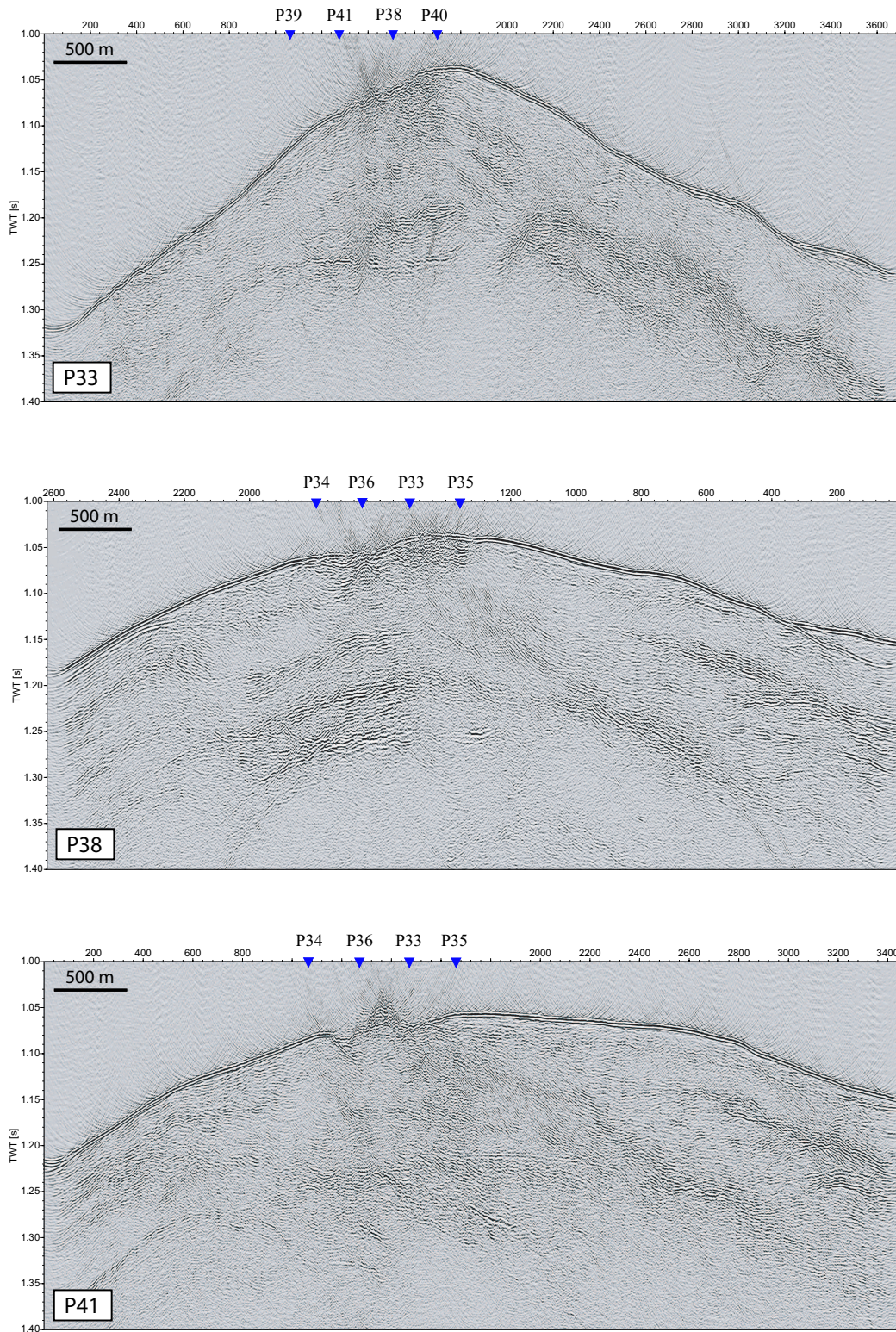


Figure 6.12: *Seismic time-migrated (constant water velocity) sparker sections of line p33, p38 and p41. The chaotic reflectivity pattern near the summit is indicative for massive gas hydrates.*

6.4 Free gas below the BSR

The negative polarity of the BSR indicates a V_p decrease across the stability boundary. In principle, this contrast may be caused by elevated V_p in gas hydrate bearing sediments above the base of the gas hydrate stability zone (*Hyndman and Spence, 1992*) and/or by low velocities in gas-charged layers beneath it (*Korenaga et al., 1997*). Results from various studies indicate that, with some possible exceptions, strong BSRs are principally caused by a drastic decrease of V_p due to free gas, with a relatively small contribution from an overlying "hydrate wedge" (*Korenaga et al., 1997*). At some locations, however, weaker BSRs may be caused by gas hydrates without underlying free gas (*Minshull et al., 1994; Pecher et al., 1996*). A major question regarding the operation of the hydrate/gas system is the thickness, origin, and dynamics of the free gas zone. VSPs conducted during Ocean Drilling Program Leg 164 on the Blake Ridge revealed that the hydrate zone there is underlain by a surprisingly thick gas zone of at least 250 m (*Holbrook et al., 1996*). The free gas zone is characterized by a region of a unusually low P-wave velocity (Fig. 6.13) that coincides with a band of high reflectivity that follows the stratigraphic layers. This can be explained by slight variations in gas concentrations across the layer boundaries, since V_p is very sensitive to gas at low concentrations. A similar band of high reflectivity has been reported offshore Pakistan (*Grevemeyer et al., 2000*). Drilling on the Cascadia margin (*MacKay et al., 1994*) and off Chile (*Bangs et al., 1993*), on the other hand, showed that the gas zones there are thin, which confirmed earlier results from waveform inversion (*Singh et al., 1993*). The cause of these large differences in the thickness of the gas zone are not understood, however, sediment permeability may play a key role (*Pecher and Holbrook, 2000*). The second significant seismic characteristic of hydrate cementation, called "blanking" is also displayed in Figure 6.13. Blanking is the reduction of the amplitude (weakening) of seismic reflections probably caused by the presence of gas hydrate. Many observa-

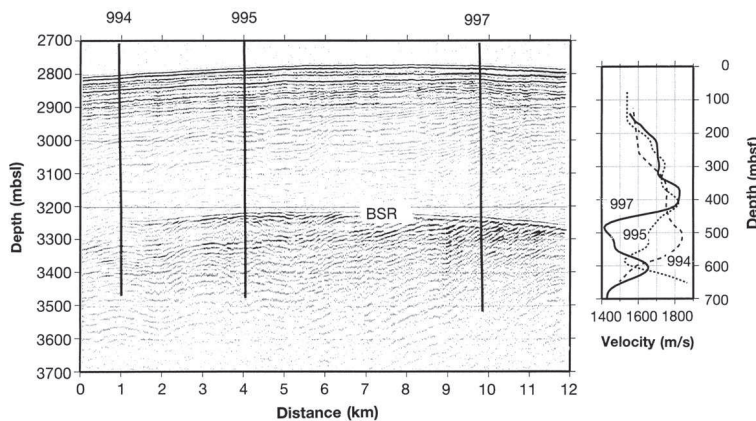


Figure 6.13: *Strong reflections below the BSR, indicative for free gas. low reflectivity (blanking) above the BSR, due to hydrate formation, from Holbrook et al. (1996).*

tions of blanking in nature have been associated with gas hydrate accumulations (*Lee et al.*, 1993, 1994, 1996), but the reality of blanking was questioned by *Holbrook et al.* (1996). Blanking is thought to result from preferential accumulation of gas hydrate in the more porous sedimentary strata, where it would increase the velocity of the more porous, initially lower velocity layers by the introduction of high-velocity, gas hydrate cement. This would create a more uniform, higher velocity, resulting in reduced seismic acoustic impedance contrasts and thus reduced reflection strengths. *Pecher and Holbrook* (2000) concluded that the low reflectance above the BSR at Blake Ridge is "normal", due to unusually homogeneous sediment (*Paull et al.*, 1996), while the strong reflections below the BSR are simply bright spots associated with a surprisingly thick free gas zone (*Holbrook et al.*, 1996).

The amplitude and frequency analyses of the seismic data suggest the presence of free gas beneath the BSR. Although, traveltime and depth-focusing considerations constrained the thickness of a gas layer to be relatively thin. The frequency analysis result an average thickness of 8 meters.

Neither amplitude blanking above the BSR nor enhanced reflections below the BSR are observed in the seismic data. Locally high reflections below the BSR are linked to specific horizons that may act as conduits for free gas migrating upward into the gas hydrate stability zone. Especially seismic reflector A (Fig. 6.7) is assumed to be a pathway for fluids and/or gas. The reflector has a negative phase, presumably caused by free gas or fluids. This reflector was crossed at four sites during ODP Leg 204 and LWD (Logging while drilling) measurement revealed that this reflector is characterized by a strong 2- to 4-m-wide double-peaked low density and low-resistivity anomaly. Microscopic analyses of sediments of cores at Sites 1245, 1248 and 1250 reveal the sediment is composed primarily of relatively fresh glass shards indicating volcanic ash. Chemical analyses of ODP support the interpretation that it is a conduit for fluids coming from a greater depth. The occurrence of free gas was assumed to be restricted only to this 2-4 m interval.

In general ODP found no indication of a thick gas layer beneath the BSR. PCS (pressure core sampler) measurements of gas concentration during Leg 204 indicate that free gas is present beneath the BSR but only in thin layers. The thickness of the gas layer was not determined during ODP 204. Although at Site 1250 free gas appears to be present in relatively high concentrations (perhaps around 4% of pore space) at a depth of ~7.5 m below the BSR, whereas only dissolved methane seems to be present in the core derived from ~24 m below the BSR. At Site 1250 the presence of free gas just below the BSR is documented by the concentrations of methane well above in situ solubility found in a PCS core from ~5 m below the BSR and from P-wave data

obtained by sonic logs. The V_p -logs of Sites 1244 and 1245 (Figs. 6.8 and 6.9) along the main seismic line do not reveal a significant drop of the P-wave velocity beneath the BSR and hence suggest rather low concentrations of free gas.

At all ODP drill sites an enrichment of ethane beneath the BSR was observed. ODP proposed two models for this observation. In one model the BSR serves as a barrier to upflow of ethane. In the other model, ethane is preferentially incorporated into hydrate; dissociation of the hydrate at a later time in response to tectonic uplift recycles ethane into the free gas zone beneath the hydrate. ODP found indications for both models and suggests the possibility that both mechanisms operate simultaneously. However, a thin layer of free gas underneath the BSR along the entire ridge prefers the first model, where free gas is recycled from gas hydrate due to tectonic uplift.

In conclusion, there is no direct indication of a thick gas zone beneath the BSR at all Sites. Free gas beneath the BSR is assumed to be in thin layers. Direct evidence of free gas was found at Site 1250 ~ 5 m below the BSR, whereas ~ 24 m below the BSR gas was found below saturation at in situ condition. At other Sites indicators for free gas were restricted to thin horizons, e.g. reflector A. Therefore, the observations of ODP Leg 204 on a thin free gas zone beneath the BSR generally agree with the results of the seismic investigations.

7 Conclusion and Outlook

Gas hydrates and free gas, as indicated by the seismic proxy known as the BSR, are widespread on the Southern Hydrate Ridge. Different approaches on analyzing the BSR with respect to possible hydrate formation above and free gas below the gas hydrate stability zone is presented in this study.

Velocity analysis

(1) The simultaneous traveltimes inversion of the OBH/OBS and SCS data leads to an accurate P-wave velocity model, which is constrained by ODP acoustic log measurements. By combining the different acquisition geometries, the inversion runs more stable compared to a single acquisition geometry due to the increased ray coverage. The deeptow streamer data is not included in the inversion algorithm, but independent forward modeling of the inverted velocity model fit the data of the deeptow streamer. The combination of simultaneous and independent usage of the different geometries results in a well constrained velocity model.

(2) The prediction of the BSR depth of 125 m and 133 m for Sites 1244 and 1245, derived from the velocity analysis prior to ODP drilling, is within 5 m of the results of ODP Leg 204.

(3) Zones of higher acoustic velocities do not necessarily have to indicate the presence of gas hydrates. BSRs might cross-cut lithological units of higher seismic velocities. This change in velocities is observed at the western flank of Hydrate Ridge, where sedimentary units cross-cut the BSR and consequently increase the P-wave velocity within the GHSZ. Depth-focusing analyses of the MCS data constrain this observation. This sediment unit was cored during ODP Leg 204 and is related to a change in lithology. Consequently, it can be ruled out, that this velocity anomaly is caused by a change in hydrate formation.

(4) The velocity analysis suggests general low concentrations of gas hydrates within the GHSZ. P-wave velocities of less than 1600 m/s within the GHSZ result in an estimate of 1% gas hydrates within the pore space, by comparing analyses of other hydrate provinces. Results of ODP 204 lead to an average hydrate concentration of below 2%, although higher amounts of gas hydrate (up to 20%) were found. These are limited to layers of a few tens of centimeters. In addition, ODP results have found strong evidence for the presence of free gas within the hydrate stability zone. The co-existence of hydrate and free gas within the GHSZ is a very important aspect when hydrate

concentrations are derived from acoustic velocities. Gas hydrates within the sediment generally increase P-wave velocities, which is used as a seismic proxy to locate hydrate formation. This process is severely influenced when free gas is present. Changes of the acoustic parameters, caused by relatively thin layers of free gas and/or higher concentrations of gas hydrates, are not resolved with the inversion method presented in this study. However, the uncertainty of the derived velocities is 10 m/s. Therefore, a 20 m thick layer containing 10% hydrate with a P-wave velocity of 1620 m/s is still within the velocity uncertainty and subsequently increases the average hydrate concentration over the entire GHSZ of 130 m from 1% to 2%. In conclusion, the hydrate concentration could be estimated by P-wave velocity analyses without further investigation of S-wave velocities. For a more accurate estimation, thin layering within the GHSZ, containing either free gas or a change in the hydrate concentration, have to be considered in future investigations.

(5) There is no evidence for a decrease of the P-wave velocity below the BSR resulting from the velocity analysis of the streamer and ocean bottom instrument data. This leads to the assumption that free gas at Southern Hydrate Ridge is only present in thin layers.

Amplitude and frequency analysis

(1) Different source frequencies lead to different reflection BSR amplitudes, caused by the tuning effect of a thin gas bearing layer beneath the BSR. This amplitude variation is due to the signal-interference of the top and bottom layer boundary. The result of the frequency analysis leads to a layer thickness for the free gas layer of 3 to 11 m.

(2) Strong lateral amplitude variations at low frequencies compared to small variations at high frequencies are explained by the different tuning thicknesses for each frequency range.

(3) The results of the standard AVO analysis provides a rough estimate for the physical parameters at the BSR interface. Large discrepancies in the velocities below the BSR result from the approximation of the BSR representing a single interface. Because standard AVO analysis, based on the Zoeppritz equations, is only applicable for single interfaces, detailed AVO-modeling studies are necessary to account for a thin gas layer beneath the BSR. (4) The amplitude corrections for the AVO analysis dominate the AVO-trend and therefore an accurate velocity model is essential for deriving the necessary correction factors and acquisition geometry. (5) The results of ODP drilling suggested that free gas is present below the BSR but only in thin layers. No estimation on the layer thickness was made during ODP, but free gas was not found deeper than 7 meters below the BSR. With an error of 4 m, this is consistent with the result of a 3 to 11 m thick gas layer, derived from the frequency analysis.

(6) At all ODP drill sites an enrichment of ethane beneath the BSR was observed. A thin layer of free gas underneath the BSR along the entire ridge prefers a model, where free gas is recycled from gas hydrate due to tectonic uplift.

(7) The amplitude variations along the BSR are presumably caused by changing gas saturations and layer thicknesses of the gas layer.

(8) The P-wave velocities within the GHSZ obtained from the velocity inversion are constrained by the standard AVO analysis of three OBS. The derived velocities below the BSR are lower, compared to the results of ODP leg 204. This discrepancy is either due to the uncertainty of the acoustic logs or due to the uncertainty in the amplitude calibration during the AVO analysis.

In total, the heterogeneous distribution of gas hydrates within the hydrate stability zone and the presence of gas in thin layers severely influences the nature of the BSR. In general it is assumed and widely observed that the gas hydrate content decreases gradually when moving closer to the seafloor. At Southern Hydrate Ridge, hydrate was found in high concentrations below the seafloor near the summit. Along the main seismic line, a few hundred meters north of the summit, hydrate was found sporadically almost throughout the entire GHSZ. At some locations there was no indication of formed hydrate just above the BSR. All these observations have different effects on the BSR depth and amplitude and have to be considered when future studies on BSR are carried out. In conclusion, the results of the various analyses of the BSR at Southern Hydrate Ridge, presented in this study, are confirmed by the results of Ocean Drilling Program Leg 204 and considerations for future studies on gas hydrates were presented.

Bibliography

- Aki, K., and P. Richards, *Quantitative Seismology: Theory and Methods*, 932 pp pp., W.H. Freeman and Co., San Francisco, 1980.
- Almoghrabi, H., and J. Lange, Layers and bright spots, *Geophysics*, *51*, 699–709, 1986.
- Andreassen, K., K. Hogstad, and K. Berteussen, Gas hydrate in the southern Barents Sea, indicated by a shallow seismic anomaly, *First Break*, *8*, 235–245, 1990.
- Andreassen, K., P. Hart, and A. Grantz, Seismic studies of a bottom simulating reflection related to gas hydrate beneath the continental margin of the Beaufort Sea, *J. Geophys. Res.*, *100*(B7), 12,659–12,673, 1995.
- Andreassen, K., K. Berteussen, H. Sognes, K. Henneberg, J. Langhammer, and J. Mienert, Multicomponent ocean bottom cable data in gas hydrate investigation offshore Norway, *Journal of Geophysical Research*, *108*, 2399–2409, doi:10.1029/2002JB002245, 2003.
- Backus, M. M., Water reverberations: Their nature and elimination, *Geophysics*, *24*, 233–261, 1959.
- Bangs, N., and I. Pecher, Shear wave studies of Hydrate Ridge, Oregon Margin: R/V Ewing and JOIDES Resolution Seismic Experiments, *EW0208 Cruise Report, R/V Maurice Ewing*, 2002.
- Bangs, N. L., D. S. Sawyer, and X. Golovchenko, Free gas at the base of the gas hydrate zone in the vicinity of the Chile triple junction., *Geology*, *21*, 905–908, 1993.
- Bevington, P., Data reduction and error analysis for the physical sciences, *McGraw-Hill, New York*, 1969.
- Bialas, J., and E. Flueh, Ocean Bottom Seismometers, *Sea Technology*, *40*(4), 41–46, 1999.

- Bohrmann, G., J. Greinert, E. Suess, and M. Torres, Authigenic carbonates from the Cascadia subduction zone and their relation to gas hydrate stability, *Geology*, *26*, 647–650, 1998.
- Bohrmann, G., P. Linke, E. Suess, and O. Pfannkuche, Cruise Report SO143 TECFLUX, *GEOMAR Report 93*, GEOMAR Research Center for Marine Geosciences, iSSN 0936-5788, 2000.
- Bortfeld, R., Approximation to the reflection and transmission coefficients of plane longitudinal and transverse waves, *Geophys. Prosp.*, *9*, 485–503, 1961.
- Carcione, J., and U. Tinivella, Bottom-simulating reflectors: Seismic velocities and AVO effects, *Geophysics*, *65*(1), 54–67, 2000.
- Castagna, J. P., and M. M. Backus, *Offset dependent Reflectivity - Theory and practise of AVO analysis*, first ed., Society of Exploration Geophysicists, 1993.
- Chapman, N., J. Gettrust, R. Walla, D. Hannay, G. Spence, W. Wood, and R. Hyn-dman, High-resolution, deep-towed, multichannel seismic survey of deep-sea gas hy-drates off western Canada, *Geophysics*, *67*(4), 1038–1047, 2002.
- Clague, D., N. Maher, and C. K. Paull, High-resolution multibeam survey of Hy-drate Ridge, offshore Oregon, In Paull, C.K., and Dillon, W.P. (Eds.) *Natural Gas Hydrates: Occurrence, Distribution, and Detection. Am. Geophys. union, Geophys. Monogr. Ser.*, *124*, 297–306, 2001.
- Cohen, J. K., and J. J. W. Stockwell, *CWP/SU: Seismic Unix Release 35: a free package for seismic research and processing*, Center for Wave Phenomena Colorado School of Mines, 2001.
- Dickens, G. R., C. K. Paull, P. Wallace, and O. L. S. Party, Direct measurements of in situ methane quantities in a large gas-hydrate reservoir, *Nature*, *385*, 426–428, 1997.
- Dillon, W., and C. Paull, Marine gas hydrate, II, geophysical evidence, in *natural gas hydrates: properties, occurrence and recovery*, Butterworth-Heinemann, Stoneham, Mass., pp. 73–90, 1983.
- Dvorkin, J., M. Prasad, A. Sakai, and D. Lavoie, Elasticity of marine sediments: Rock physics modeling, *Geophys. Res. Lett.*, *26*(12), 1781–1784, 1999.
- Ecker, C., and D. Lumley, Seismic AVO analysis of methane hydrate structures, *64th Ann. Internat. Mtg., Soc. Expl. Geophys., Expanded Abstracts*, pp. 1100–1103, 1994.

- Ecker, C., J. Dvorkin, and A. Nur, Sediments with gas hydrates: Internal structure from seismic AVO, *Geophysics*, *63*(5), 1659–1669, 1998.
- Ecker, C., J. Dvorkin, and A. Nur, Estimating the amount of gas hydrate and free gas from marine seismic data, *Geophysics*, *65*(2), 565–573, 2000.
- Gedom, M., A. M. Tréhu, E. R. Flueh, and D. Klaeschen, The continental margin off oregon from seismic investigation, *Tectonophysics*, *329*, 2000.
- Grevemeyer, I., A. Rosenberger, and H. Villinger, Natural gas hydrates on the continental slope off Pakistan: constraints from seismic techniques., *Geophys. J. Int*, *140*, 295–310, 2000.
- Guerin, G., D. Goldberg, and A. Meltser, Characterization of in situ elastic properties of gas hydrate-bearing sediments on the Blake Ridge, *J. Geophys. Res.*, *104*, 17,781–17,795, 1999.
- Hamarbitan, N. S., and G. F. Margrave, Spectral analysis of a ghost, *Geophysics*, *66*, 1267–1273, 2001.
- Hamilton, E., Elastic properties of marine sediments, *Geophysics*, *76*, 579–604, 1971.
- Hamilton, E., Compressional-wave attenuation in marine sediments, *Geophysics*, *37*(4), 620–646, 1972.
- Hamilton, E., Shear-wave velocity versus depth in marine sediments: a review, *J. Geophys. Res.*, *41*, 985–996, 1976a.
- Hamilton, E., Variations of density and porosity with depth in deep-sea sediments, *J. Sediment. Petrol.*, *46*(2), 280–300, 1976b.
- Hamilton, E., Sound velocity gradients in marine sediments, *J. Acoust. Soc. Am.*, *65*, 909–922, 1979a.
- Hamilton, E., Sound velocity gradients in marine sediments, *J. Acoust. Soc. Am.*, *65*, 909–922, 1979b.
- Hammond, J. W., Ghost elimination from reflection records, *Geophysics*, *27*, 48–60, 1962.
- Hargreaves, N. D., Air-gun signatures and the minimum-phase assumption, *Geophysics*, *57*, 263–271, 1992.
- Haris, A., Amplitude-preserving migration and its application to imaging of a bsr in marine multichannel seismic reflection data, Ph.D. thesis, GEOMAR, 2003.

- Henry, P., M. Thomas, and M. B. Clennell, Formation of natural gas hydrates in marine sediments: Thermodynamic calculations of stability conditions in porous marine sediments, *J. Geophys. Res.*, *104*, 23,005–23,020, 1999.
- Holbrook, W., H. Hoskins, W. Wood, R. Stephen, D. Lizzarralde, and the Leg 164 Science Party, Methane hydrate and free gas on the Blake Ridge from vertical seismic profiling, *Science*, *273*, 1840–1843, 1996.
- Hornbach, M. J., W. S. Holbrook, A. R. Gorman, K. L. Hackwith, D. Lizzarralde, and I. Pecher, Direct seismic detection of methane hydrate on the Blake Ridge, *Geophysics*, *68*, 92–100, 2003.
- Hyndman, R., and G. Spence, A seismic study of methane hydrate marine bottom simulating reflectors, *J. Geophys. Res.*, *97*(B5), 6683–6698, 1992.
- Johnson, D. T., Understanding air-gun bubble behavior, *Geophysics*, *59*, 1729–1734, 1994.
- Johnston, D. H., M. N. Toksöz, and A. Timur, Attenuation of seismic waves in dry and saturated rocks: II mechanisms, *Geophysics*, *44*, 691–711, 1979.
- Juhlin, C., and R. Young, Implications of thin layers for amplitude with offset (AVO) studies, *Geophysics*, *58*, 1200–1204, 1993.
- Kallweit, R. S., and L. C. Wood, The limits of resolution of zero-pase wavelets, *Geophysics*, *47*, 1035–1046, 1982.
- Kastner, M., K. Kvenvolden, M. Whiticar, A. Camerlenghi, and T. Lorenson, Relation between pore fluid chemistry and gas hydrates associated with Bottom-Simulating Reflectors at the Cascadia margin, Sites 889 and 892, in *Proc. ODP, Sci. Results*, vol. 146, edited by B. Carson, G. Westbrook, R. Musgrave, and E. Suess, pp. 175–187, Texas AM University, Ocean Drilling Program, College Station, TX, United States, 1995.
- Katzman, R., W. Holbrook, and C. Paull, Combined vertical-incidence and wide-angle seismic study of a gas hydrate zone, Blake Ridge, *J. Geophys. Res.*, *99*, 17,975–17,995, 1994.
- Klaeschen, D., A. Kopf, M. Arsenault, and J. Bialas, Cruise Report SO150 HYDGAS - Quantification of gas hydrates and gas in the sediments of the Cascadia accretionary wedge using seismic methods, *Report*, GEOMAR Research Center for Marine Geosciences, 2001.

- Knott, C. G., Reflexion and refraction of elastic waves with seismological applications, *Phil. Mag.*, *48*, 64–97, 1899.
- Koefoed, O., and N. D. Voogd, The linear properties of thin layers with an application to synthetic seismograms over coal seams, *Geophysics*, *45*, 1254–1268, 1980.
- Korenaga, J., W. S. Holbrook, S. C. Singh, and T. A. Minshull, Natural gas hydrates on the southeast US margin: Constraints from full waveform and travel time inversion of wide-angle seismic data, *J. Geophys. Res.*, *102*, 15,345–15,365, 1997.
- Larner, K., D. Hale, S. M. Zinkham, and C. Hewlitt, Desired seismic characteristics of an air gun source, *Geophysics*, *47*, 1723–1284, 1982.
- Lee, M., D. Hutchinson, W. Agena, W. Dillon, J. Miller, and B. Swift, Method of estimating the amount of in-situ gas-hydrates in deep marine sediments, *Marine Petr. Geol.*, *10*, 493–506, 1993.
- Lee, M., D. Hutchinson, W. Agena, W. Dillon, J. Miller, and B. Swift, Seismic character of gas hydrates on the southeastern U.S. continental margin, *Marine Geophys. Res.*, *16*, 163–184, 1994.
- Lee, M., D. Hutchinson, T. Collett, and W. Dillon, Seismic velocities for hydrate-bearing sediments using weighted equation, *J. Geophys. Res.*, *101*(B9), 20,347–20,358, 1996.
- Lindsey, J. P., Elimination of seismic ghost reflections by means of a linear filter, *Geophysics*, *25*, 130–140, 1960.
- Linke, P., and E. Suess, Cruise Report SO148 TECFLUX-II - tectonically-induced material fluxes, *GEOMAR Report 98*, GEOMAR Research Center for Marine Geosciences, iSSN 0936-5788, 2001.
- MacKay, M., Structural variation and landward vergence at the toe of the Oregon accretionary prism, *Tectonics*, *14*, 1309–1320, 1995.
- MacKay, M., G. Moore, G. Cochrane, J. Moore, and L. Kulm, Landward vergence and oblique structural trends in the Oregon margin accretionary prism: Implications and effect on fluid flow, *Earth Planet. Sci. Lett.*, *109*, 477–491, 1992.
- MacKay, M., R. Jarrad, G. Westbrook, R. Hyndman, and the Shipboard Scientific Party of ODP Leg 146, Origin of bottom simulating reflectors: geophysical evidence from the Cascadia accretionary prism, *Geology*, *22*, 459–462, 1994.

- MacKay, M., R. Jarrad, G. Westbrook, R. Hyndman, and the Shipboard Scientific Party of ODP Leg 146, Technical notes and additions to: Origin of bottom simulating reflectors: geophysical evidence from the Cascadia accretionary prism, in *Proc. ODP, Sci. Results*, vol. 146, edited by B. Carson, G. Westbrook, R. Musgrave, and E. Suess, pp. 461–463, Texas AM University, Ocean Drilling Program, College Station, TX, United States, 1995.
- McCaffrey, R. ., and C. Goldfinger, Forearc deformation and great subduction earthquakes: Implications for Cascadia offshore earthquake potential, *Science*, *267*, 856–859, 1995.
- Milkov, A. V., G. R. Dickens, G. E. Claypool, Y.-J. Lee, W. S. Borowski, M. E. Torres, W. Xu, H. Tomaru, A. M. Tréhu, and P. Schultheiss, Co-existence of gas hydrate, free gas, and brine within the regional gas hydrate stability zone at Hydrate Ridge (Oregon margin): evidence from prolonged degassing of a pressurized core., *Earth Planet. Sci. Lett.*, *222*, 829–843, 2004.
- Miller, J., M. Lee, and R. von Huene, An analysis of a seismic reflection from the base of a gas hydrate zone, offshore Peru, *AAPG Bull.*, *75*, 910–924, 1991.
- Minshull, T., S. Singh, and G. Westbrook, Seismic velocity structure at a gas hydrate reflector offshore western Colombia, from full waveform inversion, *J. Geophys. Res.*, *99*(B3), 4715–4734, 1994.
- Neidell, N. S., and E. Poggiagliolmi, Stratigraphic modeling and interpretation – geophysical principles and techniques, *Seismic stratigraphy, Applications to hydrocarbon exploration*, *Am. Assn. Petr. Geol. memoir*, *26*, 389–416, 1977.
- Otterbein, C., Untersuchung der lateralen Auflösung verschiedener Meßsysteme der marinen Reflexionsseismik, Ph.D. thesis, GEOMAR, diploma thesis, 1997.
- Paull, C. K., W. I. Ussler, and W. S. Borowski, Sources of biogenic methane to form marine gas hydrates - in situ production or upward migration?, *Annales of the New York Academy of Sciences*, *715*, 392–409, 1994.
- Paull, C. K., R. Matsumoto, P. Wallace, and et. al., Proceedings of the Ocean Drilling Program, Initial Reports 164, *Ocean Drilling Program, College Station, TX*, p. 623pp, 1996.
- Pecher, I., and W. S. Holbrook, *Natural Gas Hydrate in Oceanic and Permafrost Environment*, second ed., 275-294 pp., Kluwer Academic Publishers, 2000.

- Pecher, I., C. Ranero, R. von Huene, T. Minshull, and S. Singh, The nature and distribution of bottom simulating reflectors at the Costa Rican convergent margin, *Geophys. J. Int.*, *133*, 219–229, 1998.
- Pecher, I. A., R. von Huene, C. Ranero, N. Kukowski, T. A. Minshull, and S. C. Singh, Formation mechanisms of free gas beneath the hydrate stability zone at convergent margins - geophysical evidence from bottom simulating reflectors at the Peruvian and Pacific Costa Rican margins, *Proceedings International conference on natural gas hydrates*, pp. 593–600, 1996.
- Petersen, C., Seismic characterization of marine gas hydrates and free gas at Northern Hydrate Ridge, Cascadia margin, Ph.D. thesis, IFM-GEOMAR, PhD thesis, 2004.
- Richards, P. G., and C. W. Frasier, Scattering of elastic wave from depth-dependent inhomogeneities, *Geophysics*, *41*, 441–458, 1976.
- Ricker, N. H., The computation of output disturbances from amplifiers for true wavelet inputs, *Geophysics*, *10*, 207–220, 1945.
- Robertson, J. D., and H. H. Nogami, Complex seismic trace analysis of thin beds, *Geophysics*, *49*, 344–352, 1984.
- Rutherford, S. R., and R. H. Williams, Amplitude-versus-offset variations in gas sands, *Geophysics*, *54*, 680–688, 1989.
- Sheriff, R., Nomogram for Fresnel-zone calculation, *Geophysics*, *45*(5), 968–972, 1980.
- Sheriff, R., and L. Geldart, *Exploration Seismology*, second ed., Cambridge University Press, 1995.
- Shuey, R., A simplification of the Zoeppritz equations, *Geophysics*, *50*(4), 609–614, 1985.
- Singh, S., T. Minshull, and G. Spence, Velocity structure of a gas hydrate reflector, *Science*, *260*, 204–207, 1993.
- Sloan, E., *Clathrate Hydrates of Natural Gases*, second ed., Marcel Dekker, 1998.
- Spence, G., T. Minshull, and C. Fink, Seismic studies of methane gas hydrate, offshore Vancouver Island, in *Proc. ODP, Sci. Results*, vol. 146, edited by B. Carson, G. Westbrook, R. Musgrave, and E. Suess, pp. 163–174, Texas AM University, Ocean Drilling Program, College Station, TX, United States, 1995.

- Stern, L. A., S. H. Kirby, W. B. Durham, S. Circone, and W. F. Waite, *Natural Gas Hydrate in Oceanic and Permafrost Environment*, second ed., 275-294 pp., Kluwer Academic Publishers, 2000.
- Stoll, R., and G. Bryan, Physical properties of sediments containing gas hydrates, *J. Geophys. Res.*, *84*, 1629–1634, 1979.
- Suess, E., and G. Bohrmann, Cruise Report SO110 SO-RO, *GEOMAR Report 59*, GEOMAR Research Center for Marine Geosciences, iSSN 0936-5788, 1997.
- Suess, E., M. Torres, G. Bohrmann, R. Collier, J. Greinert, P. Linke, G. Rehder, A. Tréhu, K. Wallmann, G. Winckler, and E. Zuleger, Gas hydrate destabilization: enhanced dewatering, benthic material turnover and large methane plumes at the Cascadia convergent margin, *Earth Planet. Sci. Lett.*, *170*, 1–15, 1999.
- Thore, P., and C. Juliard, Fresnel zone effect on seismic velocity resolution, *Geophysics*, *64*(2), 593–603, 1999.
- Tinivella, U., and J. M. Carcione, A model of wave propagation in a porous medium saturated by a two-phase fluid, *Journ. Acoust. Soc. Am.*, *87*, 1439–1448, 1990.
- Tinivella, U., and J. M. Carcione, Estimation of gas-hydrate concentration and free-gas saturation from log and seismic data, *The Leading Edge*, *20*, 200–203, 2001.
- Toksöz, M. N., and D. H. Johnston, *Eds., Seismic wave attenuation*, Soc. of Explor. Geophys., 1981.
- Torres, M., J. McManus, D. Hammond, M. de Angelis, K. Heeschen, S. Colbert, M. Tryon, K. Brown, and E. Suess, Fluid and chemical fluxes in and out of sediments hosting methane hydrate deposits on Hydrate Ridge, OR, I: Hydrological provinces, *Earth Planet. Sci. Lett.*, *201*, 525–540, 2002.
- Torres, M. E., S. Colbert, R. W. Collier, M. deAngelis, D. Hammond, K. Heeschen, D. Hubbard, J. McManus, C. Moyer, G. Rehder, A. M. Tréhu, M. Tyron, and P. Whaling, Active gas discharge resulting from decomposition of gas hydrates on Hydrate Ridge, Cascadia margin, *EOS, Trans.*, *79*, 461, 1998.
- Torres, M. E., G. Bohrmann, K. Brown, S. Colbert, M. deAngelis, D. Hammond, G. Klinkhammer, J. McManus, E. Suess, and A. M. Tréhu, Geochemical observations on Hydrate Ridge, Cascadia margin, *Oregon State Univ. Data Rpt.*, *174*, 99–103, 1999.
- Tréhu, A., N. Bangs, M. Arsenault, G. Bohrmann, C. Goldfinger, J. Johnson, Y. Nakamura, and M. Torres, Complex subsurface plumbing beneath southern Hydrate

- Ridge, Oregon continental margin, from high-resolution 3D seismic reflection and OBS data, *Proceedings of the 4th International Conference on Gas Hydrates, Yokohama, Japan, 2002*.
- Tréhu, A., G. Bohrmann, F. Rack, and M. T. et al., *Proceedings of the Ocean Drilling Program; initial reports*, vol. 204, Texas AM University, Ocean Drilling Program, College Station, TX 77845-9547, USA, 2003.
- Tréhu, A., P. Long, M. Torres, G. Bohrmann, R. Rack, and T. C. et al., Three-dimensional distribution of gas hydrate beneath southern Hydrate Ridge: constraints from ODP Leg 204, *Earth Planet. Sci. Lett.*, 222, 845–862, 2004.
- Tréhu, A. M., and N. L. Bangs, 3-D seismic imaging of an active margin hydrate system, oregon continental margin, report of cruise ttn112, *Oregon State Univ. Data Rpt.*, 182, 2001.
- von Huene, R., I. A. Pecher, and M.-A. Gutscher, Development of the accretionary prism along Peru and material flux after subduction of Nazca Ridge, *Tectonics*, 15, 19–33, 1996.
- Voogd, N. D., and H. D. Rooijen, Thin layer response and spectral bandwidth, *Geophysics*, 48, 12–18, 1983.
- Westbrook, G., B. Carson, and R. M. et al., *Proceedings of the Ocean Drilling Program; initial reports*, vol. 146, Texas AM University, Ocean Drilling Program, College Station, TX, United States, 1994.
- Widess, M. B., How thin is a thin bed?, *Geophysics*, 38, 1176–1180, 1973.
- Winkler, K. W., and A. Nur, Seismic attenuation: Effects of pore fluids and frictional sliding, *Geophysics*, 47, 1–15, 1982.
- Wood, W., P. Stoffa, and T. Shipley, Quantitative detection of methane hydrate through high-resolution seismic velocity analysis, *J. Geophys. Res.*, 99, 9681–9695, 1994.
- Wood, W., W. Holbrook, and H. Hoskins, In situ measurements of P-wave attenuation in the methane hydrate- and gas-bearing sediments of the Blake Ridge, in *Proc. ODP, Sci. Results*, vol. 164, edited by C. Paull, R. Matsumoto, P. Wallace, and W. Dillon, pp. 265–272, Texas AM University, Ocean Drilling Program, College Station, TX, United States, 2000.

- Wyllie, M. R. J., A. R. Gregory, and G. H. F. Gardner, An experimental investigation of factors affecting elastic wave velocities in porous media, *Geophysics*, *23*, 459–493, 1958.
- Yilmaz, ., *Seismic Data Processing*, first ed., Society of Exploration Geophysicists, 1987.
- Yuan, T., R. D. Hyndman, R. D. Spence, and B. Desmons, Seismic velocity increase and deep-sea gas hydrate concentration above a bottom-simultaing reflector on the northern Cascadia continetal slope, *J. Geophys. Res.*, *101*, 13,655–13,671, 1996.
- Zelt, C., Modelling strategies and model assessment for wide-angle seismic travelttime data, *Geophys. J. Int*, *139*, 183–204, 1999.
- Zelt, C., and P. Barton, Preparation and preliminary modelling of 3-D ocean bottom seismometer data from the faroe basin experiment, *Mobile Technical Report, Contract Number 93792*, p. Phase 4, 1994.
- Zelt, C., and R. Smith, Seismic travelttime inversion for 2-D crustal velocity structure, *Geophys. J. Int*, *108*, 16–34, 1992.
- Ziolkowski, A., A method for calculating the output pressure waveform from an airgun, *Geophys. J. Roy. Astr. Soc*, *21*, 137–161, 1970.
- Ziolkowski, A., Measurement of air-gun bubble oscillations, *Geophysics*, *63*, 2009–2024, 1998.
- Zoeppritz, K., Über Reflexion und Durchgang seismischer Wellen durch Unstetigkeitsflächen, *Über Erdbebenwellen, Nachrichten der Königlichen Gesellschaft der Wissenschaften zu Göttingen*, pp. 47–84, 1919.

Acknowledgements

Prof. Dr. Ernst Flueh is gratefully acknowledged for his continuous support and advice during the last few years.

I am very grateful for the ongoing assistance and guidance of Dr. Dirk Kläschen.

I also express my thanks to Prof. Dr. Wolfgang Rabbel for spontaneously agreeing to act as co-referee.

Special thanks belong to Anne Krabbenhöft for numerous proof-readings and many suggestions, which made this thesis 'happen' in time.

I would like to thank Jörg Petersen for the valuable discussions on and beyond gas hydrates.

Furthermore I thank Dr. Matthias Zillmer for proof-reading and his advice on many subjects.

Special thanks to my parents and my sister for their support during the last few years.

Many thanks to all members of the Geodynamics Department for their friendly assistance and the kind atmosphere within the department.

Erklärung

Hiermit erkläre ich, daß die von mir für das Promotionsverfahren vorgelegte Abhandlung 'Seismic Investigations of a Bottom Simulating Reflector: Implications on Gas Hydrate and Free Gas at Southern Hydrate Ridge', abgesehen von der Beratung der Betreuer nach Inhalt und Form, meine eigene Arbeit ist. Bisher ist die Arbeit noch nicht an anderer Stelle im Rahmen eines Prüfungsverfahrens vorgelegt worden.

Cord Papenberg.

Curriculum Vitae

Personal details:

Name: Cord Papenberg
Date of Birth: 29.06.1970
Place of Birth: Rawalpindi
Citizenship: German

Doctorate:

Since February 2001 PhD student at IFM-GEOMAR, Kiel

Education:

October 2000: German Diplom (equivalent MSc) in Geophysics
1994 – 2000: Studies in Geophysics at the University of Kiel
1992 – 1994: Studies in Economical Engineering at the University of Braunschweig
1990 – 1992: Short-service volunteer in the German Navy
1990: German Abitur
1985 – 1990: German Swiss International School, Hong Kong
1979 – 1985: German School The Hague, The Netherlands
1976 – 1979: German School Helsinki, Finland